The Statistics of Stellar Multiple Systems Formed from Small Subclusters

Hannah Elizabeth Ambrose

A thesis submitted for the degree of Doctor of Philosophy

Cardiff University
July 2025

Abstract

The early life of small stellar subclusters – particularly as they evolve from the protostellar phase to stable main sequence systems – is poorly understood. In this thesis, I investigate the dynamical evolution of subclusters over this stellar adolescent phase.

I model isolated subclusters with different numbers of stars, N, and previously unexplored initial conditions (such as ordered rotation) and evolve them using an n-body algorithm. I derive an equation to generate the possible end states that these subclusters can produce. I also present a prescription for mixing the statistics generated by different values of N, which I use to investigate cores that produce a range in number of stars. I analyze the multiplicity statistics and architectures of the final systems, and compare them with the solar-mass primary statistics from Tokovinin (2021). Through this comparison, I derive predictions about the initial conditions of subclusters as they leave the protostellar phase.

To produce the best fit to the observed statistics, I find that prestellar cores must typically spawn between 4.3 and 5.2 stars. Subclusters that begin with roughly half their kinetic energy invested in rotation produce the best fits to the Tokovinin (2021) sample. These properties are also compatible with the observed *Orbital Statistics*, i.e. the distributions of semi-major axis, mass ratio, eccentricity and mutual inclination and eccentricity. The observed distribution of mutual inclinations in particular favours an average N of 4.8. The *Best-Fit* properties produce a similarly shaped mutual orbital inclination distribution as observations, with a phase offset.

The initial number of stars in the subcluster, N, has the greatest effect on the systems it produces, influencing periods and separations, dynamical biasing, plurality, mutual orbital inclinations, and ejection timescales. The fraction of kinetic energy in ordered rotation and the degree of mass segregation also have an effect on some of these statistics.

For the *Best-Fit Case*, I find that $21(\pm1)\%$ of subclusters spawn two or more multiple systems.

Publications

First Author Publications

Ambrose H. E., Whitworth A. P., 2024; *The formation of multiples in small-N subclusters*, MNRAS, 535, 3700

Ambrose H. E., Whitworth A. P., 2025; *Orbital statistics of multiple systems formed from small-N subclusters*, MNRAS (in review)

Author contributions

Chapters 2 and 3 detail and expand on the work published in Ambrose & Whitworth 2024. Chapter 4 relates the Ambrose & Whitworth 2025 work, which is currently in review with *Monthly Notices of the Royal Astronomical Society*. The content of these chapters constitutes collaborative work between myself and my supervisor and co-author, Professor Anthony Whitworth.

Contents

List of Tables

List of Figures

"I'm ready"
Spongebob Squarepants —
Spongebob Squarepants

Acknowledgements

"Knowledge cannot replace friendship"

Patrick Star — *Spongebob Squarepants*

Thanks:

To my parents, who first nurtured my love of science. Thank you for taking countless hours of your days to walk through dusty museums and stand shin-deep in creek water. You made learning the most fun a kid could have. You love and support me every day, and I don't know how I could ever thank you enough. So I got a doctorate.

To my aunts, uncles, and cousins, and all my family, who even from across an ocean let me know that they are there for me and proud of what I do. Your support means more than you know.

To my housemates Matt and Patrick, without whom I wouldn't have a single cardboard cutout of Henry Cavill, let alone two. Thanks for the wine nights, marathons of Magnum P.I., and just making me laugh – especially when you don't mean to.

To my friends Adriana and Min, who have all the dirt on me. Over the past four years we've stood together on top of Namsan and talked together from opposite thirds of the world. Being able to tell each other all about the ups and down of the PhD process made everything feel a little less crazy. Thanks amigas.

To my supervisor, Ant, for your mentorship. You have always treated me first and foremost as a collaborator and a scientist. Thanks for putting up with me and my heathen American grammar.

To the faculty and students of the School of Physics and Astronomy. To everyone who came to coffee, lunch, and brought cake on Thursdays. Thanks for the conversation, commiseration, and mutual procrastination.

And to the United Kingdom Research and Innovation Science and Technology Facilities Council, for funding my research and life in the UK. Support for the sciences is so very important, and I couldn't have done any of this without the UK government's help.

Chapter 1

Introduction

1.1 Multiple systems and their architectures

Stellar multiples are relatively close, bound systems of stars that circle one another on regular, stable (or meta-stable) orbits. The most common multiples are binary, with two stars orbiting their mutual centre of mass. Systems with three or more stars are known as "higher-order multiples" and can feature complex structures. Figure 1.1 illustrates the possible architectures for stable 3- and 4-star multiples. Stable, long-lived triple systems are hierarchical; they're composed of a relatively close central pair of stars and a third member on a much wider orbit (Fig. 1.1a). Stable quadruple systems can have one of two architectures: a '2+2' system with two relatively close stellar pairs on a wide orbit about one another (Fig. 1.1b); and a 'planetary' system with four stars on increasingly wide orbits (Fig. 1.1c). Multiples with more than four stars can be made up of increasing numbers of close pairs, planetary configurations, or combinations of the two.

Many complex multiples feature prominently in our own night sky. Mizar and Alcor, which form the middle of the handle in the Plough (or Big Dipper) asterism, is a 2+2+2 sextuple (Mamajek et al., 2010; Zimmerman et al., 2010). The Castor system, which forms the head of the left twin in the Gemini constellation, is a 2+2+2 sextuple as well (Adams & Joy, 1917). The highest-order multiples known are septuples. Figure 1.2 (from Tokovinin 2021) shows a diagram of one septuple, 65 UMa (11551+4629), where a central pair is orbited not only by three companions on hierarchical orbits, but by a close pair on a distant orbit as well. Understanding the overarching structure of these systems informs how we interpret observational statistics and drives theories of star formation.

1.2 Observational studies

While the internal structures of complex multiple star systems are known on a case-by case basis, uncovering how common such systems are – and how their properties vary across different stellar populations – requires systematic observational surveys. In early multiplicity surveys of low- and intermediate-mass primaries, higher-order multiplicity

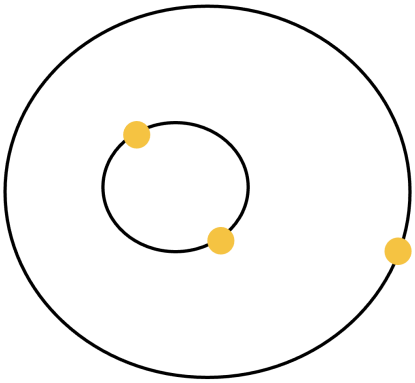

(a) Planetary Triple

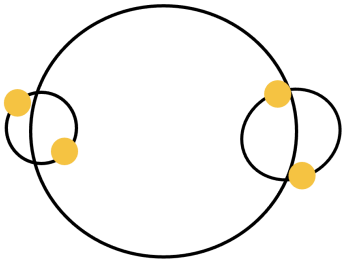

(b) 2+2 Quadruple

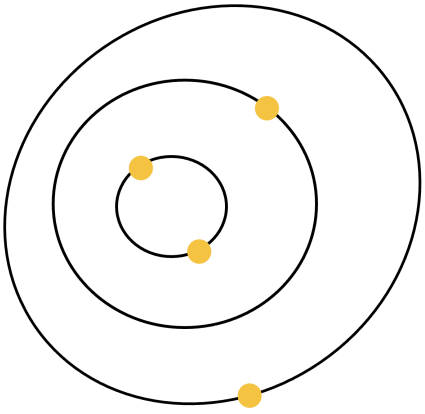

(c) Planetary Quadruple

Figure 1.1. Diagrams of possible architectures for triple and quadruple systems. Relative orbit and star sizes are illustrative and not to scale.

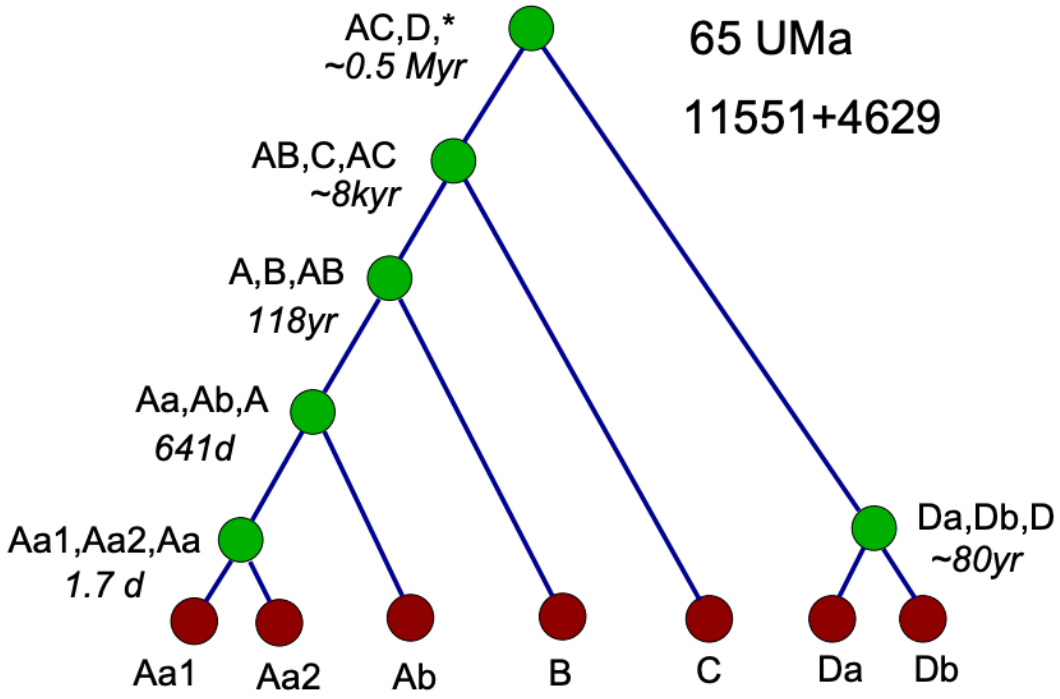

Figure 1.2. Diagram of the structure of septuple star system 65 UMa. From Tokovinin (2021).

appeared to be rare. When Duquennoy & Mayor (1991) studied the multiplicity of solar-type stars in a 22-pc sample, they found that only 5% hosted triple or other higher-order systems. Recent advances in observational technology and capability have led to the discovery of additional members in previously catalogued star systems, thereby increasing the percentage of known higher-order multiples in the solar neighbourhood. For a 25-pc sample, Raghavan et al. (2010) found 13% of systems to be higher-order multiples, and this increased to 17% when Tokovinin (2021) and Hirsch et al. (2021) studied the sample in 2021.

Current statistics for nearby systems with solar-type, main-sequence primaries (Tokovinin 2021, hereafter the T21 sample), are:

$$\mathrm{S} : \mathrm{B} : \mathrm{T} : \mathrm{Q}^{+} = 54 : 29 : 12 : 5\,. \tag{1.1}$$

Here S is the percentage of single stars, B the percentage of binaries, T the percentage of triples, and Q^{+} the percentage of quadruples plus higher-order systems (i.e. quintuples, sextuples and septuples).

Thus, in this sample, the fraction of stars that are single is

$$f_{\mathrm{s}} = \frac{\mathrm{S}}{\mathrm{S} + 2\mathrm{B} + 3\mathrm{T} + 4\mathrm{Q}^{+}} \quad \simeq \quad 32.1\%\,; \tag{1.2}$$

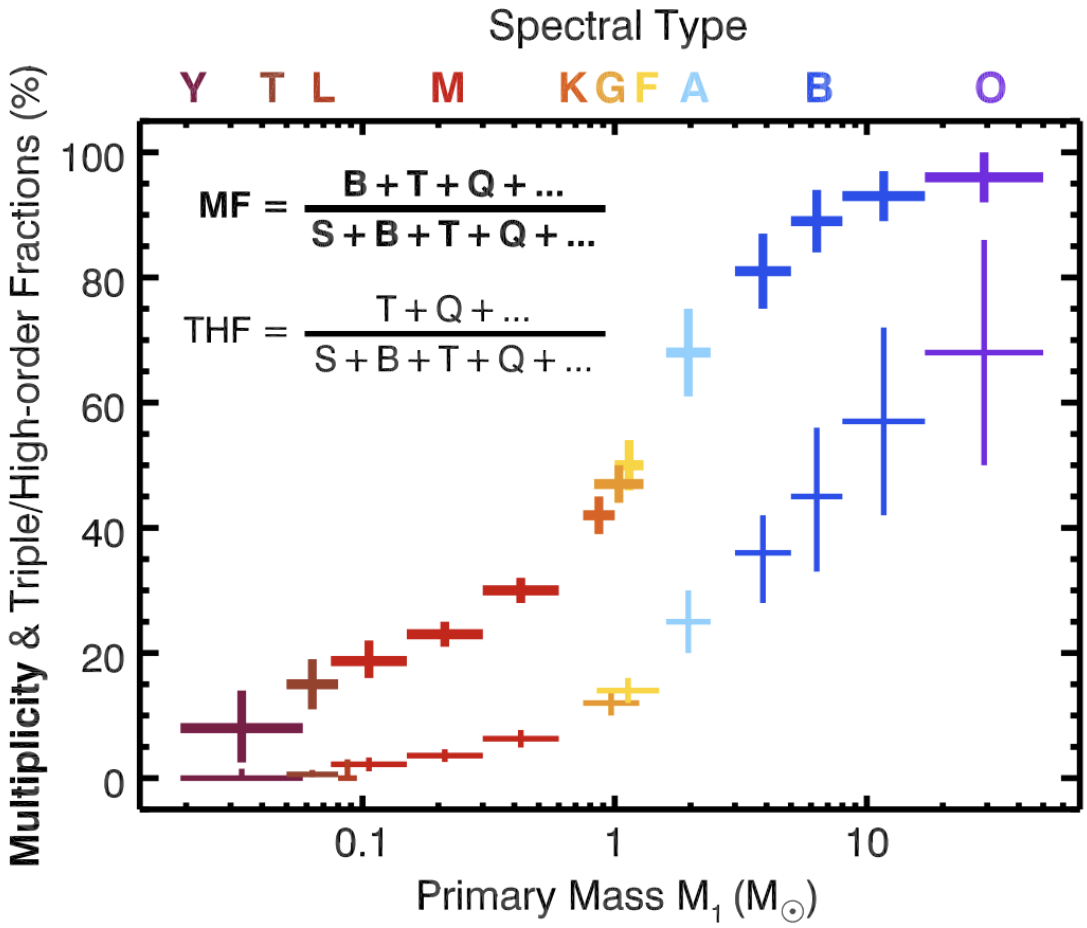

Figure 1.3. Fraction of stellar systems which are multiple (bold) and triple or higher-order, as a function of primary mass. From Offner et al. (2023).

the fraction of stars that is in binaries is

$$f_{\rm B} = \frac{\rm 2B}{\rm S + 2B + 3T + 4Q^{+}} \quad \simeq \quad 34.6\% \,; \tag{1.3}$$

the fraction that is in triples or higher order systems* is

$$f_{\rm T^{+}} = \frac{\rm 3T + 4Q^{+}}{\rm S + 2B + 3T + 4Q^{+}} \quad \simeq \quad 33.3\% \,. \tag{1.4}$$

and the fraction of stars that is in any multiple is

$$f_{\rm M} = \frac{\rm 2B + 3T + 4Q^{+}}{\rm S + 2B + 3T + 4Q^{+}} \quad = \quad 1 - f_{\rm S} \quad \simeq \quad 67.9\% \,; \tag{1.5}$$

The multiplcity statistics vary greatly with the mass of the primary star. Figure 1.3 (from Offner et al. 2023) plots the fraction of systems which are multiple (MF) and the fraction of systems which are triple or higher multiplicity (THF) as functions of mass. While less than 15% of the smallest dwarf primaries host multiples, as many as 98% of the largest O star primaries do. This trend is also reflected in the THF, which peaks slightly lower at 85%. These percentages (especially at higher masses) are uncertain due to selection effects and observational bias.

Multiple systems are detected using a variety of methods, each of which introduce different biases into observed multiplicity results. Close systems are often detected through spectroscopic or eclipse methods. Spectroscopic (or radial velocity, RV) techniques detect line-of-sight velocity changes in the movement of stars to identify multiple systems (Vogel, 1890; Pickering & Bailey, 1896). As the bodies of a binary system, for example, orbit one another, the stars move alternately toward and away from the observer. This velocity change produces periodic Doppler shifts in the stars' spectral lines, creating a cyclic signature over the orbital period. When a star's spectrum is strong enough to be measured, the degree of red or blue shifting gives its velocity along the line of sight. From these velocity measurements, astronomers can identify multiple systems even if only a subset of the components are directly observed. The technique favours short period orbits, whose larger, faster RV variations are easier to detect. It is more likely to miss companions in very unequal-mass systems, where the relatively weak pull of the secondary produces only slight variations in radial velocity of the primary, and where the fainter spectral lines of the secondary may be more difficult to distinguish from those of the brighter companion. It is less sensitive in general to low-mass (and therefore low luminosity) stars, whose spectra are fainter.

*I have assumed that all the systems contributing to $\rm Q^{+}$ are quadruples. If I account for the systems that are quintuples, sextuples and septuples, $f_{\rm T^{+}}$ will increase slightly, at the expense of $f_{\rm S}$ and $f_{\rm B}$.

Close, similar-mass multiples are also favored in the eclipse detection method. Here, stars are monitored for periodic dips in flux (Stebbins, 1910), which occur when a companion passes in front of its primary (blocking a portion of its light) and behind its primary (where the companion's light is obscured). Companions on close orbits are geometrically more likely to cross the disk of the primary from the perspective of the observer, and since close systems have shorter periods, they produce more frequent eclipses. Larger, more equal-mass companions present a large cross-sectional area compared with the primary, blocking a larger fraction of their primary's light when eclipsing, and contributing more luminosity that is obscured when they themselves are eclipsed. This produces deeper, easier to detect dips in flux.

Wider systems are detected with techniques such as astrometry, image blinking, and speckle interferometry. Astrometric multiplicity studies (first introduced by Herschel 1803) rely on precisely monitoring a star's position to map its motion compared with the expected linear trajectory of single stars. By comparing a star's measured trajectory with either the bulk motion of nearby stars or a fixed reference frame, astrometry reveals bodies which exhibit periodic movement in the plane of the sky. This periodic movement, which is the result of gravitational motion around a system's centre of mass, can be used to identify stars which are gravitationally bound companions or which host unobserved companions. The likelihood of astrometric detection depends upon the degree of curvature detected, as motion must be observed to deviate from a linear path. Therefore, the method is most effective with a high cadence and time span of measurements in comparison with the system orbital period. Unequal mass systems can be more difficult to identify, as the brighter primary star exhibits little movement around the centre of mass, while the secondary, despite a potentially wide orbit, may be too faint to detect directly.

Image blinking detects wide multiples by taking images of sky at two epochs and comparing them to reveal co-moving stars (van Biesbroeck 1944). Because both (or all) companions must be detected, the method favours luminous stars. Speckle interferometry (Labeyrie, 1970; Gezari et al., 1972) detects wide multiple systems by analyzing the speckle pattern, an interference effect visible in stellar images as a result of atmospheric turbulence and telescope aberrations. When a Fourier transform is applied to an image of a multiple system, a pattern of equal-spaced fringes emerges. The spacing and relative strength of these fringes encodes the separation and brightness of the components, respectively. As brighter, more equal-contrast fringes are easier to detect, the method favours luminous stars and equal-luminosity multiples.

Large multiplicity catalogues often collate the results of many surveys, and thus include results from many detection methods. The Raghavan et al. (2010) and Tokovinin (2021) samples, for instance, include multiples identified through all of the aforementioned detection methods. Melding the results of these various methods helps to form a more

figures/ChenFig_no_permission.png

Figure 1.4. Fraction of stellar systems which are multiple for Class 0 protostars, Class I protostars, and Main Sequence stars. From Chen et al. (2013).

complete understanding of multiplicity than can be achieved through any one method alone. The catalogues still include bias, with Tokovinin (2021) stating that in the sample, systems detected through eclipse are "over-represented, being easier to discover." So the Tokovinin (2021) statistics likely over-represent close, similar-mass multiples.

As technology and techniques advance, precision continues to improve in astronomical measurements, allowing for the detection of fainter, lower-mass companions. GAIA is one such example of a high precision facility improving the completeness of the multiple system sample through detection of new multiples (e.g. Shariat et al. 2025). As data continues to be processed from telescopes like GAIA, observational biases will likely only reduce and statistics such as $f_{\rm B}$, $f_{\rm T+}$, MF and THF will likely shift to higher values as additional members of existing systems are discovered.

Multiplicity is not static; rather it develops as stellar systems age. The MF is found to be highest in the earliest phases of protostellar evolution, and then declines through the subsequent protostellar phases. Chen et al. (2013) observed an MF of $0.64(\pm0.08)$ for low-mass Class 0 protostars, while Connelley et al. (2008a,b) found this fraction to be $0.57(\pm0.9)$ for Class 0 and $0.23(\pm0.8)$ for Class 1 sources in Perseus. Tobin et al. (2022) evaluated the same statistics in a more recent, higher resolution study of protostars in Perseus, finding that the MF decreases from $\simeq 0.49(\pm0.08)$ for Class 0 sources to $0.26(\pm0.09)$ for Class 1. Reipurth & Zinnecker (1993) found that the MF continues to fall from pre-Main Sequence to Main Sequence populations.

These trends highlight that multiplicity is both mass-dependent and evolutionarily dynamic. To understand the physical origin of these patterns, we consider the theoretical mechanisms by which multiple systems form.

1.3 Formation of stellar multiple systems

In this section, I review the dominant theoretical pathways proposed for the formation of stellar multiples. I specifically focus on the processes that form multiples on the core-scale – core and disc fragmentation – and discuss how simulations and observations constrain their relative importance.

In the standard star formation model, flows within turbulent molecular clouds converge to create self-gravitating sheets (Pringle, 1989). These sheets can further collapse into filaments, and eventually into prestellar cores (Turner et al., 1995). The process is not necessarily sequential, and the convergent flows can themselves directly spawn filament and core structures.

During the star formation process, stars from nearby cores can interact with one another. For this interaction to result in a stellar capture and produce a multiple, their mutual kinetic energy must be sufficiently dissipated to allow for gravitational binding. This energy can be removed through friction with the stellar accretion disc (Ostriker, 1994; McDonald & Clarke, 1995; Moeckel & Bally, 2007; Muñoz et al., 2015), or with remaining filamentary material if the approach occurs along the filament. Because stars accumulate significant kinetic energy during close approaches, substantial surrounding material is needed to dissipate it and enable capture. Disc-assisted capture, therefore, requires that discs must be very massive, and is typically only a viable formation mechanisms for high-mass primary multiples.

In low-mass prestellar cores, multiple systems typically form through two main processes: core fragmentation, and disc fragmentation. Figure 1.5 illustrates the four mechanisms of creating a stellar multiple (filament fragmentation, core fragmentation, disc fragmentation, and capture). It includes a schematic model, observational example, and simulation snapshot for each mechanism, along with their associated distance scales.

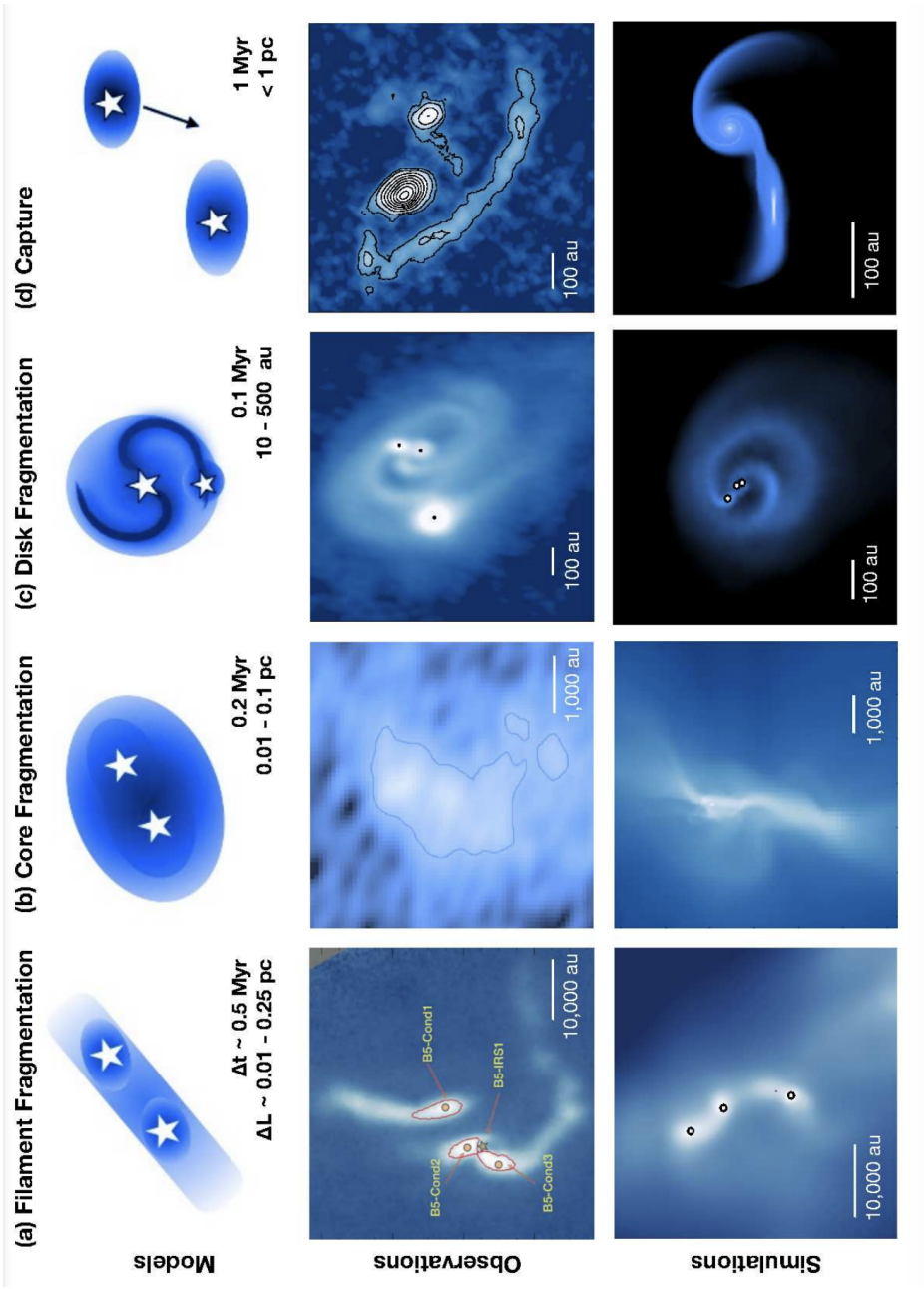

Figure 1.5. Model illustrations (top), observational examples (middle), and simulation snapshots (bottom) of the four mechanisms for multiple formation, from Offner et al. (2023).

In core fragmentation, as a prestellar core collapses, overdense regions may become gravitationally unstable and condense into multiple protostars (Boss, 1986). Conditions such as rotation, turbulence, and feedback within the core regulate the amount of fragmentation. Hennebelle et al. (2004) find that rotation increases the number of fragmentation products, and Cha & Whitworth (2003) find that differential rotation in particular (as opposed to solid-body rotation) promotes fragmentation. Even small amounts of turbulence can significantly enhance fragmentation (Goodwin et al., 2004a), and this effect becomes stronger with increasing turbulence (Goodwin et al., 2004b). Feedback comes in two main forms: radiative feedback, where collapsing material heats the core through compression and friction; and outflow feedback, where mass loss via jets and bipolar outflows alters the disc environment. The heating from radiative feedback can stabilize the core against collapse, while outflows heat the disc, induce turbulence, and transport mass and momentum away from the inner regions. Heating can either promote or inhibit fragmentation, and studies find that these mechanisms promote fragmentation specifically when they occur episodically. Lomax et al. (2014, 2015a, 2016) find that when radiative feedback is episodic, cores reproduce the peak in the prestellar core mass function and initial mass function, the observed brown dwarf-to-star ratio, and the field multiplicity statistics. Rohde et al. (2021) find that outflow feedback is also necessary: when episodic, it reproduces field multiplicity statistics for young populations, and reproduces the population of binary twins. These "twins" are an observed population whose ratio of primary to secondary mass is approximately equal (≥ 0.95).

Protostars that form from the dynamical collapse and fragmentation of the prestellar core are typically surrounded by an accretion disc. This disc forms from material with excess angular momentum, which prevents direct accretion onto the protostar. If the accretion disc becomes sufficiently massive, extended and cold, it fragments to produce a secondary star or stars in orbit around the primary (Larson, 1978; Adams et al., 1989; Chapman et al., 1992; Bonnell & Bate, 1994; Whitworth et al., 1995; Bhattal et al., 1998). This is "disc fragmentation". The discs can become unstable due to perturbation by a passing star (Boffin et al., 1998; Watkins et al., 1998a,b; Thies et al., 2010), by compression induced by a pressure wave, or by rotation of the core material itself (Hennebelle et al., 2004). Disc instability can also be triggered as material infalls onto the disc (Stamatellos et al., 2007) – specifically when this infall is rapid (Kratter et al., 2010) – though the heating produced by the incoming material stabilizes the disc while infall is still ongoing (Walch et al., 2009).

Cooling is essential to the fragmentation process; while fragments which form in the inner disc tend to form earlier, faster, and become more massive (Stamatellos & Whitworth, 2009), fragmentation occurs preferentially in the outer disc where cooling is most efficient (Stamatellos & Whitworth, 2008, 2009). Episodic accretion provides

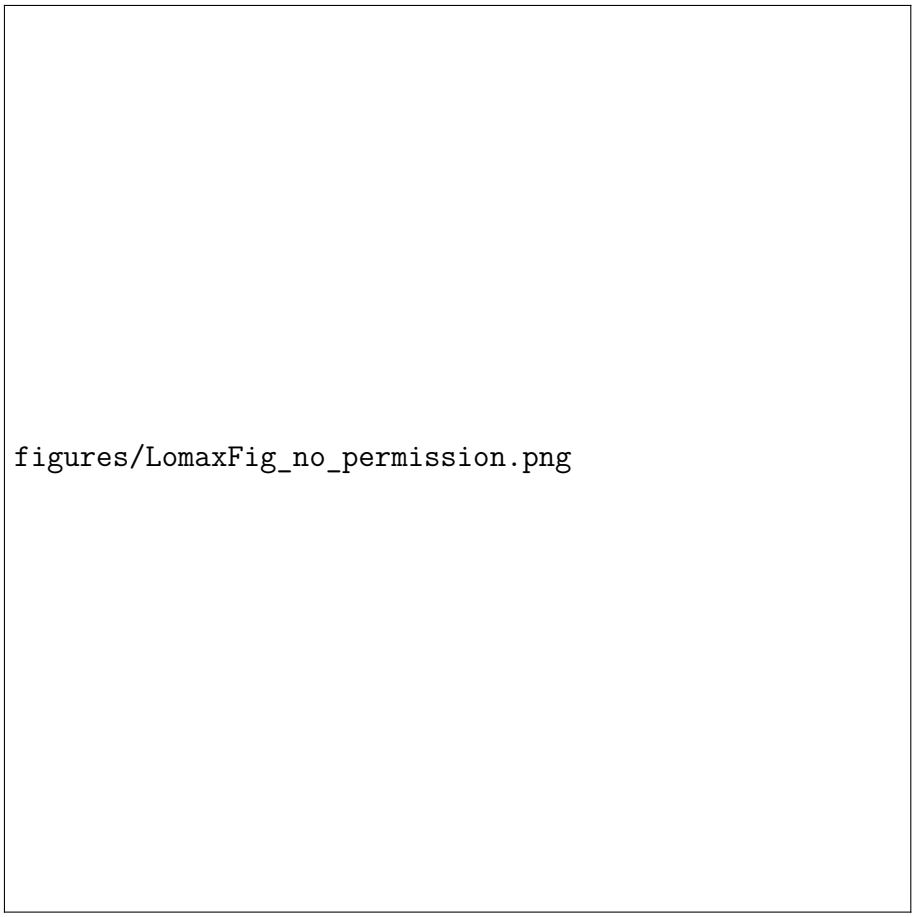

Figure 1.6. Zoom-ins of a 2+2+2 sextuple system formed from a combination of core and disk fragmentation. From Lomax et al. (2015a).

periods of cooling when fragmentation can occur (Stamatellos et al., 2011, 2012), and rapid rotation helps to extend discs, cooling them and allowing for higher rates of fragmentation (Walch et al., 2009).

The dominant fragmentation mode depends on factors such as feedback, ambient structure, temperature, and turbulence. Core fragmentation is preferred in cores undergoing radiative feedback (Offner et al., 2010). When cores form as part of the collapse of a filament, however, Walch et al. (2012) find that the presence of nearby cores suppresses the extended discs from which core fragmentation occurs. Disc fragmentation is highly sensitive to the initial temperature of the core, only occurring in the simulations of Sigalotti et al. (2023) when clouds begin with temperatures ≤ 6 K, and it dominates in the simulations of Lomax et al. (2015b) when turbulence is high.

Together, core and disc fragmentation can produce young multiple systems of as many as seven stars. For example, Lomax et al. (2015a) present a 2+2+2 sextuple system formed through a combination of both mechanisms, shown in Figure 1.6.

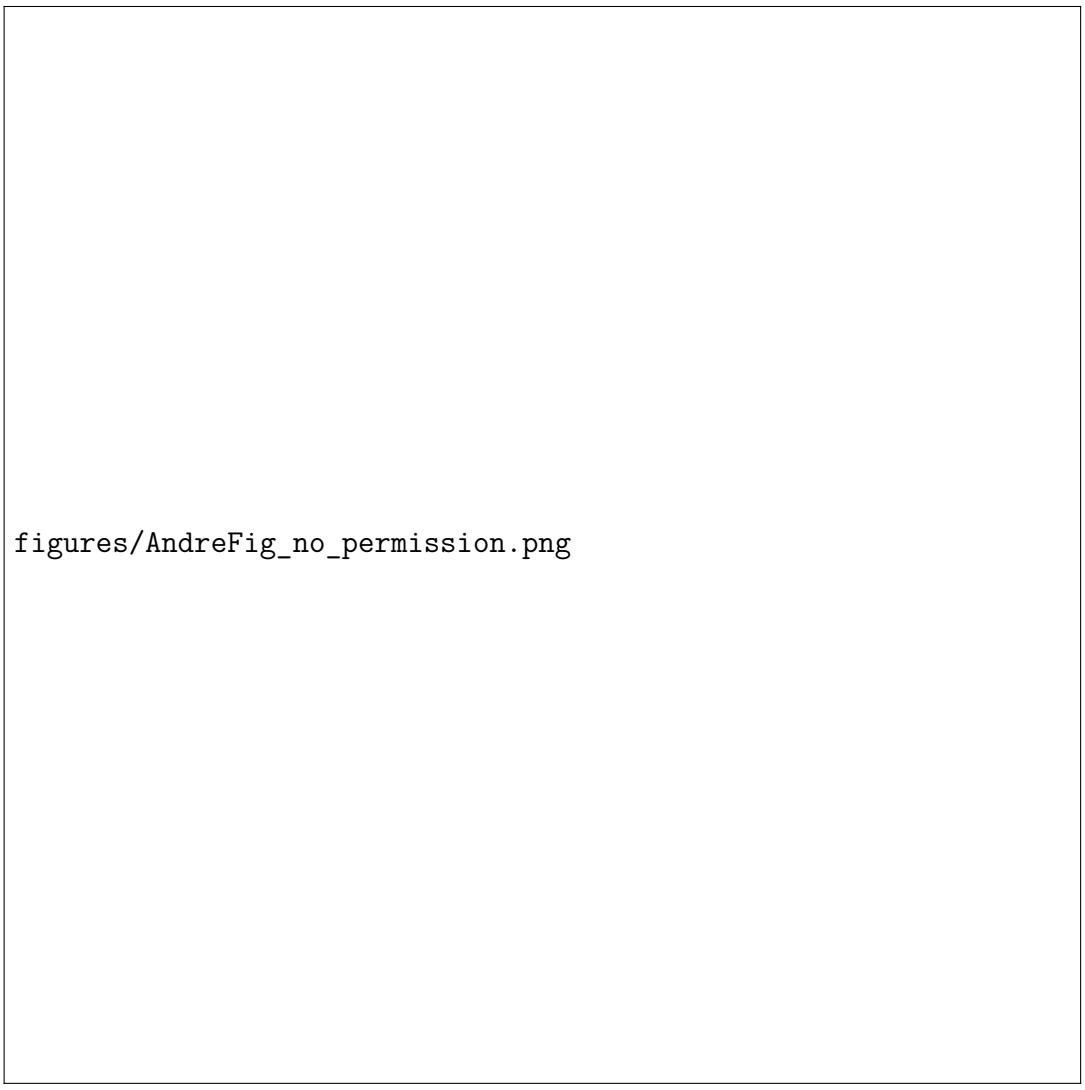

Figure 1.7. Comparison of the Kroupa (2001) IMF, the Chabrier (2005) system IMF, and the CMF observed by André et al. (2010) in the Aquila region, reproduced from André et al. (2010). The accompanying lognormal fit to the CMF data is in red, and the power-law fit to the CMF data is in black. Observations are from SPIRE/PACS observations of 541 prestellar core candidates. The typical mass spectrum of CO clumps from Kramer et al. (1998) is also included for comparison.

1.4 Previous related theoretical studies

A key constraint on star formation theories is the number of stars formed per core. Understanding this number helps connect observed multiplicity statistics to the physical processes of fragmentation and dynamical evolution. Here, I summarize key theoretical studies that estimate N, or investigate the dynamics of small stellar systems that emerge from core fragmentation. Lomax et al. (2015a) used smoothed-particle hydrodynamics (SPH) to simulate the evolution of Ophiuchus-like cores under various feedback models. They find that episodic radiative feedback best reproduced the peak in the stellar initial mass function (IMF) (Chabrier, 2005) and the observed ratio of low-mass stars to brown dwarfs (Andersen et al., 2008). Episodic radiative feedback also led the cores to reproduce the binary statistics of young embedded class II and class III protostars as observed by Kraus et al. (2011) and Kraus & Hillenbrand (2012)[†]. This best-fit feedback results in cores which produce an average of $4.5(\pm1.9)$ stars each.

In a more recent study, Rohde et al. (2021) model episodic outflow feedback in solar-mass cores using SPH. They find that the cores with outflow feedback reproduce the robust VANDAM multiplicity statistics of young sources in Perseus (Tobin et al., 2016) as well as the observed fraction of binary twins (Fernandez et al., 2017; Kounkel et al., 2019). The episodic outflow feedback leads the cores to produce an average of 3.14 ± 1.95 stars each. This value is slightly lower than that found by Lomax et al. (2015a), but the two results are consistent within uncertainties.

Holman et al. (2013) take a statistical approach to estimating N, analysing the relationship between the IMF and the Core Mass Function (CMF). The stellar IMF describes the observed distribution of stellar masses at the time of their formation. It is generally flat at lower masses and decreases as a power law at higher masses (Salpeter 1955;Chabrier 2003). The CMF describes the observed mass distribution of prestellar cores. The CMF exhibits a similar shape to the IMF, though shifted to higher masses by a factor of $\sim 2-4$ (Motte et al. 1998;Alves et al. 2007). Figure 1.7 from André et al. (2010) illustrates this offset. The similarity in their shapes and the shift in mass can both be explained if cores tend to fragment into multiple stars (with some relatively small mass loss and inefficiency). Holman et al. (2013) find that if the shape of the IMF is inherited from the shape of the CMF, then the increase in binary frequency with primary mass observed in multiplicity surveys (Fig. 1.3) requires that a prestellar core must typically spawn a subcluster of $4.3(\pm0.4)$ stars. This is the most constrained of the N estimates, and is in full agreement with both the Lomax and Rohde findings.

While the above studies focus on how many stars form per core, others examine how such small-N groups dynamically evolve into the multiplicity configurations we observe today. Sterzik & Durisen (1998) explore how multiplicity can arise and evolve in such

[†]The authors of the study note that these early binary statistics are not strongly constrained

small stellar subclusters with their dynamical n-body simulations of cold, non-rotating, spherical distributions of $N = 3$, 4, or 5 stars. The stars have masses drawn from a Miller-Scalo distribution, and are evolved for 1000 crossing times. At the end the multiplicities are

$$\begin{aligned} \mathrm{S:B:T} &= 47:47:6, \quad \text{for } N=3; \\ \mathrm{S:B:T:Q} &= 63:29:6:1, \quad \text{for } N=4; \\ \mathrm{S:B:T:Q^{+}} &= 70:19:9:1, \quad \text{for } N=5. \end{aligned} \tag{1.6}$$

Thus, they show that increasing N increases the percentage of singles and reduces the percentage of binaries.

McDonald & Clarke (1993) investigate how stellar mass shapes the outcome of small-N dynamics. In their model, they randomly sample stellar masses from an IMF-like distribution, then assuming the two most massive stars form a binary while all other stars remain single. They term this phenomenon Dynamical Biasing, and find that it reproduces the observed population of binaries with solar-mass primaries and low-mass luminous companions, while simultaneously explaining the observed scarcity of brown dwarf companions to solar-type stars. In a second paper, McDonald & Clarke (1995) use n-body simulations to show that, if the stars in a small-N subcluster are attended by discs, the increased dissipation during close encounters reduces the effectiveness of dynamical biasing, meaning that lower-mass stars have an increased chance of ending up in a binary. Lee et al. (2019) and Kuffmeier et al. (2019) further show that dynamical friction introduced by the disc causes forming protostars to migrate inward, hardening binaries and thus increases the tendency to produce higher-order multiples.

If gas from the natal cloud is present, Kuruwita & Haugbølle (2023) show that the resulting drag can also drive the migration, or inspiral, of forming stars, bringing binaries closer together. This would likewise increase the proportion of higher-order multiples.

1.5 Early clustering in observations

Observations support the presence of small protostellar groupings within nearby, young star-forming regions. Cartwright & Whitworth (2004) introduce a technique to quantify stellar substructure within regions such as molecular clouds. Through this technique, they show that the Chameleon Molecular Cloud displays moderate hierarchical substructure, indicating that its young stellar objects are spatially grouped. The Taurus Molecular Cloud shows an even greater degree of clustering in this study. The number of protostars present in these groupings can vary between regions. In the Auriga-California Molecular Cloud, for instance, Broekhoven-Fiene et al. (2014) identify 7 protostellar clusters: 4 containing 10 or more stars, and 3 smaller groups of $5 - 9$ stars. Similar hierarchical organization is shown in young protostars across low mass star-forming

environments; Schmeja et al. (2008) report clustering of Class 0 and Class 1 protostars in the Perseus, Ophiuchus, and Serpens Molecular Clouds. Their analysis reveals age effects in substructure, finding Class $2/3$ protostars to be centrally condensed, resembling older star clusters. They attribute this change in substructure to dynamical interactions between protostars, which erase hierarchical, clustered structure on a few-Myr timescale.

1.6 Long-term impact of early dynamics

The early dynamical environment in which stars form can leave long-lasting imprints on both the internal structure of multiple systems and the demographics of the field star population. By studying these outcomes, we can reconstruct aspects of the subcluster dynamics that produced them. In this work, I focus on three key mechanisms that produce these signatures: Dynamical Biasing, von Zeipel-Lidov-Kozai cycles, and stellar ejections.

Sterzik & Durisen (1998) (hereafter SD98) observe Dynamical Biasing in their numerical simulations of subclusters with $3 \leq N \leq 5$. In triple and higher-order multiples, $80 - 90\%$ of central orbits involve the two most-massive stars, and this percentage increases with increasing N, and with the range of stellar masses within the subcluster. At the same time, the mean semi-major axis of these central orbits decreases with increasing N, since with larger N there are more opportunities for three-star interactions. The degree of dynamical biasing in observations, therefore, provides insight into the initial number of stars and the initial mass distribution of subclusters.

When three-star interactions take place within a hierarchical triple, gravitational perturbations from the outer companion can induce a periodic exchange of angular momentum between the orbits. These von Zeipel-Lidov-Kozai (ZLK) cycles result in a cyclic variation in the eccentricity of the inner orbit, combined with a cyclic variation in the mutual orbital inclination (von Zeipel, 1910; Lidov, 1962; Kozai, 1962). They can drive the inner binary toward high eccentricity, potentially triggering tidal interactions or mergers, and they can flip the orbits of systems from prograde to retrograde (e.g. Naoz, 2016).

The dynamics of subclusters also play a key role in shaping broader field populations, particularly the statistics of single stars, since many single stars start life in subclusters before being ejected into the field. Consequently the number, mass distribution, and velocity distribution of single stars are significantly influenced by the dissolution of their natal subclusters. For example, the single star population should start with a velocity distribution compatible with the velocity distribution of subcluster ejections. Subsequent interactions between these single stars and other objects (other field stars, star clusters and molecular clouds) may then alter this distribution. In addition, Dynamical Biasing leads to the preferential ejection of lower-mass stars, which is seen in both numerical n-body

(McDonald & Clarke, 1995; Sterzik & Durisen, 1998) and hydrodynamical simulations (e.g. Goodwin et al., 2004a), resulting in a lower average mass for single stars compared to those in multiple systems. The initial velocity distribution of field stars – especially low-mass singles – may therefore preserve a dynamical imprint of early subcluster interactions, offering a potential observational probe of the fragmentation and ejection process.

1.7 *n*-body integration

While prescriptions such as SPH are used to understand the fragmentation of prestellar cores into protostellar multiples, once fragmentation and migration are complete (and much of the natal gas has accreted or dissipated), n-body dynamics dominate the evolution of stellar multiple systems.

Objects gravitate according to Newton's law of universal gravitation (Newton, 1687), and when a gravitating system is made up of two bodies in isolation, the equations of motion can be solved exactly. But for $N > 2$, no analytical solution exists. Instead, the position and velocity of each object are described by a coupled set of infinite Taylor series expanded around time:

$$\mathbf{x}(t+h) = \mathbf{x}(t) + h\mathbf{x}'(t) + \frac{h^2}{2!}\mathbf{x}''(t) + \frac{h^3}{3!}\mathbf{x}'''(t) + \frac{h^4}{4!}\mathbf{x}^{(4)}(t) + \cdots \tag{1.7}$$

$$\mathbf{x}'(t+h) = \mathbf{x}'(t) + h\mathbf{x}''(t) + \frac{h^2}{2!}\mathbf{x}'''(t) + \frac{h^3}{3!}\mathbf{x}^{(4)}(t) + \frac{h^4}{4!}\mathbf{x}^{(5)}(t) + \cdots , \tag{1.8}$$

where $\mathbf{x}$ is the position vector, t is time, h is the timestep, and n "primes" represent the n-th derivative of $\mathbf{x}$.

The position and velocity of each body at some future time must be estimated based on the force exerted by each other body. As a result, complexity increases with N, as a system of N stars requires $N(N-1)/2$ force calculations. Errors arise during the trajectory calculations as an artifact of taking discrete time steps and of truncating the estimated values at each of these steps. Short timesteps can improve accurracy to a degree, but errors will still grow exponentially with integration time (Miller, 1964). Within the isolated gravitating system, the quantites of total orbital energy, linear momentum, angular momentum, and centre of mass velocity will always be conserved, providing a benchmark for monitoring tbe growth of errors. Astronomers once calculated the dynamical movements of these $N > 2$ systems by hand (Stromgren, 1900; Strömgren, 1909), but even with today's computational technology, the n-body problem remains complex.

Predictor-corrector methods of n-body integration reduce the number of force evaluations needed by predicting the trajectory of a particle at some timestep using the Taylor expansion, then refining the estimate with a corrector formula based on the updated information (see Aarseth 2003). von Hoerner (1960), who introduced the

method, estimates the calculations to the fourth order of the Taylor series. Following works tested higher-order approximations (e.g. Aarseth, 1966; Wielen, 1967), but the increased integration time was typically found to outweigh the gains in accuracy (Wielen, 1974). One predictor-corrector algorithm commonly used in astrophysical contexts is the 3rd Order Hermite scheme (Makino, 1991), which relies on estimating the acceleration and jerk of each body. It is particularly suited to systems with large variation in mass scales, distance scales, and dynamical timescales; it is also symplectic, which leads to good conservation of energy over time.

The Runge-Kutta family of methods tackles the problem of reducing force evaluations by estimating the trajectory at an intermediate, half-timestep (Runge, 1895; Kutta, 1901). It is typically implemented at the 4th order, where four interim steps are calculated using the previous timestep, two half-timesteps calculated with the preceding interim step, and the full timestep calculated with the preceding interim step (see equations 2.40-2.47 in Chapter 2). All interim steps are then weighted and summed to produce an estimated change in position and velocity (2.48). RK4 is not symplectic, and can introduce a drift in conserved quantities over time, though if total energy change is properly monitored, this does not pose a problem for the end systems. As the integration scheme only requires the calculation of position and velocity, it is simpler to implement than integrators like Hermite.

More advanced techniques have been developed to address the issues that arise with large variations in distance scale and very large n. For instances where individual systems may experience a wide variety of distance scales, such as on elliptical orbits, adaptive timesteps can increase accuracy and efficiency. They set each timestep according to the relative change in trajectory from the step before, ensuring small steps at close encounters and allowing large steps at large separations. When integrating systems whose different components may remain on very disparate distance scales from one another, such as a star cluster with close binaries, the close systems require much shorter timesteps to maintain precision than is necessary for the widely separated pairings. In these instances, instead of updating every star on the same timestep, each body can update on an individual timescale. These techniques can be used individually, or in conjunction, as the setup requires. For groups of very closely interacting bodies, conventional two-body calculations can result in singularities. To avoid these singularities, chain regularization recasts the equations of motion into a regularized coordinate system, typically organized in a chain structure (Aarseth & Zare, 1974).

For very large n, calculating the forces between all particles becomes prohibitive. Neighbour schemes reduce computational load by limiting calculations for each body to some grouping of nearby "neighbours" (Ahmad & Cohen, 1973, 1974), and tree codes estimate the combined effect of distant groupings of particles as one force (Barnes &

Hut, 1986; McMillan & Aarseth, 1993). For extremely large n, such as in cosmological simulations, particles can be assigned to a piece of a grid or mesh for which the potential is solved before interpolating the motion back to each body. This grid is used in conjunction with a neighbour treatment in the particle-particle particle-mesh method (Hockney & Eastwood, 1988).

Like any numerical method, n-body balances the benefits of accuracy with the cost of complex implementation and increasing computation time. While many complex tools have been developed, simpler prescriptions often suffice for small-n systems with constrained scales, especially when care is taken to monitor the accumulation of errors.

1.8 Aim of the thesis

Through a combination of observation and theory, we know the following:

- **Higher-order multiples are prevalent:** They comprise a significant portion of stellar systems, even for lower primary masses when multiplicity is less common. Multiplicity statistics are likely to be higher than current observational surveys report, since detection methods likely miss the lowest mass and most widely-separated companions.

- **They can form from individual cores:** Many protostars can condense from a single prestellar core, as either a consequence of core fragmentation, disc fragmentation, or a combination of the two. The conditions of these cores influence the fragmentation pathway and its efficiency.

- **Low-mass protostars must form in groups to reproduce multiplicity statistics:** Several distinct theoretical studies converge on the conclusion that an average of 4 or 5 stars likely form from each low-mass prestellar core, though the exact number may vary by environment.

- ***n*-body integration is a useful tool for understanding these protostellar subclusters:** n-body integration techniques, while unable to solve for gravitational motion analytically, provide valuable insight into the complex movements, evolution, and dissolution of small-N subclusters and the systems they can form. n-body interactions alone can create stable multiples from randomized subclusters, even in very simple models. The addition of features like gas and discs should increase the survival of these multiples.

- **Evidence of a dynamic history should be visible in the final systems:** Markers of an early life in dynamically-active small-N subclusters persist within stellar multiples and the single star population long after the subcluster has dissolved.

Despite the advances made in our understanding of stellar multiplicity, several open questions remain:

- **What happens to fragments over the long term?** Simulations of fragmentation halt at the protostellar stage, and sometimes before. How do these protostars evolve as a group? How are they affected by initial conditions unexplored by Sterzik & Durisen (1998)?
- **Are $N > 5$ subclusters able to form long-lived multiples?** Of how high an order? How do these subclusters alter the global multiplicity statistics?
- **What initial number of protostars, when evolved, best reproduce the observed multiplicity statistics?** How does this number compare with previous findings? If they agree, how does it constrain our estimate of N?

With these open questions in mind, this thesis seeks to model the evolution of stellar subclusters between the protostellar and main sequence phases with previously-unexplored initial conditions. By comparing the multiplicity statistics and structural features of the final systems with observed statistics, I will make predictions about the initial conditions of the subclusters, with an emphasis on N. The goal of this work is to find an estimate of N which reproduces observed statistics and constrains the estimates of previous works.

1.8.1 Thesis plan

- Chapter 2 introduces the method by which I set the initial conditions of the subclusters, evolve them, and calculate their system characteristics. I also outline a procedure to idenfity and track stellar multiples.
- In Chapter 3, I evolve subclusters with $3 \leq N \leq 7$ and various initial conditions. I introduce a scheme to combine results from realizations of different N in order to identify the mix of N values which best reproduces observed multiplicity statistics.
- Chapter 4 analyses the effect of initial conditions on the structural features of the stellar systems produced by the experiments in Chapter 3.
- In chapter 5, I explore and derive a function which outputs the number of possible end states for a subcluster of N stars. The function also gives the multiplicities of all systems which make up each end state.
- The final chapter summarizes the thesis, outlines key results, and discusses future avenues of exploration.

Chapter 2

Method

In this chapter, I outline the technical processes used to set up stellar subclusters, evolve them through time, and determine the characteristics of the systems they produce. I further discuss how the output of these processes is stored, the efficiency and accuracy of the integration, and how the data may be scaled to study subclusters of different masses and sizes.

2.1 Creating the Systems

Table 2.1. Parameters and symbols

N AND THE CONFIGURATION PARAMETERS	
number of stars in subcluster	N
standard deviation of $\log_{10}(M/\mathrm{M}_\odot)$	σ_ℓ
percentage of kinetic energy in ordered rotation	$\alpha_{\rm rot}$
rotation law: solid-body=SOL; Keplerian=KEP	$\alpha_{\rm law}$
mass segregation option	$\alpha_{\rm seg}$
Configuration, $[\sigma_\ell, \alpha_{\rm rot}, \alpha_{\rm law}, \alpha_{\rm seg}]$	$\mathcal{C}$
INITIALIZATION VARIABLES	
mass of star	M
$\log_{10}(m/\mathrm{M}_\odot)$ (random Gaussian deviate)	ℓ
random Gaussian deviates on $[-\infty, \infty]$	$\mathcal{G}$,$\mathcal{G}_\nu$
position of star	$\boldsymbol{r}$
	$[r, \theta_r, \phi_r]$
	$[x, y, z]$
random linear deviates on $[0, 1]$	$\mathcal{L}_r, \mathcal{L}_\theta, \mathcal{L}_\phi$
index for stellar ID	n
radius of subcluster centre of mass	$\boldsymbol{r}_{\rm COM}$
total mass of subcluster	$M_{\rm tot}$
gravitational potential energy	Ω

gravitational constant	G
initial rotational kinetic energy of subcluster	$E_{\rm rot}$
total kinetic energy of subcluster	$\mathcal{K}$
total orbital energy of the subcluster	$E_{\rm tot}$
random isotropic velocity	$\boldsymbol{v}_{\rm iso}$
dispersion in random isotropic velocity	$\sigma_{\rm iso}$
velocity of star	$\boldsymbol{v}$
	$[v, \theta_v, \phi_v]$
	$[v_x, v_y, v_z]$
bulk velocity of subcluster	$v_{\rm COM}$
rotational velocity	$\boldsymbol{v}_{\rm rot}$
moment of inertia about the z-axis	I_z
angular speed about the z-axis	ω
unit vector parallel to the z-axis	$\hat{\boldsymbol{e}}_z$
Kepler coefficient	κ
net angular momentum about the z-axis	H_z
linear momentum	$\boldsymbol{p}$
angular momentum	$\boldsymbol{H}$
Numerical Variables and Parameters	
acceleration	$\boldsymbol{a}$
time	t
interim step values	$k_{1,\boldsymbol{v}}, k_{2,\boldsymbol{v}}, k_{3,\boldsymbol{v}}, k_{4,\boldsymbol{v}}$
	$k_{1,\boldsymbol{r}}, k_{2,\boldsymbol{r}}, k_{3,\boldsymbol{r}}, k_{4,\boldsymbol{r}}$
integration stepsize	h
estimated change in velocity	$\Delta\boldsymbol{v}$
estimated change in position	$\Delta\boldsymbol{r}$
adaptive integration timestep	Δt
coefficient for integration timestep	γ
time-interval for monitoring multiplicity	$\Delta t_{\rm MMO}$
Orbital Parameters	
semi-major axis	a
orbital period	P
eccentricity	e
orbital inclination angle	θ_o
Scaling Parameters	
mean of $\log_{10}(m/{\rm M}_\odot)$	ℓ_0
radius of subcluster	R
factor to scale total mass of subcluster	f_M

factor to scale radius of subcluster	f_R

Five physical parameters are required to generate the initial conditions for a subcluster. The first is the number of stars in the subcluster, N. The remaining four physical parameters, $(\sigma_\ell,\, \alpha_{\rm rot},\, \alpha_{\rm law},\, \alpha_{\rm seg})$ are termed 'Configuration Parameters', and regulate – in a statistical sense – the distribution of stellar masses and the initial distribution of stars in phase space. In this section, I define the four Configuration Parameters and explain how they are implemented in setting up the initial conditions. They are also listed in the first section of Table 3.3, and they are all dimensionless.

2.1.1 Mass

The individual stellar masses, M, are generated from a log-normal distribution. I define:

$$\ell = \log_{10}\left(\frac{M}{\rm M_\odot}\right), \tag{2.1}$$

and calculate a value of ℓ using a gaussian random deviate $\mathcal{G}$

$$\ell = \ell_0 + \sigma_\ell \mathcal{G}, \tag{2.2}$$

where $\ell_{_0}$ defines the peak of the gaussian distribution and $\sigma_{_\ell}$ defines its log dispersion. Each stellar mass M is then given by

$$M = 10^\ell \, {\rm M_\odot}. \tag{2.3}$$

Here σ_ℓ is a Configuration Parameter, since it regulates the width of the mass distribution, i.e. the mean ratio between the most and least massive stars. While $\ell_{_0}$ regulates the mean mass, it is not a Configuration Parameter, as the results can be re-scaled to give any value of $\ell_{_0}$. The prescription for rescaling the code output is explained in Section 2.7.

2.1.2 Position

To start with, the stars are positioned randomly in a sphere of radius R using spherical polar coordinates. I select values of r, θ_r, and ϕ_r using three independent random linear deviates $\mathcal{L}_r$, $\mathcal{L}_{\theta,r}$, and $\mathcal{L}_{\phi,r}$ on the interval $[0, 1]$, where

$$r = R\mathcal{L}_r^{1/3}, \tag{2.4}$$

$$\theta_r = \cos^{-1}(2\mathcal{L}_{\theta,r} - 1), \tag{2.5}$$

$$\phi_r = 2\pi\mathcal{L}_{\phi,r}. \tag{2.6}$$

If $\alpha_{\rm seg} = 1$, the stars are mass-segregated along the radial axis. This is done by matching the masses and stellar radii such that the most massive star occupies the position of smallest radius, and the least massive the position of largest radius (i.e. for any pair of stars with IDs n and n', if $M_n < M_{n'}$, then $r_n > r_{n'}$). If $\alpha_{\rm seg} = 0$, the radii remain randomly assigned to the masses.

From here I transform the spherical coordinates into the cartesian reference frame:

$$x = r\sin(\theta_r)\cos(\phi_r), \tag{2.7}$$

$$y = r\sin(\theta_r)\sin(\phi_r), \tag{2.8}$$

$$z = r\cos(\theta_r). \tag{2.9}$$

Once the masses and positions are assigned, the centre of the Cartesian coordinate system is shifted to the centre of mass,

$$\boldsymbol{r}_n \longrightarrow \boldsymbol{r}_n - \boldsymbol{r}_{\rm COM}. \tag{2.10}$$

where

$$\boldsymbol{r}_{\rm COM} = \frac{1}{M_{\rm tot}} \sum_{n=1}^{n=N} \left\{ M_n \boldsymbol{r}_n \right\}, \tag{2.11}$$

and

$$M_{\rm tot} = \sum_{n=1}^{n=N} \left\{ M_n \right\}. \tag{2.12}$$

.

The initial self-gravitational potential energy,

$$\Omega = -G \sum_{n=1}^{n=N-1} \sum_{n'=n+1}^{n'=N} \left\{ \frac{M_n\, M_{n'}}{|\boldsymbol{r}_n - \boldsymbol{r}_{n'}|} \right\}, \tag{2.13}$$

is also computed.

R is not a Configuration Parameter, since the results can be re-scaled to any subcluster radius.

2.1.3 Velocity

The last two Configuration Parameters regulate the kinetic energy and spatial distribution of the stars in the subcluster. $\alpha_{\rm rot}$ dictates the percentage of kinetic energy that is in ordered rotation, as opposed to random isotropic velocity dispersion

$$\alpha_{\rm rot} = \frac{E_{\rm rot}}{\mathcal{K}}. \tag{2.14}$$

$\mathcal{K}$ is the total kinetic energy:

$$\mathcal{K} = \frac{1}{2}\sum_{n=1}^{n=N} M_n |\boldsymbol{v_n}|^2. \tag{2.15}$$

At this juncture, the stars are given random isotropic velocities, $\boldsymbol{v}_{\rm iso}$, drawn from a Maxwellian distribution with zero mean and standard deviation

$$\sigma_{\rm iso} = \sqrt{[1-\alpha_{\rm rot}]\frac{\Omega}{6M_{\rm tot}}}, \tag{2.16}$$

where $M_{\rm tot}$ is the total mass of the subcluster. I select a gaussian random deviate $\mathcal{G}_\upsilon$ on the interval $[-\infty, +\infty]$ and two linear random deviates ($\mathcal{L}_{\theta.\upsilon}$, $\mathcal{L}_{\phi,\upsilon}$) on the interval $[0, 1]$, using these values to obtain velocities in the spherical frame

$$\upsilon = \sigma_{\rm iso}\,\mathcal{G}_\upsilon, \tag{2.17}$$

$$\theta_\upsilon = \cos^{-1}(2\mathcal{L}_{\theta,\upsilon} - 1), \tag{2.18}$$

$$\phi_\upsilon = 2\pi\mathcal{L}_{\phi,\upsilon}. \tag{2.19}$$

Transforming to cartesian,

$$\upsilon_x = \upsilon\sin(\theta_\upsilon)\cos(\phi_\upsilon), \tag{2.20}$$

$$\upsilon_y = \upsilon\sin(\theta_\upsilon)\sin(\phi_\upsilon), \tag{2.21}$$

$$\upsilon_z = \upsilon\cos(\theta_\upsilon). \tag{2.22}$$

These velocities are then shifted to the centre-of-mass frame by calculating the subcluster bulk velocity,

$$\boldsymbol{v}_{_{COM}} = \frac{1}{M_{_{TOT}}}\sum_{n=1}^{n=N}\left\{M_n\boldsymbol{v}_n\right\}, \tag{2.23}$$

subtracting from the stellar velocities,

$$\boldsymbol{v}_n \longrightarrow \boldsymbol{v}_n - \boldsymbol{v}_{_{COM}} \tag{2.24}$$

and renormalising to correct the total kinetic energy invested in isotropic velocity dispersion.

If $\alpha_{\rm rot} > 0$, the stars are also given ordered rotation velocities, $\boldsymbol{v}_{\rm rot}$, where $\alpha_{\rm law}$ dictates the rotation law. If $\alpha_{\rm law} = \rm SOL$ the rotation is solid-body and the rotational exponent is 1. The moment of inertia about the z-axis, angular speed about the z-axis,

and velocity are thus assigned respectively as

$$\left.\begin{array}{rcl} I_z & = & \sum\limits_{n=1}^{n=N}\{M_n|\hat{\boldsymbol{e}}_z\wedge\boldsymbol{r}_n|^2\}, \\ \omega & = & [\alpha_{\rm rot}\Omega/I_z]^{1/2}, \\ \boldsymbol{v}_{{\rm rot}:n} & = & \omega\ \hat{\boldsymbol{e}}_z\wedge\boldsymbol{r}_n\,, \end{array}\right\}\ \text{if } \alpha_{\rm law}={\rm SOL}\,; \tag{2.25}$$

where $\hat{\boldsymbol{e}}_z$ is the unit vector parallel to the z-axis and $\wedge$ denotes a vector product. Alternatively, if $\alpha_{\rm law}={\rm KEP}$ the rotation is Keplerian and the rotational exponent is $-\frac{1}{2}$. The moment of inertia about the z-axis, Kepler coefficient, and velocity now scale with $\boldsymbol{r}_n^{-1/2}$, and are assigned respectively as

$$\left.\begin{array}{rcl} I'_z & = & \sum\limits_{n=1}^{n=N}\{M_n|\hat{\boldsymbol{e}}_z\wedge\boldsymbol{r}_n|^{-1}\}, \\ \kappa & = & [\alpha_{\rm rot}\Omega/I'_z]^{1/2}, \\ \boldsymbol{v}_{{\rm rot}:n} & = & \kappa\ |\hat{\boldsymbol{e}}_z\wedge\boldsymbol{r}_n|^{-3/2}\ \hat{\boldsymbol{e}}_z\wedge\boldsymbol{r}_n, \end{array}\right\}\ \text{if } \alpha_{\rm law}={\rm KEP}. \tag{2.26}$$

The net velocities of the stars,

$$\boldsymbol{v}_n=\boldsymbol{v}_{{\rm iso}:n}\ +\ \boldsymbol{v}_{{\rm rot}:n}, \tag{2.27}$$

are then computed and shifted (again) to the centre-of-mass frame.

Finally the initial total kinetic energy is computed and the velocities are re-scaled to ensure that the subcluster is virialised,

$$\boldsymbol{v}_n \longleftarrow \boldsymbol{v}_n\ \sqrt{\frac{\Omega}{2\mathcal{K}}}. \tag{2.28}$$

Because of this rescaling, the specific choice of velocity dispersion $\sigma_{\rm iso}$ in Eq. 2.17 is inconsequential.

I chose to use an initially virialised subcluster for two reasons. First, the timescale on which the subcluster approaches virial equilibrium is likely to be short compared with the timescale on which the multiplicity statistics stabilise. Second, this reduces the number of free parameters to explore.

2.1.4 Flattening

In the original form of the experiment, I included a flattening parameter, $\alpha_{\rm disk}$, which produced a flattened, disk-like spatial distribution of stars. This parameter was disregarded from results, as it produced no statistically-significant affect on the end systems. However, I will outline the prescription for this flattening.

If $\alpha_{\rm disk} = 1$, the positions of the stars are flattened in the z-direction such that

$$z \longleftarrow z\left[1 + \frac{3\alpha_{\rm rot}}{2}\right]^{-1}. \tag{2.29}$$

The velocities are also modified accordingly:

$$v_z \longleftarrow v_z\left[1 + \sqrt{\frac{3\alpha_{\rm rot}}{2}}\right]^{-1}. \tag{2.30}$$

Equations 2.29 and 2.30 are not exact solutions, rather they approximate the expected behaviour of a rotating cloud by parameterizing the flattening as a function of the degree of ordered rotation.

The rotational velocity must be rescaled such that the chosen values reproduce the desired value of $\alpha_{\rm rot}$. For this, I calculate the net angular momentum about the z-axis

$$H_z = \sum_{n=1}^{n=N} M_n(xv_{tot,y} - yv_{tot,x}) \tag{2.31}$$

and moment of inertia about the z-axis

$$I_z = \sum_{n=1}^{n=N} M_n(x^2 + y^2) \tag{2.32}$$

to find the rotational energy

$$E_{rot} = \frac{H_z^2}{2I_z}. \tag{2.33}$$

Thus the new $\alpha'_{\rm rot}$ is given by

$$\alpha'_{\rm rot} = \frac{E_{rot}}{E_{\rm kin}}. \tag{2.34}$$

The rotational velocity is modified as follows:

$$v_{rot} \longleftarrow v_{rot}\sqrt{\frac{\alpha_{\rm rot}}{\alpha'_{\rm rot}}}. \tag{2.35}$$

The sequence from 2.27 through 2.28, and 2.31 through 2.35 is repeated until $\alpha'_{\rm rot}$ satisfies the condition

$$\alpha_{\rm rot:tol} > |\alpha'_{\rm rot} - \alpha_{\rm rot}|. \tag{2.36}$$

The default value of the tolerance parameter is set to $\alpha_{\rm rot:tol} = 0.1$.

2.1.5 System Parameters

I use the shorthand

$$\mathcal{C} \equiv [\sigma_\ell,\, \alpha_{\rm rot},\, \alpha_{\rm law},\, \alpha_{\rm seg}] \tag{2.37}$$

to represent a specific set of Configuration Parameters. Apart from N and $\mathcal{C}$, the only other variables that distinguish one experiment from another are the random-number seeds used to generate different realisations of the same N and same set of Configuration Parameters, $\mathcal{C}$.

2.2 Evolving the System

To time-evolve the point-mass star clusters, I wrote a 4th order Runge-Kutte Ordinary Differential Equation solving algorithm (RK4). For each of the coupled differential equations of gravitational motion of acceleration:

$$\boldsymbol{a} = \frac{d\boldsymbol{v}}{dt}, \tag{2.38}$$

and velocity:

$$\boldsymbol{v} = \frac{d\boldsymbol{r}}{dt}, \tag{2.39}$$

I calculate four interim step values k_1, k_2, k_3, and k_4 according to a given stepsize h:

$$k_{1,\boldsymbol{v}} = h\boldsymbol{a}(\boldsymbol{r}) \tag{2.40}$$
$$k_{1,\boldsymbol{r}} = h\boldsymbol{v} \tag{2.41}$$
$$k_{2,\boldsymbol{v}} = h\boldsymbol{a}(\boldsymbol{r} + \frac{k_{1,\boldsymbol{r}}}{2}) \tag{2.42}$$
$$k_{2,\boldsymbol{r}} = h[\boldsymbol{v} + \frac{k_{1,\boldsymbol{v}}}{2}] \tag{2.43}$$
$$k_{3,\boldsymbol{v}} = h\boldsymbol{a}(\boldsymbol{r} + \frac{k_{2,\boldsymbol{r}}}{2}) \tag{2.44}$$
$$k_{3,\boldsymbol{r}} = h[\boldsymbol{v} + \frac{k_{2,\boldsymbol{v}}}{2}] \tag{2.45}$$
$$k_{4,\boldsymbol{v}} = h\boldsymbol{a}(\boldsymbol{r} + k_{3,\boldsymbol{r}}) \tag{2.46}$$
$$k_{4,\boldsymbol{r}} = h[\boldsymbol{v} + k_{3,\boldsymbol{v}}]. \tag{2.47}$$

They are then weighted and added together to calculate the estimated velocity and position at the next step:

$$\Delta \boldsymbol{v} = \frac{1}{6}[k_{1,\boldsymbol{v}} + 2k_{2,\boldsymbol{v}} + 2k_{3,\boldsymbol{v}} + k_{4,\boldsymbol{v}}] \tag{2.48}$$

$$\Delta \boldsymbol{r} = \frac{1}{6}[k_{1,\boldsymbol{r}} + 2k_{2,\boldsymbol{r}} + 2k_{3,\boldsymbol{r}} + k_{4,\boldsymbol{r}}]. \tag{2.49}$$

This algorithm estimates the equations of gravitational motion to the 4th order, which provides a high level of accuracy during stellar close encounters, when energy conservation is most likely to be lost in N-body simulations. Other N-body codes such as nbody6, which is employed in the AMUSE package (Portegies Zwart, 2011), use lower-order algorithms such as the Leapfrog-Verlet 3rd order ODE solver. This is because general N-body codes are designed to balance precision with efficiency for high N. Since this code is designed for relatively small N values, I employ an RK4 for its greater accuracy. I do not find this choice to be time-prohibitive – the computational runtime to evolve a two-body system $\sim$ 1 Myr on a Mac M1 chip is $\sim$ 0.3 s.

To increase time-efficiency and conservation of angular momentum throughout the evolution, I incorporated an algorithm to adapt the evolutionary timestep, Δt. For each stellar pair at each new step of the integrator, the algorithm takes the magnitude change in relative position over relative velocity, and the magnitude change in relative velocity over relative acceleration. Δt is calculated as a fraction of the smallest of these values.

$$\Delta t = \gamma \ \mathrm{MIN}\left\{ \frac{|\boldsymbol{r}_n - \boldsymbol{r}_{n'}|}{|\boldsymbol{v}_n - \boldsymbol{v}_{n'}|}, \frac{|\boldsymbol{v}_n - \boldsymbol{v}_{n'}|}{|\boldsymbol{a}_n - \boldsymbol{a}_{n'}|} \right\}_{n \neq n'} \tag{2.50}$$

where $\boldsymbol{r}_n, \boldsymbol{v}_n$, and $\boldsymbol{a}_n$ are the position, velocity, and acceleration of star n, respectively.

Δt is then used for the next step of the integration. Here γ is a user-specified parameter determining the accuracy of the integration. This formulation ensures that the largest fractional change in relative position or relative velocity of any two stars in one timestep is $\sim \gamma$. As stars move closer to one another, conservation of energy is maintained, and as stars move further apart and less precision is needed, computational time is conserved. The numerical experiments presented in the thesis have been performed with $\gamma = 0.1$.

Each initial system is integrated for a maximum of 1000 crossing times ($t_{\rm cr}$), where

$$t_{\rm cr} = \sqrt{\frac{R^3}{GM_{\rm tot}}}, \tag{2.51}$$

unless all the existing systems become unbound from one another, in which case the integration is terminated at a time $t < 1000\ t_{cr}$ in order to save computer time (see Section 2.4).

2.3 Identifying Binary and Higher-Order Multiples

At regular intervals, $\Delta t_{\rm MMO}$, during the cluster evolution, I identify multiple systems using a Multiplicity Monitoring Operation, hereafter MMO. The MMO selects a random pair of stars in the subcluster – If the stars in this pair [1] are mutual nearest neighbours, and [2] have negative energy in their mutual centre of mass frame, they are identified as bound. For the purposes of the MMO, the bound pair is then treated as a single object with the properties (mass, position, velocity) of its center of mass. This object is added to the pairing procedure, and its individual constituent stars are removed from this iteration of the MMO. Conversely, if the pair do not meet both criteria [1] and [2], they remain as individual stars, and the MMO checks a different possible pairing. This continues recursively until the full inventory of multiple systems in the subcluster has been determined.

Through this procedure, the MMO identifies all stellar systems which have formed at that $\Delta t_{\rm MMO}$, the multiplicity of each system, its architecture (*i.e.* planetary vs 2+2 quadruple), as well as which specific stars occupy which orbit. For each identified bound system – including higher-order multiples – the procedure calculates the orbital parameters: semi-major axis (a), orbital period (P), eccentricity (e), and angular momentum vector (which gives the orbital inclination vector with angle θ_o). The MMO is implemented every 33 crossing times ($\sim 2.3\,{\rm Myr}\,N^{-1/2}$, or $\sim 1\,{\rm Myr}$ for $N = 4\ or\ 5$). By running at many intervals throughout the integration, the MMO is able to track the evolution of system multiplicity and architecture. Note that, after an MMO implementation, the integration procedure continues to follow all stars as individuals.

2.1 shows the evolution of an example $N = 4$ subcluster. At all four MMO timesteps shown, the MMO identifies a "planetary" quadruple with a central pairing made up of the two most massive stars (0.64 $M_\odot$ and 0.37 $M_\odot$). In the first two $\Delta t_{\rm MMO}$, the 0.25 $M_\odot$ star occupies the third orbit in the hierarchy, and the 0.24 $M_\odot$ star is a distant fourth. Between the second and third $\Delta t_{\rm MMO}$, the outer two stars exchange places in the hierarchy.

2.4 Unbound Stars and Stopping Conditions

During the evolution, a star or system may become unbound from the rest of the subcluster. It is then no longer necessary to track its position, and it is removed from further evolution of the subcluster (and from subsequent MMO implementations). However, during periods of frequent close encounters two stars that are actually bound to one another may not meet condition [1] (*i.e.* may briefly not be mutual nearest neighbours). This only occurs occasionally, and only ever in the very early lifetime of a subcluster when the dynamics is very chaotic. To avoid inadvertently removing bound stars or systems from the evolution, stars and systems are only removed after the first 4

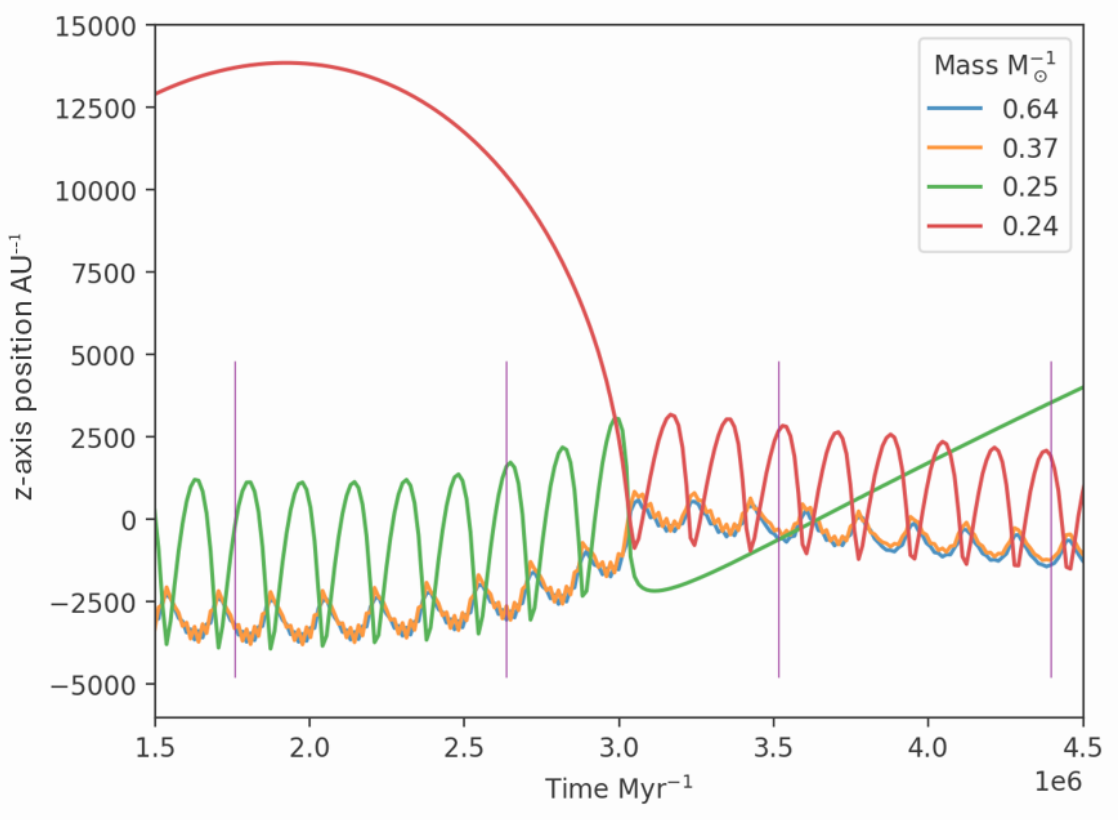

Figure 2.1. The trajectory of each member of a 4 star subcluster as projected onto the z-axis. The subcluster centre of mass lies at the origin. Monitoring timesteps are marked with purple vertical lines. At all four MMO timesteps shown, the MMO identifies a "planetary" quadruple with a central pairing made up of the two most massive stars (0.64 $M_\odot$ and 0.37 $M_\odot$). In the first two Δt_{MMO}, the 0.25 $M_\odot$ star forms a third and the 0.24 $M_\odot$ star is a distant fourth. Between the second and third Δt_{MMO}, the outer two stars exchange places in the hierarchy.

$\Delta t_{\rm MMO}$, and only if those stars or systems have remained unbound for two consecutive MMOs.

If the MMO finds that the subcluster consists entirely of singles and binaries, no further dynamical change can take place and the evolution is halted.

2.5 Output

The code outlined above calculates a significant number of values at a large number of timesteps. Many, but not all, of these data are valuable for analysis. To keep files as compact as possible, organize the data, and cull unnecessary information, I constructed three output files: stellar information, orbital information, and subcluster information.

Stellar information: This file stores information on the movement of the individual stars in each realized subcluster. Each star is identified by its mass and a label number, which is given by the star's mass rank within its subcluster. The cartesian position and velocity vectors, along with the dimensionalized time, are written every 0.5 crossing times. While the position and velocity are calculated for every evolutionary timestep Δt, the 0.5 crossing time resolution is high enough to represent the general movements of most systems without creating prohibitively-large output files. The stellar output files for $N = 7$ do not exceed 1.7 GB each. To investigate the detailed movements of a particular system, one can simply rerun that realization and store the output at a higher time resolution.

Orbital Information: This file stores the information about each orbit identified by the MMO. For each $\Delta t_{\rm MMO}$, the MMO establishes a hierarchy of orbits and calculates the parameters of those orbits. For each subcluster orbit at each $\Delta t_{\rm MMO}$, I store the labels of the inner object (which could be a single star or another orbit), the outer object (which could likewise be a star or orbit), a label for this new orbit, and its orbital parameters: mutual orbital inclination, eccentricity, semimajor axis, and period.

Subcluster Information: This file stores information about the subcluster as a whole. At each $\Delta t_{\rm MMO}$, the code writes the dimensionalized time, the multiplicity of all systems in the subcluster, and the number of close orbits which are not the central pair of their system, as in a 2+2, 3+2, 3+3, etc. configuration.

This file is also where the total kinetic energy and total potential energy of the subcluster are stored for energy conservation checks.

2.6 Checks

Total orbital energy $E_{\rm tot}$, linear momentum $\boldsymbol{p}$, and angular momentum $\boldsymbol{H}$,

$$E_{\rm tot} = \mathcal{K} + \Omega, \tag{2.52}$$

$$\boldsymbol{p} = M\boldsymbol{v}, \tag{2.53}$$

$$\boldsymbol{H} = \boldsymbol{r} \wedge \boldsymbol{p} \tag{2.54}$$

are conserved in real, isolated gravitational systems which are not subject to external forces, but errors can accumulate in numerical methods such as RK4.

Figure, 2.2 shows $\mathcal{K}$, Ω, and $E_{\rm tot}$ over time for an example $N = 3$ subcluster. For all subclusters in the example Configuration $N = 3$, $\mathcal{C}(\sigma_\ell = 0.3, \alpha_{\rm rot} = 0, \alpha_{\rm seg} = 0)$, The median change in normalized relative energy over the course of a simulation, $\Delta E_{\rm tot} = |E_{\rm tot,final} - E_{\rm tot,0}|/(|\mathcal{K}_0| + |\Omega_0|)$, is 0.3%. Deviations in total linear momentum are negligible – while individual values of linear momentum are of order $|\boldsymbol{p}| = 10^{-3}$, $|\boldsymbol{p}_{\rm tot}|$ is of the order 1E-18, arising from the 15-decimal place precision of 64-bit floats. Angular momentum drifts slightly: $97(\pm 2)\%$ of subclusters complete the integration with a fractional change in total angular momentum of $< 5\%$. As the focus of this work is the gravitational evolution of subclusters using the global statistics produced by many realizations, small error accumulation ($< 5\%$) does not meaningfully impact the results. If the focus were on the dynamical evolution of individual, real-world systems such as Earth-Moon-Sun, tighter error restrictions might be necessary.

2.7 Scaling

The numerical experiments described in the paper are strictly speaking dimensionless, and have only been scaled so that the centre of the mass distribution corresponds to M$= 0.25$ M$_\odot$ and the subcluster radius to $R = 10^3\,{\rm AU}$ for the purpose of illustration. To scale a given experiment to a subcluster with a different total mass, M'_{tot}, and/or a different radius, R', one must multiply all stellar and system masses by

$$f_{_M} = \frac{M'_{\rm tot}}{M_{\rm tot}}; \tag{2.55}$$

all position vectors and orbital axes by

$$f_{_R} = \frac{R'}{R}\,; \tag{2.56}$$

the time and all orbital periods by

$$\sqrt{\frac{f_{_R}^3}{f_{_M}}}; \tag{2.57}$$

and all velocities by

$$\sqrt{\frac{f_{_M}}{f_{_R}}}. \tag{2.58}$$

Orbital eccentricities and inclinations are unchanged.

One potential use of these rescaling relations could be to modify the mass distribution to study subclusters dominated by different spectral types.

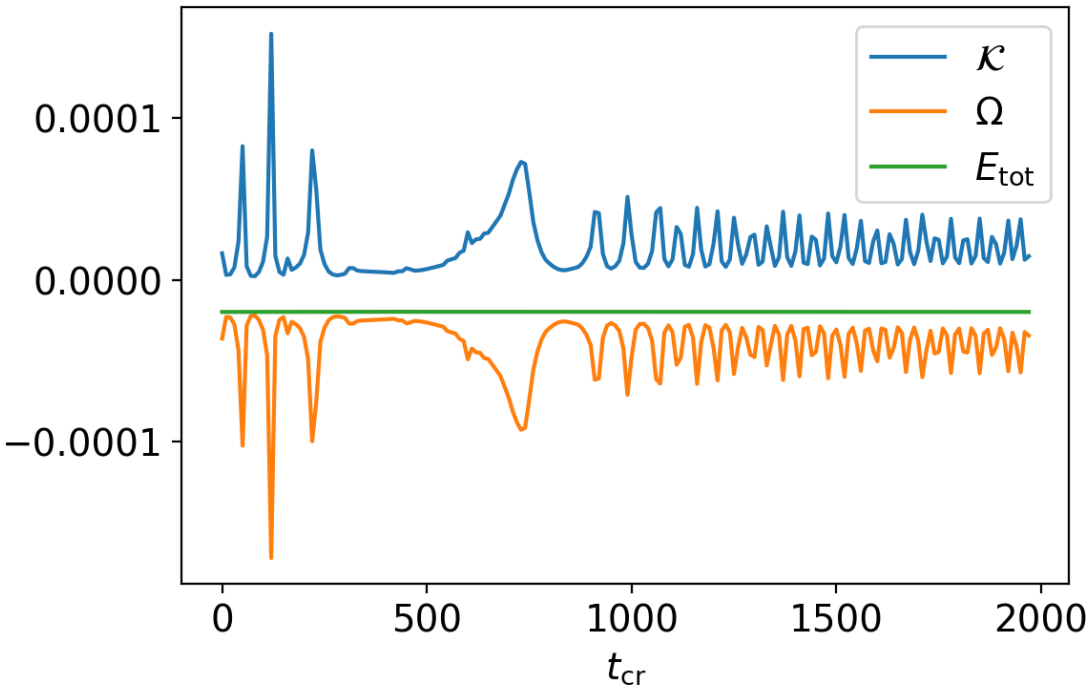

Figure 2.2. Kinetic, gravitational potential, and total orbital energy over the full integration time for an example 3-star subcluster. The x-axis is given in dimensionless crossing times and the y-axis in dimensionless energy.

Chapter 3

The formation of multiples in small-*N* subclusters

In this chapter, I explore the multiplicity achieved through the evolution of small, isolated subclusters of N stars. The goal of this experiment is to understand what initial conditions best reproduce observed multiplicity. I use the method outlined in Chapter 2 to initialise, evolve, and determine the characteristics of small-N stellar subclusters. I also introduce a prescription for mixing the multiplicity statistics from realizations of different N. By comparing the mixed experimental statistics with observations, I find a best mix of Configuration Parameters and distribution of N to reproduce the main-sequence multiplicity statistics of solar-mass primary systems.

3.1 Initial Conditions

I evolve an ensemble of stellar subclusters using pure gravitational dynamics. The subclusters are initially characterised by the number of stars they contain, N, and four Configuration Parameters described in Chapter 2. These are:

- σ_ℓ, defined in Equation 2.2, the standard deviation of the log-normal distribution of stellar masses, hereafter termed the 'mass range'. I explore values in the range $0.2 \leq \sigma_\ell \leq 0.4$, but focus here on results obtained with $\sigma_\ell = 0.3$.*

- $\alpha_{\rm rot}$, Equation 2.14, the fraction of kinetic energy in ordered rotation. The rest is in random velocities drawn from an isotropic Maxwellian distribution. I consider values of $\alpha_{\rm rot}$ ranging from 0 to 0.99, or no rotation to virtually all kinetic energy in ordered rotation.

- $\alpha_{\rm law}$, the rotation law. This is either Keplerian (Equation 2.26, KEP), or solid-body (Equation 2.25, SOL).

*Lower values of σ_ℓ result in too few binaries with low mass-ratios, q. Higher values result in an IMF that is too much broader than the CMF.

Table 3.1. Parameters and symbols

multiplicity of system	m
maximum multiplicity considered	$m_{\max}$
percentage of singles ($m=1$)	S
percentage of binaries ($m=2$)	B
percentage of triples ($m=3$)	T
percentage of higher-order systems ($m\geq 4$)	Q^{+}
mean number of systems with multiplicity m formed by a single subcluster with Configuration $\mathcal{C}$ that contains N stars	$\mathcal{S}_{\mathcal{C}Nm}$
probability that a core spawns N stars	$\mathcal{P}_{\mathcal{D}N}$
normalisation coefficient for $\mathcal{P}_{\mathcal{D}N}$ (see Eqn. 3.2)	$\eta_{\mathcal{D}}$
parameter for $\mathcal{P}_{\mathcal{D}N}$ (see Eqn. 3.1)	$\Delta N_{\mathcal{D}}$
parameter for $\mathcal{P}_{\mathcal{D}N}$ (see Eqn. 3.1)	$N_{\mathcal{D}}$
mean of N for $\mathcal{P}_{\mathcal{D}N}$ (see Eqn. 3.3)	$\mu_{\mathcal{D}}$
standard deviation of N for $\mathcal{P}_{\mathcal{D}N}$ (see Eqn. 3.4)	$\sigma_{\mathcal{D}}$
N-distribution, $[N_{\mathcal{D}},\ \Delta N_{\mathcal{D}}]$	$\mathcal{D}$
frequency of system of multiplicity m resulting from Configuration $\mathcal{C}$ and N-Distribution $\mathcal{D}$	$f_{\mathcal{C}\mathcal{D}m}$
observed number of systems with multiplicity m	$\mathcal{O}_m$
quality of fit to observations with Configuration $\mathcal{C}$ and N-distribution $\mathcal{D}$	$\mathcal{Q}_{\mathcal{C}\mathcal{D}}$
total number of systems with multiplicity m predicted for Configuration $\mathcal{C}$ and N-distribution $\mathcal{D}$	$\mathcal{N}_{\mathcal{C}\mathcal{D}m}$
percentage of stars with $m \geq 3$	$f_{\mathrm{T}^{+}}$

- $\alpha_{\rm seg}$, which determines whether the stars are mass-segregated ($\alpha_{\rm seg}=1$) or not ($\alpha_{\rm seg}=0$). Star positions are generated randomly within a uniform-density sphere with radius $R_{\rm o}$ if $\alpha_{\rm rot}=0$, and within a uniform-density oblate spheroid with semi-major axis $R_{\rm o}$ if $\alpha_{\rm rot}>0$. See section 2.1.2.

For the number of stars, N, I explore subclusters with $3 \leq N \leq 7$. Subclusters of $N=1,2$ are of course possible, but I do not need to evolve these cases – their multiplicity output cannot be changed by pure internal dynamical evolution. I stop consideration after $N=7$ for two reasons: it is prohibitive to keep track of all the different possible outcomes; and such large N are likely to be rare.

All subclusters start in Virial Equilibrium, and for each combination of N and *C*onfiguration Parameters (σ_ℓ, $\alpha_{\rm rot}$, $\alpha_{\rm law}$, $\alpha_{\rm seg}$) I evolve 1000 realisations for a maximum of 1000 $t_{\rm cr}$, where $t_{cr} \sim 0.07\,{\rm M}yr\,N^{-1/2}$

For the purpose of illustration, I set: (i) the mean of the log-normal distribution of masses to $\mu_\ell=-0.6$ so that the median stellar mass is $M_{\rm med}=0.25\,{\rm M}_\odot$; and (ii) the radius (or semi-major axis) of the initial spherical (or oblate spheroidal) envelope to $R_{\rm o}=1000\,{\rm AU}$. However the equations regulating the evolution of a pure n-body subcluster are dimensionless, so the results can be rescaled arbitrarily according to Section 2.7.

In order to understand how subcluster-scale dynamical interactions shape long-term stellar multiplicity, I limit the experiment to point-mass stars and their gravitational forces. I do not include ambient gas, (therefore there is no stellar accretion or gravitational softening), stellar mass loss, collisions and mergers, or external forces.

3.2 Mixing *N* Statistics

For each set of Configuration Parameters, $\mathcal{C}$ listed in Table 3.3, and number of stars, $3 \leq N \leq 7$, I compute the mean number of systems with multiplicity m, $\mathcal{S}_{\mathcal{C}Nm}$, formed from each of the 1000 realisations. m is taken in the range $1 \leq m \leq m_{\rm max}=4^+$. Because the numbers of quintuples, sextuples and septuples are small (both in the numerical experiments, and in the observations), they are simply added to the quadruples to give $\mathcal{S}_{\mathcal{C}N4^+}$.

To fit the observations, I assume that the probability that a core spawns a subcluster of N stars is given by the distribution function

$$\mathcal{P}_{\mathcal{D}N} = \eta_{\mathcal{D}}\,MAX\Big(\Big\{\Delta N_{\mathcal{D}}^2 - [N-N_{\mathcal{D}}]^2\Big\},\,0\Big), \tag{3.1}$$

$$\eta_{\mathcal{D}} = 1 \Big/ \sum_{N=1}^{N=7} MAX\Big(\Big\{\Delta N_{\mathcal{D}}^2 - [N-N_{\mathcal{D}}]^2\Big\},\,0\Big), \tag{3.2}$$

where $\eta_{\mathcal{D}}$ is a normalisation coefficient. This function creates a truncated discrete parabolic curve defined on the range $1 \leq N \leq 7$. Because N is not a continuous variable, $N_{\mathcal{D}}$ regulates, but is not exactly, the mean of the N distribution; and $\Delta N_{\mathcal{D}}$ regulates, but is not exactly, the standard deviation of the N distribution. The true mean and standard deviation are given by

$$\mu_{\mathcal{D}} = \sum_{N=1}^{N=7} \{\mathcal{P}_{\mathcal{D}N}\, N\}\,, \tag{3.3}$$

$$\sigma_{\mathcal{D}}^2 + \mu_{\mathcal{D}}^2 = \sum_{N=1}^{N=7} \left\{\mathcal{P}_{\mathcal{D}N}\, N^2\right\}. \tag{3.4}$$

The subscript $\mathcal{D}$ in Equations 3.1 through 3.4 represents the parameters of the distribution function, i.e.

$$\mathcal{D} \equiv [N_{\mathcal{D}},\, \Delta N_{\mathcal{D}}]\,, \tag{3.5}$$

hereafter the N-Distribution.

The frequency with which a subcluster having Configuration Parameters $\mathcal{C}$ and N-distribution $\mathcal{D}$ spawns a multiple system of order m is

$$f_{\mathcal{C}Dm} = \sum_{N=1}^{N=7} \{\mathcal{P}_{\mathcal{D}N}\, \mathcal{S}_{\mathcal{C}Nm}\}\,. \tag{3.6}$$

Therefore, if the observed number of systems with multiplicity m is $\mathcal{O}_m$, the predicted number is

$$\mathcal{N}_{\mathcal{C}Dm} = f_{\mathcal{C}Dm} \sum_{m=1}^{m=4^+} \{\mathcal{O}_m\} \Big/ \sum_{m=1}^{m=4^+} \{f_{\mathcal{C}Dm}\}\,, \tag{3.7}$$

and the quality of fit for this combination of Configuration Parameters, $\mathcal{C}$, and N-Distribution, $\mathcal{D}$, is given by

$$\mathcal{Q}_{\mathcal{C}D} = \sum_{m=1}^{m=4^+} \left\{\frac{[\mathcal{N}_{\mathcal{C}Dm} - \mathcal{O}_m]^2}{\mathcal{O}_m^2}\right\} \tag{3.8}$$

A lower value of $\mathcal{Q}_{\mathcal{C}D}$ represents a better fit.

3.3 Results and Discussion

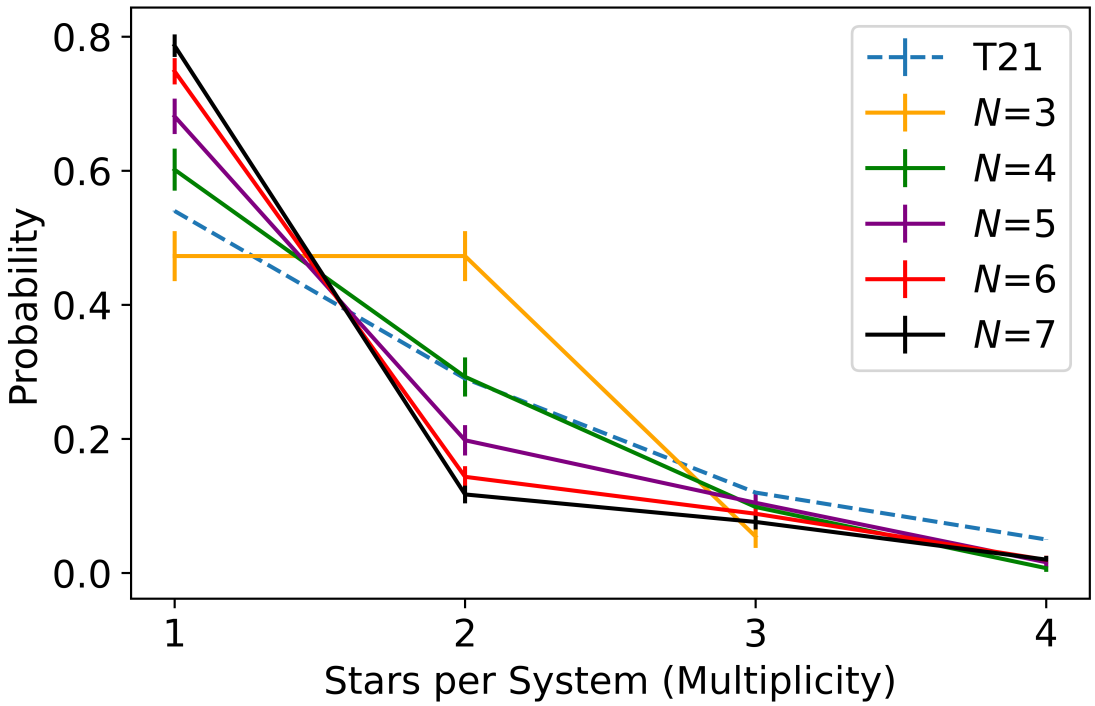

Figure 3.1. Multiplicity distributions for subclusters with $N = 3$ (yellow), 4 (green), 5 (purple), 6 (red) and 7 (black). For each N-value I have evolved 1000 different realisations with the fiducial Configuration Parameters ($\alpha_{\rm rot} = 0$, $\alpha_{\rm seg} = 0$). The blue dashed line represents the T21 sample. Error bars represent the 3σ statistical variance.

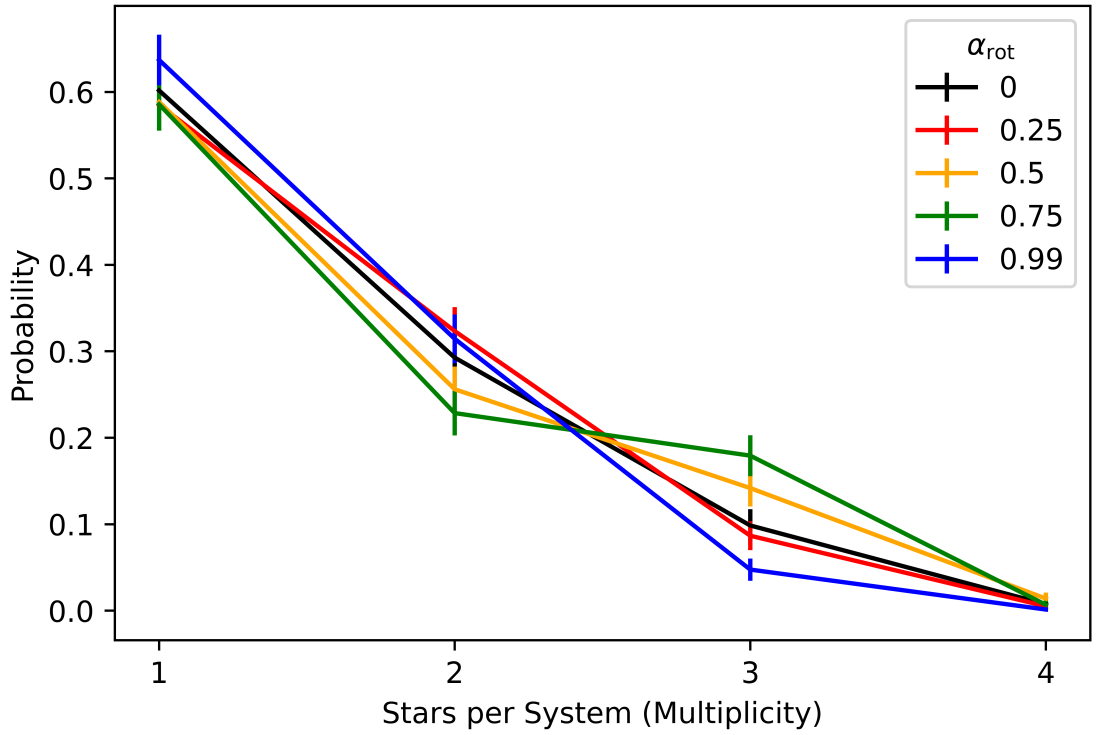

Figure 3.2. Multiplicity distributions for subclusters with $N = 4$, $\alpha_{\rm seg} = 1$, and different values of $\alpha_{\rm rot} = 0$ (black), 0.25 (red), 0.5 (yellow), 0.75 (green), and 0.99 (blue). For each $\alpha_{\rm rot}$ value I have evolved 1000 different realisations. Error bars represent the 3σ statistical variance.

Table 3.2. The Configurations evaluated, and the quality and parameters of the best fit. Column 1, Configuration ID; Columns 2 through 4, the amount of rotation, the rotation law, and whether there is mass segregation; Columns 5 and 6, the N-Distribution Parameters, $(N_{\mathcal{D}}, \Delta N_{\mathcal{D}})$; Columns 7 and 8, the mean and standard deviation of the N-Distribution; Column 9, the quality of the best fit (small for a good fit); Columns 10 through 13, the percentages of singles, S, binaries, B, triples, T, and quadruples plus higher orders, Q^+; Column 14, the total number of systems produced; Columns 15 through 18, the multiplicity fraction (MF, Equation 3.9), the triple and higher-order fraction (f_{T^+}, Equation 1.4), the companion fraction (CF, Equation 3.10), and the plurality (PL, Equation 3.11). Row 1, the parameter symbols; Row 2, the observed statistics from the T21 sample (Tokovinin, 2021); Rows 3 through 5, the results from Sterzik & Durisen (1998) for subclusters with a single $N = 3$, 4 and 5; Rows 6 through 10, the results from this work for subclusters with a single $N = 3$, 4, 5, 6 and 7; Row 11, the fiducial case (no rotation, no segregation); Rows 12 through 15, the solid-body rotation cases; Rows 16 and 17, the Keplerian rotation cases; Rows 18 through 22, the mass-segregated cases (including the best-fit case, SEG4).

$\mathcal{C}$	$\alpha_{\rm rot}$	$\alpha_{\rm law}$	$\alpha_{\rm seg}$	$N_{\mathcal{D}}$	$\Delta N_{\mathcal{D}}$	μ_{D}	σ_{D}	$\mathcal{Q}_{\mathcal{C}D}$	S	B	T	Q^{+}	Sys	MF	$f_{\rm T+}$	CF	PL
T21	0	–	–						54	29	12	5		0.46	0.17	0.68	1.13
SD3	0	–	0	3	0				46.8	46.8	5.5	0	1,878	0.53	0.06	0.59	0.82
SD4	0	–	0	4	0				62.7	29.1	6.0	1.1	2,713	0.36	0.07	0.44	0.74
SD5	0	–	0	5	0				70.1	18.9	9.0	0.9	3,475	0.29	0.10	0.40	0.75
N=3	0	–	0	3	0	3	0	1.71	47.3	47.3	5.45	0	1,614	0.53	0.05	0.58	0.80
N=4	0	–	0	4	0	4	0	0.77	60.2	29.3	9.85	0.73	2,194	0.40	0.11	0.51	0.84
N=5	0	–	0	5	0	5	0	0.65	68.1	19.8	10.5	1.61	2,798	0.32	0.12	0.46	0.84
N=6	0	–	0	6	0	6	0	0.84	74.8	14.3	8.84	1.96	4,377	0.25	0.11	0.38	0.76
N=7	0	–	0	7	0	7	0	1.06	78.7	11.7	7.62	2.00	5,290	0.21	0.10	0.33	0.70
FID	0	–	0	4.9	1.0	4.8	0.1	0.64	67.1	21.0	10.4	1.49	16,273	0.33	0.12	0.46	0.84
SOL1	0.25	SOL	0	5.0	1.0	5.0	0.0	0.57	66.2	21.7	10.4	1.7	17,104	0.34	0.12	0.48	0.86
SOL2	0.50	SOL	0	4.3	3.3	4.4	2.1	0.41	62.6	24.3	11.1	2.0	16,599	0.37	0.13	0.53	0.91
SOL3	0.75	SOL	0	4.4	3.4	4.4	2.2	0.49	63.8	23.1	11.3	1.78	16.714	0.36	0.13	0.51	0.90
SOL4	0.99	SOL	0	4.9	1.0	4.8	0.1	1.26	70.3	23.7	5.65	0.38	17,829	0.30	0.06	0.36	0.63
KEP1	0.50	KEP	0	4.4	3.4	4.4	2.2	0.42	63.5	23.6	10.8	2.08	16,715	0.36	0.13	0.51	0.90
KEP2	0.99	KEP	0	5.0	1.0	5.0	0.0	1.22	71.2	21.8	6.57	0.38	17,992	0.29	0.07	0.36	0.64
SEG1	0	–	1	5.0	1.0	5.0	0.0	0.63	67.1	20.6	10.8	1.53	16,590	0.33	0.12	0.47	0.85
SEG2	0.50	SOL	1	5.3	1.6	5.2	0.5	0.43	66.1	21.0	10.6	2.29	16,574	0.34	0.13	0.49	0.89
SEG3	0.99	SOL	1	4.6	1.1	4.6	0.2	1.38	69.5	25.9	4.31	0.33	17,869	0.31	0.05	0.36	0.60
SEG4	0.50	KEP	1	5.4	4.4	4.8	2.4	0.35	63.2	24.1	10.3	2.41	16,339	0.27	0.13	0.52	0.91
SEG5	0.99	KEP	1	4.8	1.0	4.7	0.2	1.33	69.9	25.1	4.59	0.41	17,995	0.30	0.05	0.36	0.61

The numerical experiments suggest that most cores spawn 4 or 5 stars. There are cores that spawn 3 stars, but if they were the norm they would produce too many binaries and too few singles, while contributing no quadruples or higher-order systems. Conversely, there are cores that spawn more than 5 stars, but if they were the norm they would produce too many singles and too few binaries. Although such high-N cores are essential to produce the high-order systems, this pure n-body model does not produce as many high-order systems as are observed; I find that increasing N is more effective at over-producing singles than it is at producing stable higher-order multiples. In fact, only 3 of the $N = 7$ experimental realizations resulted in lasting 7-star systems (see Appendix A for details). In Section 3.3.4.1 I suggest that forming the observed number of high-order systems probably requires the inclusion of additional physics such as disc drag and disc fragmentation, since this will deliver compact, tightly bound companions that can survive all but the closest interactions with other stars.

3.3.1 A universal *N* value

It is informative to consider the possibility that all cores spawn the same number of stars, i.e. a universal N value, although a universal N is extremely unlikely. For these experiments I use the fiducial parameters, i.e. no rotation and no mass-segregation.

An initially-bound subcluster with $N=3$ stars has $\mathcal{A}_3 = 2$ possible end-states: (i) a triple system, or (ii) a binary and a single star. Because the dissolution of a 3-star subcluster into a binary and a single is the only way for a binary or a single star to form from such a subcluster, the percentages of single and binary systems must be equal in this case. For the fiducial case, in which the initial subcluster has no ordered rotation or mass segregation, $\sim 90\%$ of 3-star subclusters decay into a binary and a single, giving percentages of S:B:T:Q$^+$ = 47:47:6:0, exactly as obtained by Sterzik & Durisen (1998).

An initially-bound subcluster with $N=4$ stars has $\mathcal{A}_4 = 4$ possible end-states: (i) a quadruple; (ii) a triple and a single star; (iii) two separate binaries; or (iv) a binary and two single stars. For the fiducial case, $N=4$ gives S:B:T:Q$^+$ = 60:29:10:7. Note that higher-order multiples may come in different variants. For example, there are '2+2' quadruples and planetary quadruples.

Of the quadruple systems produced in the $N=4$ fiductial, $25(\pm14)\%$ are '2+2' systems and the remainder are planetary. In contrast, in the Tokovinin 2014 sample $\sim 75\%$ of quadruples are '2+2' systems. There are two possible explanations for this discrepancy. First, because '2+2' systems feature two close pairs on one larger orbit (Fig. 1.1b), they are likely easier to detect through spectroscopic and eclipse methods, which favour close orbits (see Section 1.2), making them overrepresented in the observational sample. This is in comparison to 'planetary' quadruples (Fig 1.1c), whose outermost companions orbit much farther from the singular inner pair. These outer companions are also more likely to be low-mass due to dynamical biasing, (see section 1.6), faint,

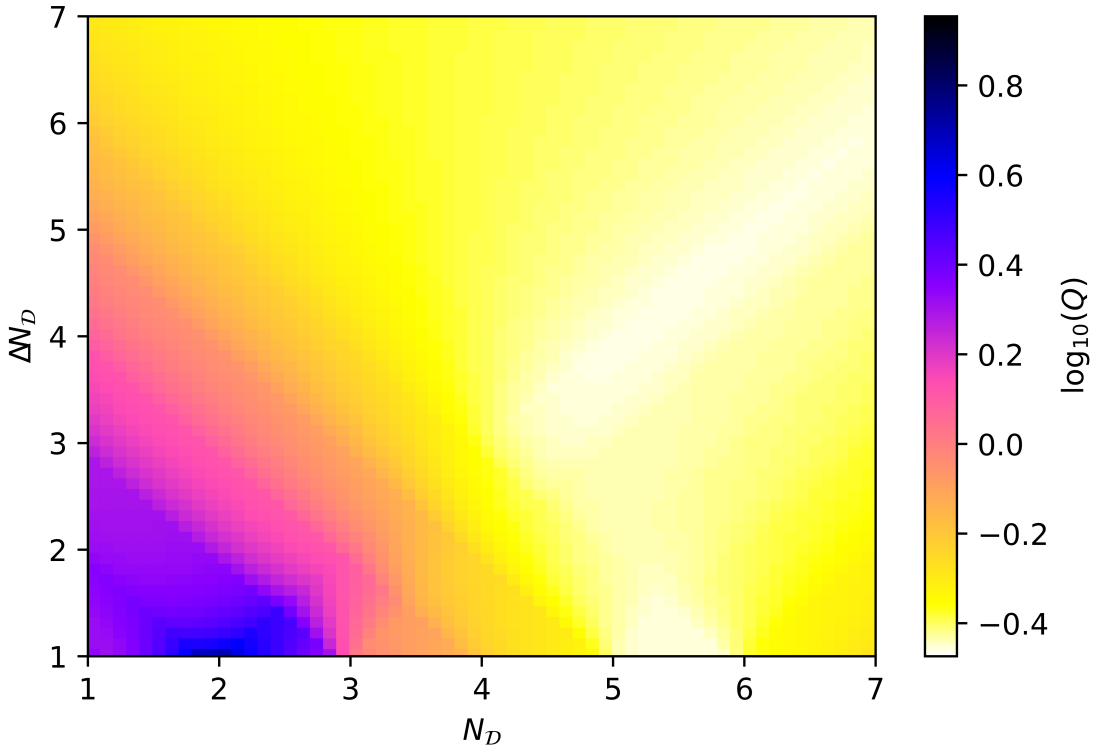

Figure 3.3. Map of the Quality Factor, $\mathcal{Q}_{\mathcal{C}D}$, for the best-fit Configuration Parameters SEG4 ($\alpha_{\rm rot} = 0.50$, $\alpha_{\rm law} =$ KEP, $\alpha_{\rm seg} = 1$) and the full range of N-Distribution Parameters ($1.0 \leq N_{\mathcal{D}} \leq 7.0$ and $1.0 \leq \Delta N_{\mathcal{D}} \leq 7.0$). The colour encodes $\log_{10}(\mathcal{Q}_{\mathcal{C}D})$, with the best fits white, very bad fits purple, and the worst fit ($N_{\mathcal{D}} = 2$ and $\Delta N_{\mathcal{D}} = 1$) black.

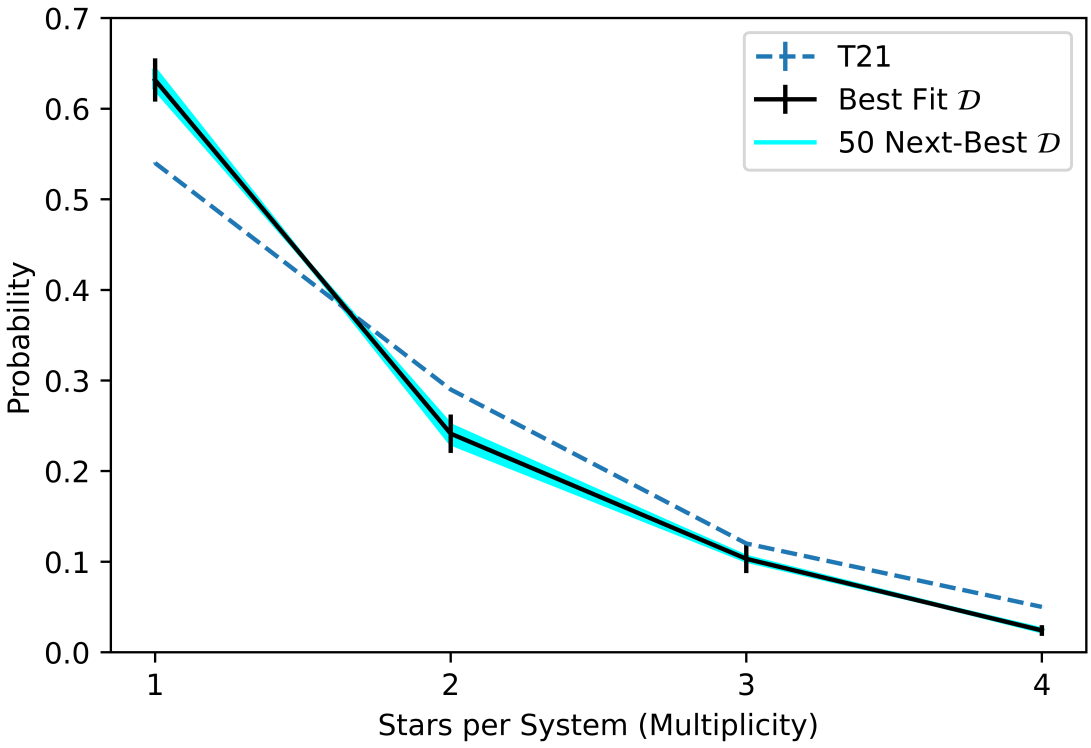

Figure 3.4. Multiplicity distributions. The blue dashed curve represents the T21 sample. The black full line represents the absolute best-fit combination of Configuration Parameters and N-Distribution Parameters (i.e. SEG4, one from bottom row in Table 3.3). The surrounding cyan represents fits for the same Configuration Parameters and the 50 next-best-fits with different N-Distribution Parameters (corresponding to the whitest region on Fig. 3.3).

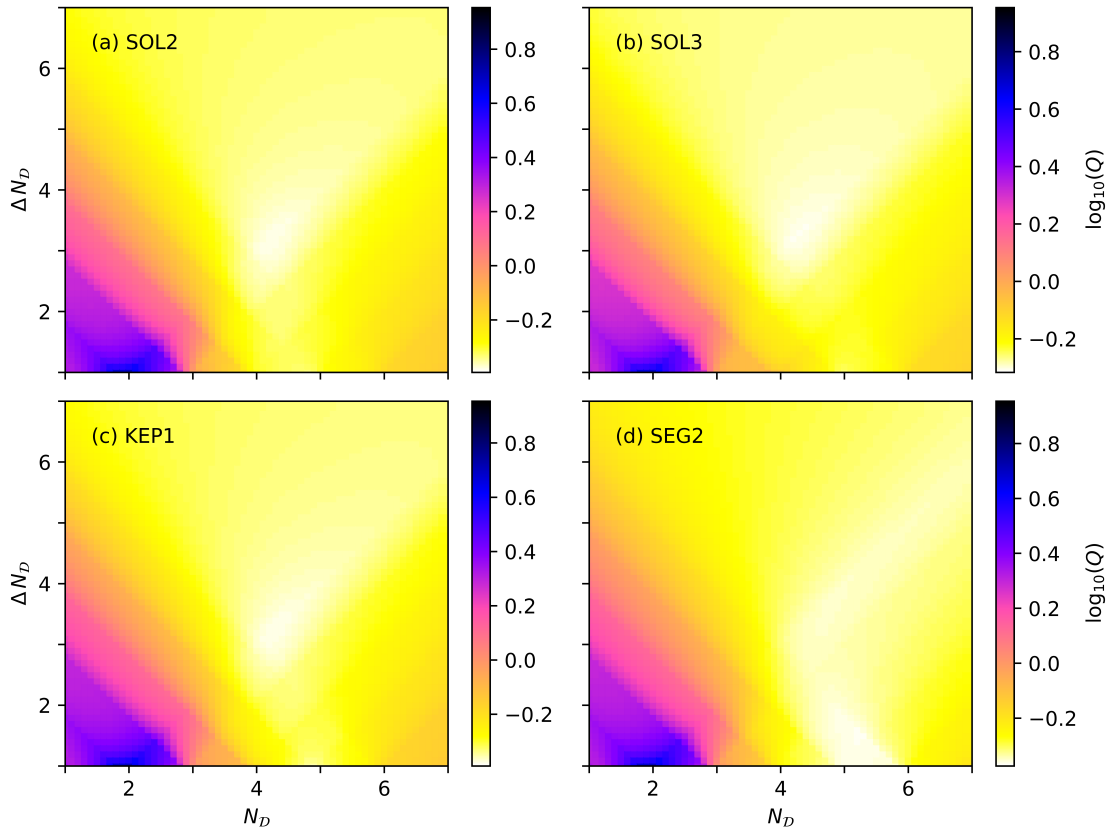

Figure 3.5. As Fig. 3.3, but for the Configuration Parameters giving the second through fifth best fits (i.e. the other fits with $\mathcal{Q}_{cD} < 0.50$): (a) SOL2 with $\mathcal{Q}_{cD} = 0.41$; (b) SOL3 with $\mathcal{Q}_{cD} = 0.49$; (c) KEP1 with $\mathcal{Q}_{cD} = 0.42$; and (d) SEG2 with $\mathcal{Q}_{cD} = 0.43$.

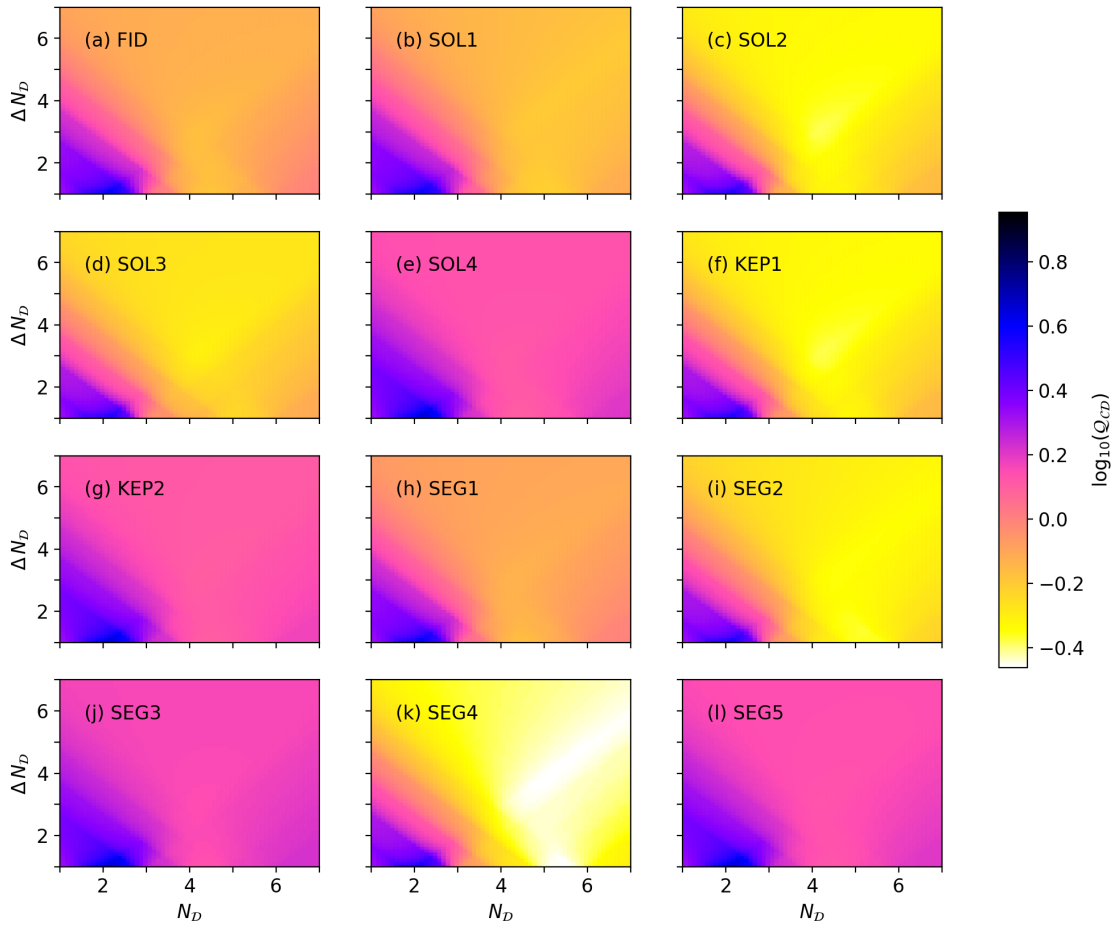

Figure 3.6. As Fig. 3.3, but for all Configuration Parameters on a single color mapping.

and thus missed by wide orbit detection methods (see Section 1.2). Second, it may be that additional physics that is missing from our numerical experiments – for example, circumstellar accretion discs and disc fragmentation – increases the percentage of '2+2' quadruples.

The number of distinguishable end-states increases monotonically with N. 5-star subclusters have $\mathcal{A}_5 = 6$ possible end-states, and 6-star subclusters have $\mathcal{A}_6 = 10$ possible end-states. For the fiducial case, $N=5$ gives S:B:T:Q$^+$ = 68:20:10:2, with $24(\pm8)\%$ of Q$^+$ systems composed wholly, or in part, of '2+2' configurations; and $N=6$ gives S:B:T:Q$^+$ = 75:14:9:2, with $24(\pm6)\%$ of Q$^+$ systems containing '2+2' configurations.

An initially-bound subcluster with $N=7$ stars has $\mathcal{A}_7 = 14$ possible end-states: (i) a septuple; (ii) a sextuple and a single star, (iii) a quintuple and a binary, (iv) a quintuple and two singles, (v) a quadruple and a triple, (vi) a quadruple, a binary, and a single, (vii) a quadruple and three singles, (viii) two triples and a single, (ix) a triple and two binaries, (x) a triple, a binary, and two singles, (xi) a triple and four singles, (xii) three binaries and a single, (xiii) two binaries and three singles, (xiv) a binary and five singles. Given the rapid increase in the number of end-states with increasing N, I limit consideration to $N \leq 7$. For the fiducial case, $N=7$ gives S:B:T:Q$^+$ = 79:12:8:2, with $19(\pm5)\%$ of Q$^+$ systems containing '2+2' configurations. I explore the change in number of possible end states with N in Chapter 5, and develop a formula for its calculation.

Figure 3.1 displays the multiplicity distributions for the fiducial case with different values of N. The results for $N=4$ most accurately match the T21 sample, but no value exactly reproduces the observed multiplicities. Increasing N does increase the probability of forming higher-order multiples. Indeed, a system with multiplicity $m \geq 3$ can only form if $N \geq m$. However, this effect is small, and the main effect of increasing N is to increase the percentage of singles at the expense of binaries. These singles are mainly lower-mass stars that have been ejected by the sling-shot mechanism.

For subclusters with a universal N value the multiplicity statistics can be changed quite significantly by introducing rotation. Figure 3.2 shows the effect of different amounts of rotation for subclusters with $N=4$. The remaining 3 Configuration parameters: mass range, type of rotation, and mass segregation, have no statistically-significant effect on the universal N-value multiplicity statistics.

3.3.2 A distribution of *N* values

Since it is unlikely that every prestellar core produces the same number of stars, I also calculate the experimental statistics for distributions of N values. I identify the combinations of Configuration Parameters, $\mathcal{C}$, and N-Distribution, $\mathcal{D}$, that best fit the observations. The N-Distributions are given by Equation 3.1, and I test all combinations

of $N_{\mathcal{D}}$ = 1.0, 1.1, 1.2, 1.3, . . . 6.8, 6.9, 7.0, and $\Delta N_{\mathcal{D}}$ = 1.0, 1.1, 1.2, 1.3, . . . 6.8, 6.9, 7.0.

Table 3.3 lists all the tested Configurations $\mathcal{C}$; for each Configuration, the parameters of the N-Distribution giving the best fit to the T21 sample; and – where they exist – the corresponding parameters from Sterzik & Durisen (1998).

3.3.2.1 The notional absolute-best fit

The notional absolute-best fit is obtained with Configuration $\mathcal{C}$ = SEG4 ($\alpha_{\rm rot} = 0.5$, $\alpha_{\rm law} = \textsc{kep}$, $\alpha_{\rm seg} = 1$) and an N-Distribution with $(N_{\mathcal{D}}, \Delta N_{\mathcal{D}}) \simeq (5.4, 4.4)$ (corresponding to mean $\mu_{\mathcal{D}} \simeq 4.8$, and standard deviation $\sigma_{\mathcal{D}} \simeq 2.4$). This delivers percentages S:B:T:Q$^+$ = $63 : 24 : 10 : 2.4$, with Quality Factor $\mathcal{Q}_{\mathcal{C}D} = 0.35$ and $41(\pm5)\%$ of Q$^+$ systems containing '2+2' orbits.

3.3.2.2 How critical is the *N*-Distribution?

Figure 3.3 is a map of the Quality Factor, $\mathcal{Q}_{\mathcal{C}D}$, for Configuration $\mathcal{C}$ = SEG4 over the full range of N-Distribution parameters, $(N_{\mathcal{D}}, \Delta N_{\mathcal{D}})$. There are two regions of low $\mathcal{Q}_{\mathcal{C}D}$ (i.e. good fits, represented by white on Fig. 3.3). One is centred on the best fit $(N_{\mathcal{D}}, \Delta N_{\mathcal{D}}) \simeq (5.4, 4.4)$ with an extension to higher and lower values of $N_{\mathcal{D}}$ and $\Delta N_{\mathcal{D}}$. The other, slightly less-favoured region, is centred on $(N_{\mathcal{D}}, \Delta N_{\mathcal{D}}) \simeq (5.5, 1)$.

Figure 3.4 compares the multiplicities corresponding to the absolute-best fit (black line) and the fifty next-best fits (i.e. SEG4 with slightly different N-Distributions; cyan shading). These fits correspond to the whitest region on Figure 3.3 (specifically, an area that is $\sim 1.4\%$ of the total area of Fig. 3.3). They all fall within one standard deviation of the absolute-best fit, so the parameters of the N-Distribution giving the absolute-best fit are not highly critical.

Notably, but unsurprisingly, a prestellar core producing exactly 2 stars results in the worst fit, since it only produces binary systems. The corresponding black point on Figure 3.3 is only just visible next to the abscissa.

3.3.2.3 Which are the critical Configuration Parameters?

Table 3.4 lists the five Configurations that produce fits with, $\mathcal{Q}_{\mathcal{C}D} < 0.5$.

Figure 3.5 shows the Quality Factor, $\mathcal{Q}_{\mathcal{C}D}$, for the four additional Configurations and the full range of N-Distribution parameters, $(N_{\mathcal{D}}, \Delta N_{\mathcal{D}})$. Panels (c) SOL2, (d) SOL3, and (f) KEP1 on Fig. 3.5 are very similar to one another, with a single region of high quality, centred on $(N_{\mathcal{D}}, \Delta N_{\mathcal{D}}) \simeq (4.4, 3.4)$. Panel (i) SEG2 is more like SEG4 (Figure 3.3), with two regions, but the preferred region is now the lower one centred on $(N_{\mathcal{D}}, \Delta N_{\mathcal{D}}) = (5.3, 1.6)$.

Table 3.4. The parameters of the five best fits, i.e. those with Quality Factor, $\mathcal{Q}_{\mathcal{CD}} < 0.5$. Reading left to right, the columns give the configuration name, the parameters of the configuration ($\alpha_{\rm rot}$, $\alpha_{\rm law}$, $\alpha_{\rm seg}$), the mean and standard deviation of the distribution of N values ($\mu_{\mathcal{D}}$, $\sigma_{\mathcal{D}}$), the Quality Factor ($\mathcal{Q}_{\mathcal{CD}}$), and the percentage of Q^+ systems that contain '2+2' orbits.

$\mathcal{C}$	$\alpha_{\rm rot}$	$\alpha_{\rm law}$	$\alpha_{\rm seg}$	$\mu_{\mathcal{D}}$	$\sigma_{\mathcal{D}}$	$\mathcal{Q}_{\mathcal{CD}}$	'2+2'
SOL2	0.50	SOL	0	4.4	2.1	0.41	$25(\pm06)$
SOL3	0.75	SOL	0	4.4	2.2	0.49	$26(\pm06)$
KEP1	0.50	KEP	0	4.4	2.2	0.42	$28(\pm05)$
SEG2	0.50	SOL	1	5.2	0.5	0.43	$44(\pm07)$
SEG4	0.50	KEP	1	4.8	2.4	0.35	$41(\pm05)$

All five Configurations involve rotation, four with 50% of the kinetic energy invested in rotation, and one with 75%. I conclude that having comparable amounts of energy in rotation and in random isotropic motions is a critical requirement for producing a good fit to observed statistics.

In contrast, three of the top-five Configurations have solid-body rotation, while two have Keplerian rotation. I conclude that the details of the rotation law are not critical. Similarly three of the top-five configurations have no mass segregation, and two of them do. Therefore it appears that mass segregation is also not a critical requirement for a good fit.

Figure 3.6 compares all Configurations over the full range of N-Distribution parameters using a single colour scale. All Configurations with low or now rotation – panels (a) FID, (b) SOL1, and (h) SEG1 – give poor fits, and all high-rotation Configurations – panels (e) SOL4, (g) KEP2, (j) SEG3, and (l) SEG5 – give the poorest fits, regardless of rotation type or mass segregation. This again supports the conclusions that moderate rotation is critical to reproducing observations, while type of rotation and mass segregation are not.

The mass segregation does appear to have an affect on the formation of '2+2' systems. While the percentage of '2+2's is similar for the best-fit cases with no segregation ($\alpha_{seg} = 0$), those that begin with segregated masses ($\alpha_{seg} = 1$) have a much higher percentage of '2+2's (Table 3.4).

3.3.3 Metrics of overall multiplicity

Various metrics of overall multiplicity have been proposed, in particular the *multiplicity fraction* (i.e. the fraction of systems that are not single),

$$\mathrm{MF} = \frac{\mathrm{B+T+Q+...}}{\mathrm{S+B+T+Q+...}}\,; \tag{3.9}$$

the *triple/higher-order fraction* (i.e. the fraction of systems that are triple or higher-order, see Equation 1.4); the *companion fraction* (i.e. the mean number of companions per primary),

$$\mathrm{CF} = \frac{\mathrm{B} + 2\mathrm{T} + 3\mathrm{Q} + ...}{\mathrm{S} + \mathrm{B} + \mathrm{T} + \mathrm{Q} + ...}\,; \tag{3.10}$$

and the *p*lurality (i.e. the mean number of companions per star, irrespective of whether it is a primary star),

$$\mathrm{PL} = \frac{2\mathrm{B} + 6\mathrm{T} + 12\mathrm{Q} + ...}{\mathrm{S} + 2\mathrm{B} + 3\mathrm{T} + 4\mathrm{Q} + ...}\,. \tag{3.11}$$

These metrics are given in the last four columns of Table 3.3. The last one, PL, has the merit that it has a clear physical meaning and reflects, more strongly than the others, the percentage of higher-order multiples. CF and PL can both be greater than one. Indeed, for the T21 sample, PL $= 1.13$, and it is likely to be even higher for high-mass primaries.

3.3.4 Caveats

3.3.4.1 Pure *n*-body dynamics

The numerical experiments reported here involve pure n-body dynamics. Consequently – modulo numerical errors – the resulting multiplicities are determined solely by the initial conditions and gravitational interactions between point masses. Because gravity is a time-reversible process, N-star subclusters which end the experiment with one system of multiplicity N (i.e. they undergo no ejections) fall into two categories: either the initial subcluster begins in a stable (hierarchical) configuration, or the simulation ends before the subcluster has reached its final state. Meta-stable systems will eventually dissolve into more than one system. I explore the metastable population of the experiment in Chapter 4.

Phenomena such as dissipation from the cloud or disc, which harden systems against dissolution and act to increase stellar multiplicity, are not considered. I expect the pure n-body results of this work to represent a conservative (i.e. low) estimate of the multiplicity which can be achieved from a subcluster of N stars.

3.3.4.2 Isolated subclusters

Each subcluster is evolved in isolation. The subcluster cannot capture outside stars, nor can it be perturbed by stellar flybys. For low-N subclusters, capture might increase the multiplicity metrics (e.g. MF, CF and PL). But for high-N subclusters, perturbations by stellar flybys would be likely to reduce the multiplicity metrics, for example by disrupting hierarchical triples.

3.3.4.3 Duration of integration

Subclusters are evolved for a maximum of 1000 crossing times. In practice most of the final multiple systems are established early in the evolution, within the first 200 crossing times. For the $N = 7$ case, whose systems take the longest to settle into their end states, more than 80% of instantiations achieve their final $1000\,t_{cr}$ multiplicities by $200\,t_{\rm cr}$, and more than 95% by $600\,t_{cr}$.

3.3.4.4 Limited number of stars in subcluster

I do not consider subclusters with $N > 7$. As N increases, the multiplicity distribution changes at a decreasing rate (see Figure 3.1): the percentages of binaries and triples decrease slightly, the percentage of singles increases, and the percentages of higher-order multiples ($m \geq 4$) increase imperceptibly. For example, in the fiducial case, the multiplicity distributions for $N = 6$ and 7 agree within their 3σ uncertainties (Figure 3.1). This is true for all configurations tested. I expect multiplicities for values of $N > 7$ to follow this trend, remaining very similar to the multiplicity values for $N = 7$.

In addition, the complexity of possible end states increases dramatically with N (see Chapter 5]), making higher-N numerical experiments prohibitive from a book-keeping standpoint.

3.3.4.5 Observational statistics

The T21 observational statistics are probably influenced by selection effects , which are introduced in relation to detection method and discussed for the T21 sample in Section 1.2. Historically, many detection methods such as RV and eclipse have been likely to miss low-luminoisty systems and unequal-mass companions. High-precision data such as GAIA measurements have enabled observers to detect new companions to previously-considered single stars, along with new companions to known multiples (e.g. Thomas et al. 2023; Mugrauer et al. 2023). Because higher precision allows for the detection of lower-luminosity and more unequal-mass systems, further technological advancements will likely function to increase multiplicity estimates and the proportion of higher-order systems. As the completeness of multiplicity surveys improves, the analysis presented in this chapter can easily be reapplied to updated observational statistics. However, the inability of this pure n-body model to produce enough higher-order systems is likely to remain a limitation.

3.3.4.6 Summary

I have used n-body numerical experiments to determine the multiplicity statistics that result from small-N subclusters of stars that interact only through their mutual gravity. These statistics have then been compared with the T21 sample of nearby systems

with solar-mass primaries (Tokovinin, 2021). The subclusters are presumed to be the product of collapse and fragmentation in a single isolated prestellar core.

To produce an acceptable fit to the observed statistics, prestellar cores must – on average – spawn between 4.3 and 5.2 stars. This seems to be a rather compelling conclusion, in the sense that firstly it produces by far the best fit to the observations, and secondly a very similar conclusion has been drawn by two other, completely independent studies, *viz.* [1] Holman et al. (2013) using statistical arguments, and [2] Lomax et al. (2015b) using SPH simulations. I stress that neither [1] nor [2] involves n-body numerical experiments, and they are therefore totally independent of the results reported here.

In the numerical experiments reported in this work, subclusters which begin with roughly half their kinetic energy invested in rotation produce the best fits to the T21 sample. Furthermore there is a broad range of setups that produce very similar fits, but they all have roughly half their kinetic energy invested in rotation. These setups do occasionally spawn fewer than four stars, or more than five, but this is relatively rare. The multiplicity statistics appear to be independent of whether the subcluster starts with a solid-body or Keplerian rotation law, and of whether the masses are initially segregated.

Although the overall fits obtained here are quite good, there are always too few systems with multiplicity $m \geq 4$. I believe that this is because these stars do not have circumstellar discs. Such discs will make close encounters between stars dissipative, thereby increasing the formation of tight orbits and higher-order multiples. Such discs may also fragment to form close companions, some of which will survive interactions with other stars in the subcluster, and again this will promote the formation of higher-order multiples.

Chapter 4

Orbital statistics of multiple systems formed from small-N subclusters

In this chapter, I analyse the orbital parameters of the multiple systems identified in the numerical experiments of Chapter 3. These parameters are: semi-major axes, a; the extent of Dynamical Biasing; mass ratios, q_1 and q_2; numbers of companions; mutual orbital inclinations, θ_o; eccentricities, e; masses and ejection velocities, $v_{\rm ej}$. I term these Orbital Statistics, to distinguish them from the Multiplicity Statistics reported in Chapter 3. I compare the Orbital Statistics from different N and Configuration Parameters, with a focus on the Fiducial and Best Fit cases defined in Chapter 3. I also introduce a naming convention to distinguish types of orbits.

4.1 Architectures of Multiple Systems

A system with multiplicity m comprises m stars and $m-1$ orbits. Most of the parameters I discuss in the following chapter describe an orbit. If both the objects on either end of the orbit are stars, I classify the orbit as S2; if only one is a star, as S1; and if neither is a star, as S0.

A binary consists of a single S2 orbit.

A stable (and therefore hierarchical) triple comprises an S2 orbit and a larger S1 orbit; the S2 orbit involves a pair of stars orbiting one another, and the S1 orbit involves this pair and a third star orbiting one another.

A quadruple may comprise an S2 orbit and two S1 orbits, in which case it is classed as a *Planetary Quadruple*; the S2 orbit involves a pair of stars orbiting one another, the

Table 4.1. Additional orbital parameters

binary mass ratio	q_1
tertiary mass ratio	q_2
stellar escape velocity	$v_{\rm ej}$
ratio of outer to inner semi-major axis	$\mathcal{R}_a$
initial random kinetic energy of subcluster	$E_{\rm ran}$

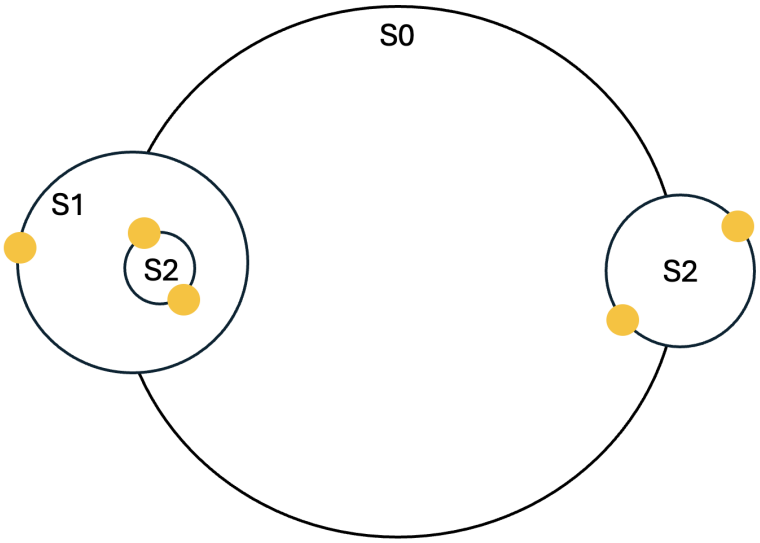

Figure 4.1. An example orbital configuration – a 3+2 quintuple – made up of S2, S1, and S0 orbits.

first S1 orbit involves this pair and a third star orbiting one another, and the second S1 orbit involves this threesome and a fourth star orbiting one another. Alternatively a quadruple may comprise two S2 orbits and one S0 orbit, in which case it is classed as a *2+2 Quadruple*; each of the S2 orbits involves a different pair of stars orbiting one another, and the S0 orbit involves the two pairs orbiting one another.

Figure 4.1 illustrates an example configuration, a 3+2 quintuple, which demonstrates all three types of orbits.

For the purpose of evaluating statistical distributions I distinguish S2 orbits from S1 orbits, and I do not consider S0 orbirts, since they are too rare to support reliable statistics.

4.2 Results

I have selected two main cases from Chapter 3 with which to illustrate the *Orbital Statistics*. In both I fix $\sigma_\ell = 0.3$, since this is the value that is most consistent with the mapping from the prestellar Core Mass Function to the stellar Initial Mass Function (Whitworth, Ambrose & Georgatos, in prep.).

- The first case is the *Fiducial Case*. It has $\alpha_{\rm rot} = 0$, therefore there is no ordered rotation and $\alpha_{\rm law}$ is irrelevant. It also has $\alpha_{\rm seg} = 0$, meaning no mass segregation. I present results for $N = 3$, 4, 5, 6 and 7. With $N = 1$ all stars are single, and with $N = 2$ all stars are in binaries, since the subcluster is virialised from the outset.

- The second case is the *Best-Fit Case*. This is the case identified in Chapter 3 which best reproduces the *Multiplicity Statistics* for solar-mass primaries from T21. It has a distribution of N values with mean $\mu_N = 4.8$ and standard deviation $\sigma_N = 2.4$. The Configuration Parameters are $\alpha_{\rm rot} = 0.5$ and $\alpha_{\rm law} = {\rm KEP}$ (moderate Keplerian rotation) and $\alpha_{\rm seg} = 1$ (mass segregation). Further details of the Best-Fit case can be found in Chapter 3, section 2.5.

- Some dependencies are better illustrated by considering parameter values other than those of the *Fiducial* and *Best-Fit Cases*. These are discussed in separate subsections. Section 4.2.1.3 deals with the dependence of semi-major axes on the amount of ordered rotation ($\alpha_{\rm rot}$). Section 4.2.4.3 deals with how the mutual orbital inclinations depend on the amount of ordered rotation ($\alpha_{\rm rot}$).

4.2.1 The Distribution of Semi-Major Axes

4.2.1.1 Semi-major axes in the Fiducial Case

Figures 4.2a and 4.2b show that in the *Fiducial Case* the semi-major axes of S2 orbits tend to decrease with N, whereas the semi-major axes of S1 orbits are roughly

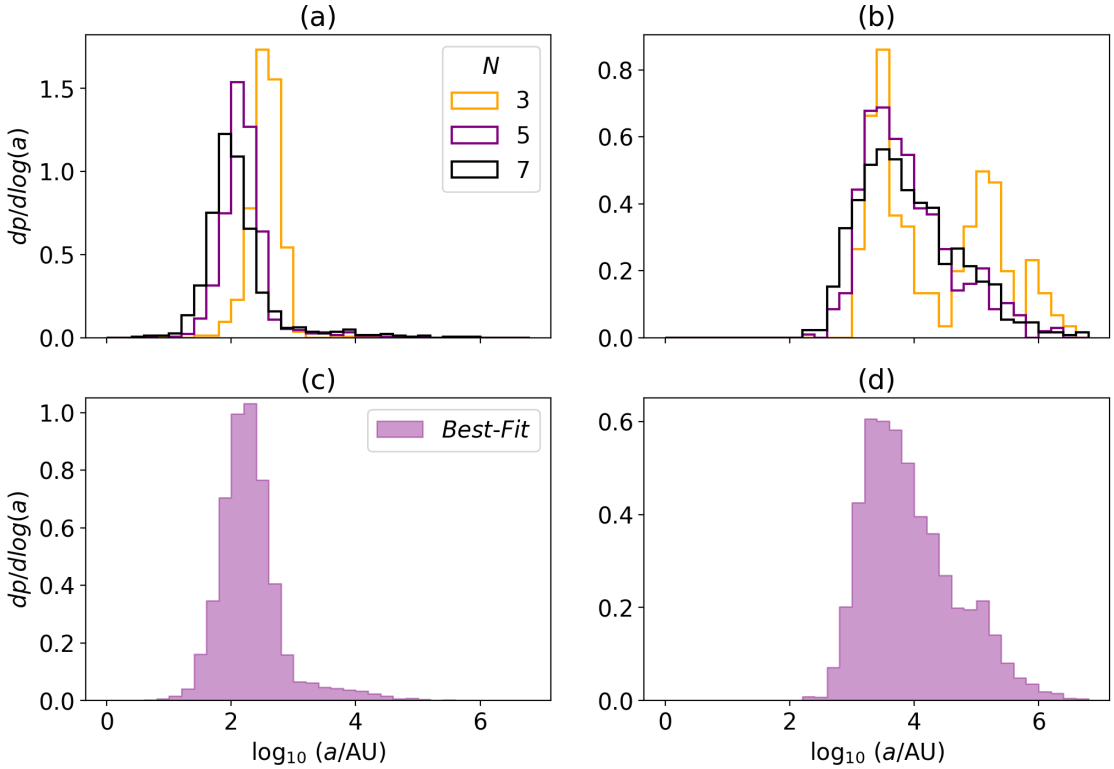

Figure 4.2. The specific probability distributions of semi-major axis, a, for (a) S2 orbits, and (b) S1 orbits, in the *Fiducial Case* with $N = 3$, 5 and 7; the results for $N = 4$ and 6 are omitted to avoid confusion. (c) and (d) show the specific probability distributions for the *Best-Fit Case*.

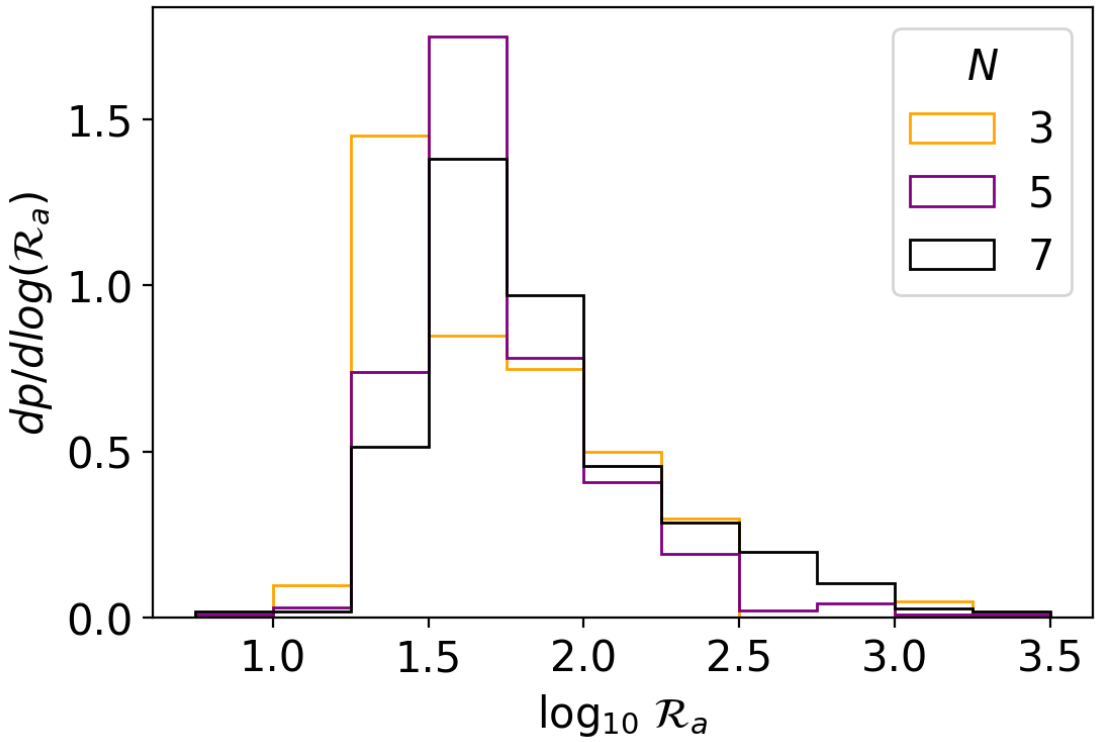

Figure 4.3. The specific probability distributions of the ratio, $\mathcal{R}_a$, of outer (S1) to inner (S2) orbital semi-major axis in triple systems for $N = 3$, 5, and 7.

independent of N. Specifically, with the scalings adopted here (see Section 2.7), the peak of the distribution of semi-major axes for S2 orbits decreases from $\sim 400\,\mathrm{AU}$ for $N=3$, to $\sim 90\,\mathrm{AU}$ for $N=7$, with the peaks of the corresponding period distributions decreasing from $\sim 8\,\mathrm{kyr}$ to $\sim 1\,\mathrm{kyr}$. In contrast, the semi-major axes for S1 orbits peak at $\sim 4,000\,\mathrm{AU}$ (periods at $\sim 300\,\mathrm{kyr}$), more or less independent of N. Because the distributions shown are specific probabilities, the area under each integrates to 1. Therefore, they capture the probability density at each semi-major axis value, but do not reflect the relative incidence of, for example, S1 vs S2 or $N = 3$ vs $N = 5$ orbits.

The ratios of S1 to S2 orbital semi-major axes, $\mathcal{R}_a$, are shown in Figure 4.3. The ratio peaks around $\mathcal{R}_a \sim 45$ for $N = 7$ and drops to $\mathcal{R}_a \sim 25$ for $N = 3$.

4.2.1.2 Semi-major axes in the Best-Fit Case

Figures 4.2c and 4.2d show that in the *Best-Fit Case*, the distribution of semi-major axes for S2 orbits peaks at $\sim 160\,\mathrm{AU}$ (periods $\sim 2.5\,\mathrm{kyr}$), similar to the *Fiducial Case* with $N=4$ or 5. For S1 orbits the distribution peaks at $\sim 4,000\,\mathrm{AU}$ (periods $\sim 300\mathrm{kyr}$), as for the *Fiducial Case* with all N.

4.2.1.3 Semi-Major axes with Very High Rotation

The distributions of semi-major axis for S2 orbits (as discussed in the two preceding subsections, 4.2.1.1 and 4.2.1.2) are, with one notable exception, almost independent of the Configuration Parameters (σ_ℓ, α_{rot}. α_{law}, α_{seg}). The one exception is the case of very rapid rotation. Figure 4.4 shows the results obtained with $\sigma_\ell = 0.3$, $\alpha_{\mathrm{rot}} = 0.99$, $\alpha_{\mathrm{law}} = \mathrm{SOL}$, $\alpha_{\mathrm{seg}} = 0$, and different N. These parameters correspond to the same range of un-segregated masses as 4.2.1.1 and 4.2.1.2, but with almost all the kinetic energy invested in solid-body rotation. In this case the semi-major axes again tend to decrease with increasing N, but the effect is significantly smaller. There are two reasons for this. First the stars start on very circular orbits, and therefore close to nested 'planetary' architectures; this reduces the frequency of close interactions. Second, with solid-body rotation, and a gravitational potential well that is only due to the masses of the other stars, the Virial Condition in the form

$$\mathcal{K} = E_{\mathrm{ran}} + E_{\mathrm{rot}} \quad = \quad -\frac{\Omega}{2}\,, \tag{4.1}$$

will often deliver setups in which some stars are unbound, from the outset, and therefore fly off immediately. At the same time, the stars on closer orbits are very strongly bound and tend to stay so. This is particularly true for $N=3$.

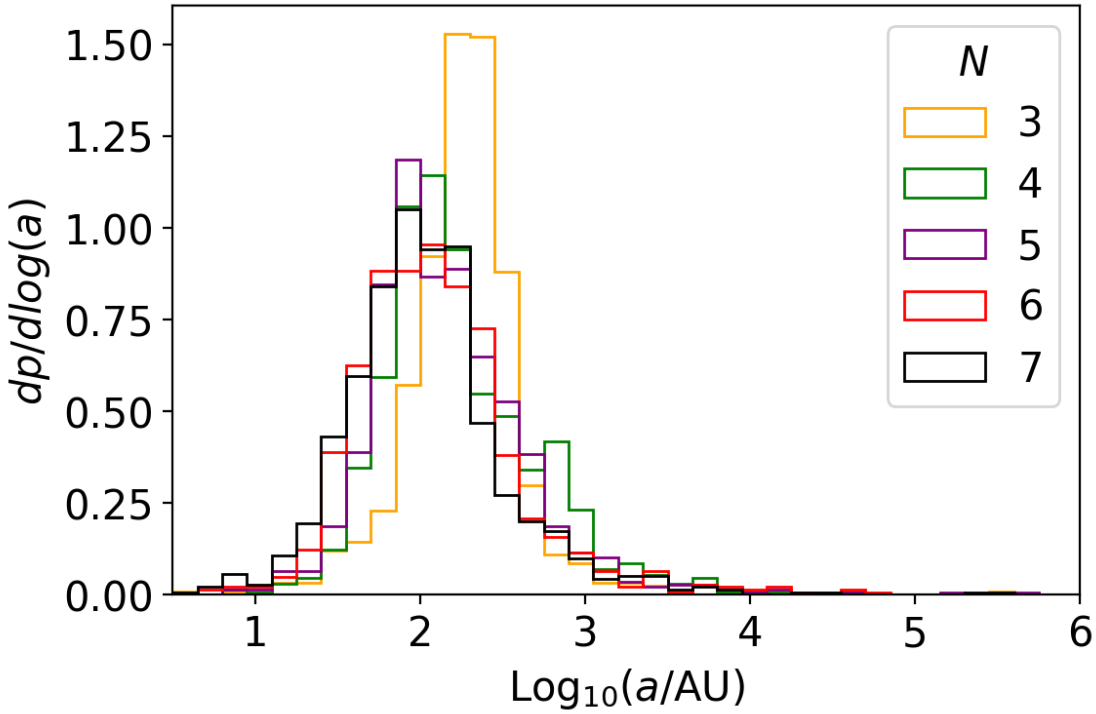

Figure 4.4. The specific probability distributions of semi-major axis, a, for S2 orbits from the high-rotation case discussed in Section 4.2.1.3 (i.e. $\alpha_{\rm rot} = 0.99$, $\alpha_{\rm law} = \textsc{sol}$, $\alpha_{\rm seg} = 0$, so almost all the kinetic energy in solid-body rotation, and no mass segregation) with $N = 3, 4, 5, 6, 7$.

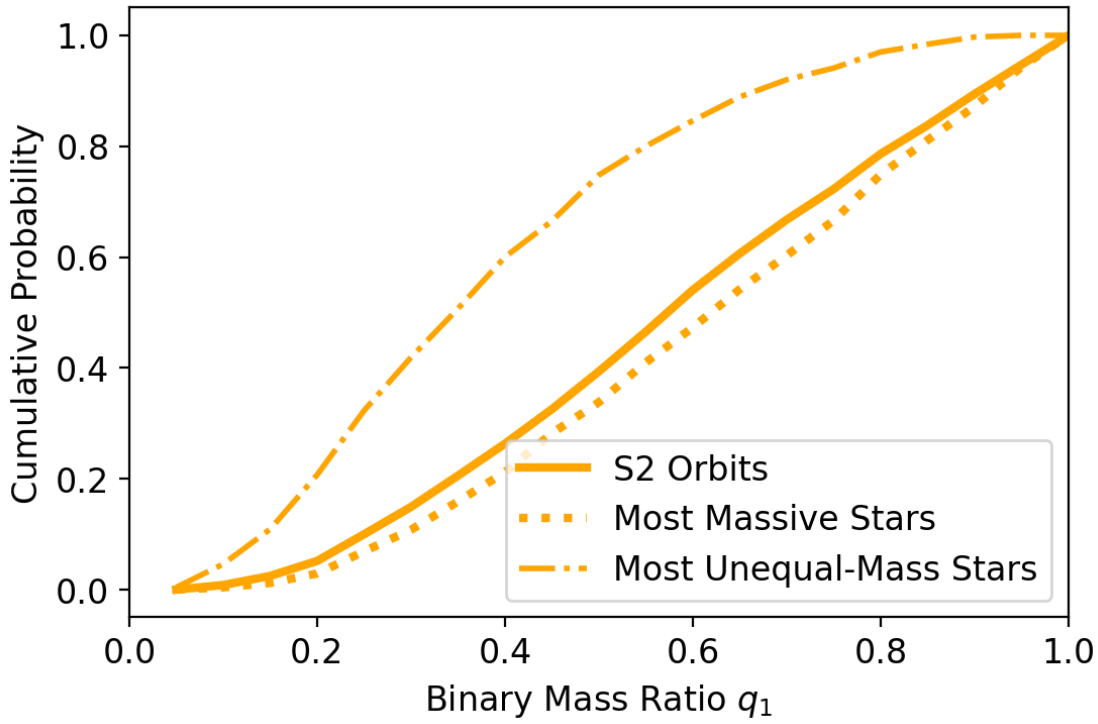

Figure 4.5. The cumulative probability distributions of mass ratio, q_1. *Solid Line*: S2 orbits of systems formed dynamically in the *Fiducial Case* with $N = 3$. *Dotted Line:* values obtained by simply pairing the 2 most massive stars. *Dash-Dotted Line:* values obtained by pairing the most and least massive stars.

4.2.2 Mass Ratios

4.2.2.1 Mass Ratios in the Fiducial Case

For any system in which two stars with masses M_1 and M_2 ($<M_1$) orbit their mutual centre of mass, the binary mass ratio is

$$q_1 = \frac{M_2}{M_1}. \tag{4.2}$$

Necessarily $0<q_1<1$.

For any system in which a star with mass M_3 and an S2 pairing (total mass M_1+M_2) orbit one another, the tertiary mass ratio is

$$q_2 = \frac{M_3}{M_1+M_2}. \tag{4.3}$$

It follows that $q_2>0$, but there is no upper limit on q_2.

The solid line on Figure 4.5 shows the cumulative probability distribution of q_1 for the S2 orbits from the *Fiducial Case* with $N=3$. The dotted line shows the ratio between the mass of the second most massive star and the mass of the most massive star, irrespective of whether they end up on an S2 orbit, for the same case. For comparison, the dash-dotted line shows the ratio between the mass of the most and least massive stars. This demonstrates the tendency of pure n-body dynamics to deliver the two most massive stars into an S2 orbit (and conversely to put less massive stars on outer orbits or eject them, as per McDonald & Clarke 1993). In this case $72(\pm1.5)\%$ of the S2 orbits involve the two most massive stars.

Figure 4.5 also shows that the distribution of mass ratios for the S2 orbits is approximately flat in the interval $0.2<q_1<1$, and that there are very few below $q_1=0.2$, i.e. to a first approximation,

$$\frac{dp}{dq_1} \sim \begin{cases} 0.00\,, & q_1<0.2\,; \\ 1.25\,, & 0.2\leq q_1<1. \end{cases} \tag{4.4}$$

Figure 4.6a shows the cumulative probability distribution of q_1 for the S2 orbits in the *Fiducial Case* with $N=3$, 4, 5, 6, 7. As N increases, the q_1 distribution for S2 orbits shifts to higher values.*

*While mass ratios and the relative frequency of high-q_1 systems increases with N, the degree of pure *Dynamical Biasing*, in which S2 orbits involve the two most massive stars, actually decreases with increasing N. This is because, with larger N, i.e. more stars in the birth subcluster and therefore more relatively massive stars to chose from, a pairing of – say – the first and third most massive star may still have a high mass ratio. As noted by SD98, *Dynamical Biasing* is a more useful concept if it is not limited in this sense, i.e. not limited to systems involving the two most massive stars.

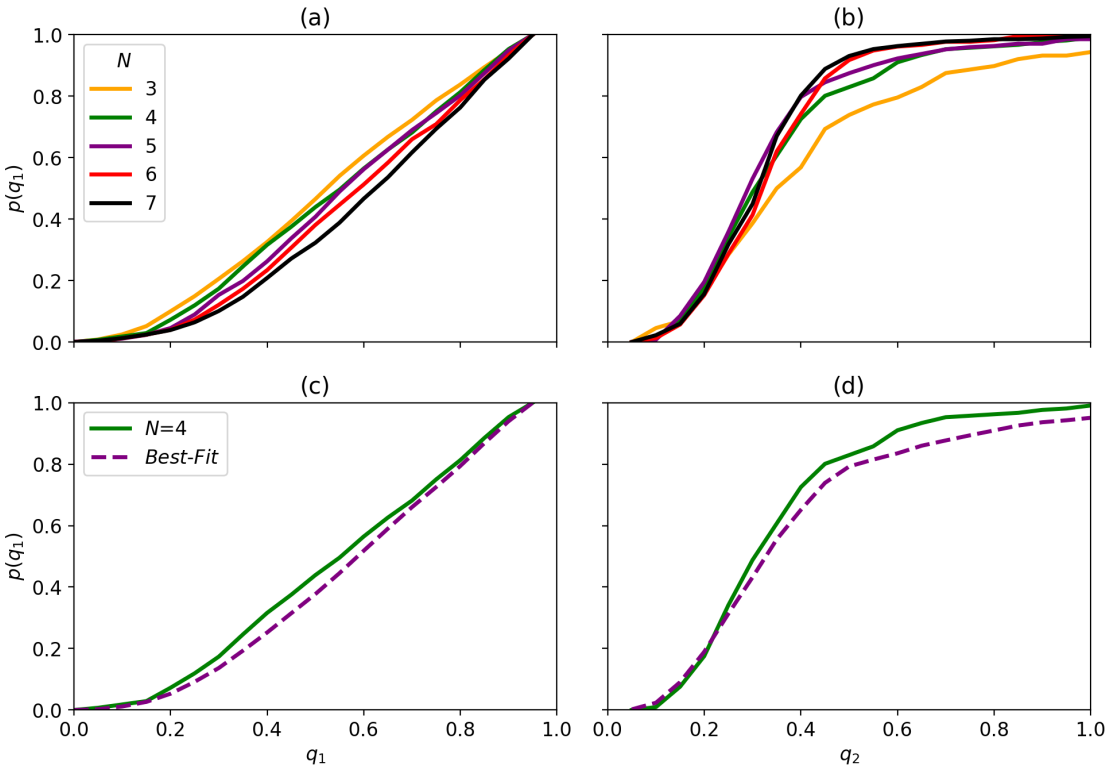

Figure 4.6. The cumulative probability distributions of binary mass ratio, q_1, and tertiary mass ratio, q_2. (a) q_1, and (b) q_2, for the *Fiducial Case* with $N = 3$, 4, 5, 6, 7. (c) q_1, and (d) q_2, for the *Best-Fit Case* with *Fiducial Case* $N = 4$ for comparison.

Our results for the *Fiducial Case* and $N=3$, 4, 5 can be compared with those of SD98, who obtain somewhat higher levels of dynamical biasing. This is because SD98 initialise their subclusters with a greater spread of stellar masses.

Our model almost never produces binaries with very similar masses, say $q_1>0.9$, since this requires two unlikely circumstances: the random selection of two stars with very similar mass from the mass spectrum, *and* for those two stars to be high-mass and therefore likely to pair up.

Figure 4.6b shows the cumulative probability distribution of q_2 for the S1 orbits in the *Fiducial Case* with $N=3$, 4, 5, 6, 7. As N increases, the mean q_2 decreases, and in the limit $N \gtrsim 5$ almost all higher-order systems have $0.1 \lesssim q_2 \lesssim 0.4$. For lower N values there is little ($N=4$) or no ($N=3$) choice for the masses of additional components in higher-order systems, once the stars in the central S2 orbit have been set.

The $N = 3$ case results in a small number of systems with $q_2 > 1$, $6(\pm2)\%$, while the $N > 3$ cases each produce less than 2% systems with $q_2 > 1$. When I compare with q_2 values reported by Reipurth & Mikkola (2015) from their $N = 3$ simulations of brown dwarf triples, I find that my 200 $t_{\rm cross}$ (~ 15 Myr) values fall between their result values, which change drastically with evolution time. Reipurth & Mikkola (2015) find $1.2(\pm0.1)\%$ of systems to have $q_2 > 1$ at 1 Myr of evolution, rising to $13(\pm2)\%$ at 100 Myr of evolution.

4.2.2.2 Mass Ratios in the Best-Fit Case

Figure 4.6c shows the cumulative probability distribution of q_1, and Figure 4.6d the cumulative probability distribution of q_2, for the *Best-Fit Case*. They are very similar to those for the *Fiducial Case* with $N=4$ and $N=5$, *i.e.* most q_1 values are between 0.2 and 0.9; most q_2 values are between 0.1 and 0.4; 65% of S2 orbits involve the two most massive stars in the initial subcluster. Rotation and mass-segregation do not have a significant influence on mass ratios.

For the *Best-Fit Case*, $4.9(\pm0.5)\%$ of systems have $q_2 > 1$. This is similar to the tertiary mass ratios observed in T21, in which $3.0(\pm0.4)\%$ of systems in the 200 pc sample have $q_2 > 1$.

4.2.3 The Number of Companions

In Chapter 3, I define the Plurality of a cohort of stars, 3.11, which is the mean number of companions that a star in the cohort has, *irrespective of whether it is a primary star*. Thus, for example, a binary involves two stars each of which has one companion, a triple involves three stars each of which has two companions, and so on.

4.2.3.1 The Number of Companions in the Fiducial Case

Figure 4.7a shows the mean Plurality, $\overline{\rm PL}$, as a function of mass for the *Fiducial Case* with $N=3$, 5, 7. As expected $\overline{\rm PL}$ increases with mass, and exceeds unity for masses above the median ($0.25\,{\rm M}_\odot$). As N increases, the mean Plurality of the highest-mass stars increases, and the mean Plurality of the lowest-mass stars decreases. This is a consequence of the greater number of interactions that can occur when N is higher. These interactions tend to eject lower-mass stars, thereby reducing their Plurality, and to deliver higher-mass stars into more tightly-bound long-lived higher-order multiples, thereby increasing their Plurality.

4.2.3.2 The Number of Companions in the Best-Fit Case

Figure 4.7b shows the variation of $\overline{\rm PL}$ with stellar mass for the *Best-Fit Case*. This is very similar to the *Fiducial Case* with $N=5$, indicating that rotation and mass segregation do not affect $\overline{\rm PL}$ very much. For masses $M \gtrsim 0.5\,{\rm M}_\odot$, $\overline{\rm PL} \simeq 1.5$.

4.2.4 Mutual Orbital Inclination and von Zeipel-Lidov-Kozai Cycles

Each orbit, o, in a multiple system has an orientation,

$$\hat{\boldsymbol{e}}_o = \frac{\boldsymbol{L}_o}{|\boldsymbol{L}_o|}, \tag{4.5}$$

which is the direction of the associated angular momentum, $\boldsymbol{L}_o$. An important parameter constraining the architectures of triple and higher-order multiples is the mutual orbital inclination, i.e. the angle

$$\theta_{oo'} = \cos^{-1}(\hat{\boldsymbol{e}}_o \cdot \hat{\boldsymbol{e}}'_o) \tag{4.6}$$

between two nested orbits o and o'. A random, isotropic distribution of orbits will have a mutual orbital inclination PDF with

$$\frac{dp}{d\theta} = \frac{\sin(\theta)}{2}, \quad 0 \leq \theta \leq \pi\ . \tag{4.7}$$

In this section I explore the statistics of mutual orbital inclinations, θ_o, and their systematic time-variation, due to von Zeipel-Lidov-Kozai cycles.

4.2.4.1 Mutual orbital inclination in the Fiducial Case

Figure 4.8a shows the specific probability distributions of mutual orbital inclinations for the *Fiducial Case* with different N. The curves in 4.8a and 4.8b represent the expected distribution of θ_o for a population of randomly oriented orbits. The random distribution peaks at $\theta_o = 90^{\rm o}$, where the solid angle per unit interval of linear angle is largest. For all N there are very few systems close to prograde coplanarity (small θ_o).

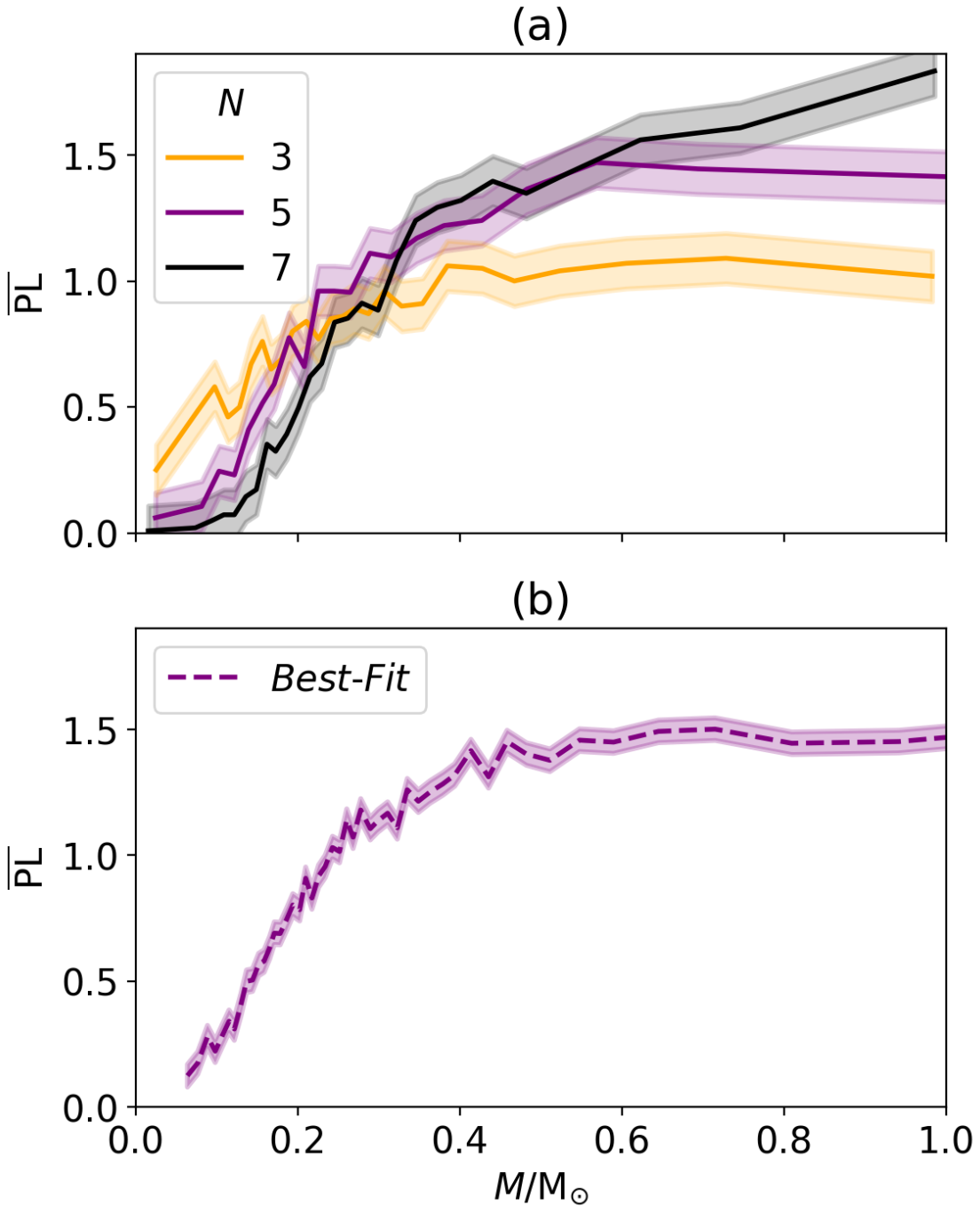

Figure 4.7. The mean plurality, $\overline{\mathrm{PL}}$, as a function of stellar mass. (a) the *Fiducial Case* with $N = 3,\ 5,\ 7$. (b) The *Best-Fit Case*. The shaded regions represent the 1σ uncertainty.

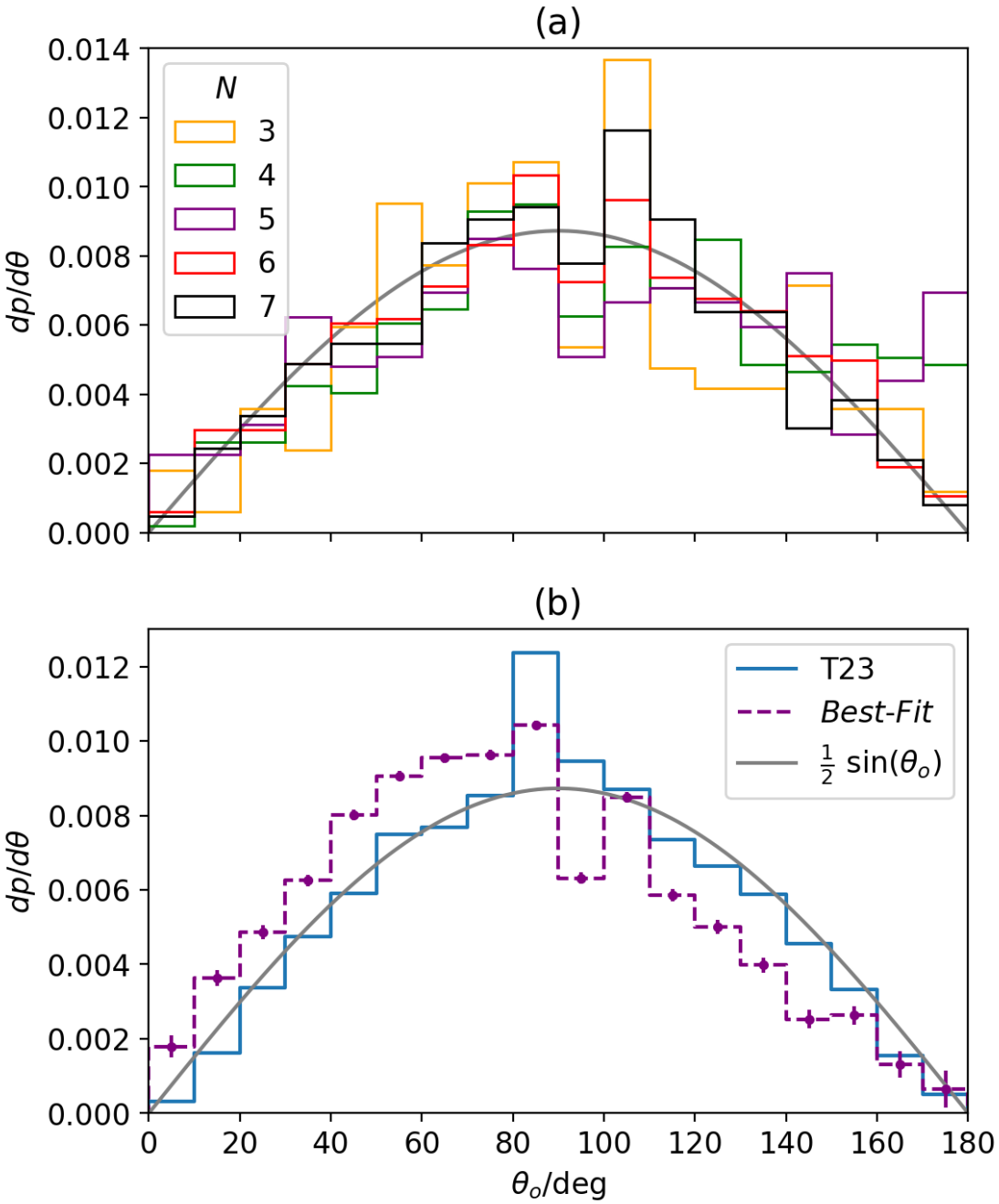

Figure 4.8. The specific probability distributions of mutual orbital inclination, θ_o, for θ_o in degrees. (a) The *Fiducial Case* with $N = 3$, 4, 5, 6, 7. (b) The *Best-Fit Case* and for the observed systems in the T23 catalogue. Figure 4.8a is produced using 2000 realizations for each N value, in order to improve signal-to-noise.

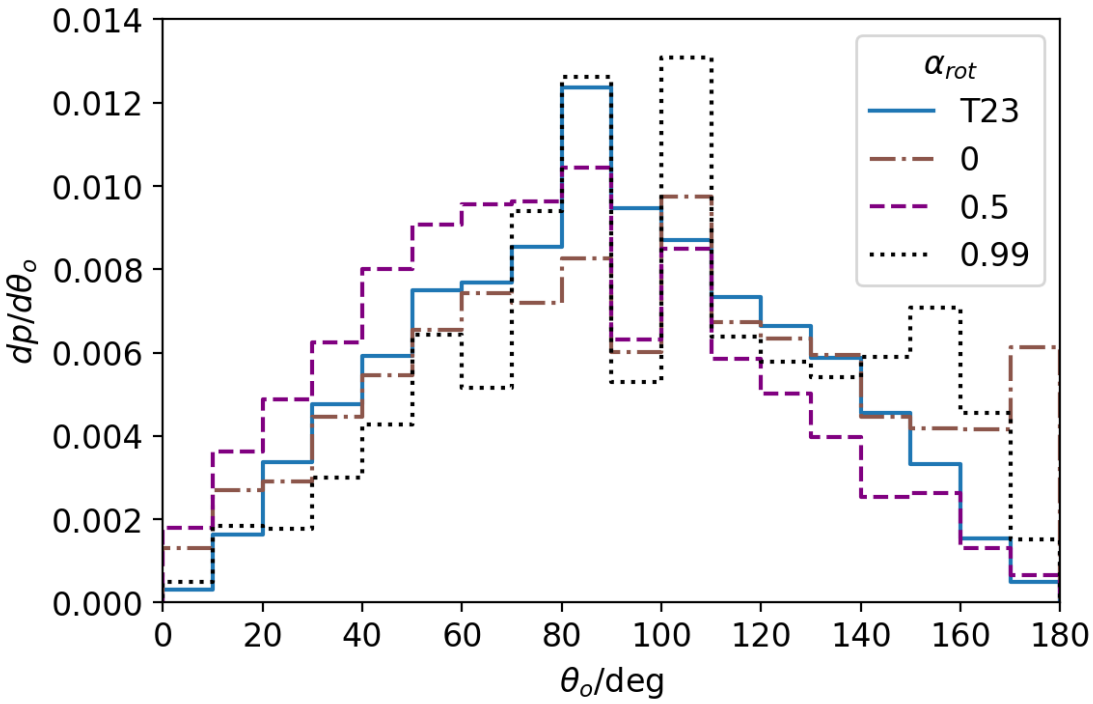

Figure 4.9. The specific probability distributions of mutual orbital inclination, θ_o, for subclusters with the *Best-Fit* N and different amounts of initial solid-body rotation, $\alpha_{\rm rot}$; and for the observed systems in the T23 catalogue. Here θ_o is given in degrees.

For $N=3$, 6, and 7, the distribution is peaked towards approximately orthogonal orbits. Two-sample Kolmogorov-Smirnov tests (K-S tests, see Massey 1951) comparing these three N distributions with one another fail to reject the null hypothesis that the samples could be drawn from the same underlying distribution. Their shape is consistent with a random θ_o distribution, as one-sample KS tests comparing these N with a random distribution also fail to reject the null hypothesis. Each of these comparisons generate p-values of p≥ 0.25.

For $N=4$ and 5, the distributions are quite flat above $\theta_o=30^{\rm o}$, implying that counter-rotating orbits are somewhat favoured compared with a random θ_o distribution. A two-sample K-S test confirms the consistency between these two distributions, failing to reject the null hypothesis (p-value$=0.27$). One-sample K-S tests also confirm that $N=4$ and 5 are inconsistent with a random distribution, rejecting the null hypothesis with p-values $\ll 0.01$. Their preference for counter-rotation is supported by the simulations of Hayashi et al. (2022), who find hierarchical triples to be more stable in an orbit that is fully retrograde than either fully prograde or orthogonal.

4.2.4.2 Mutual orbital inclination in the Best-Fit Case

Figure 4.8b shows the specific probability distributions of mutual orbital inclinations for the *Best-Fit Case* and for the observed systems in the Tokovinin 2023 catalogue (hereafter T23). They have similar shapes, but in the *Best-Fit Case* the mean is somewhat lower ($\bar{\theta}=78^\circ$ with skewness 0.038) than the T23 sample ($\bar{\theta}=89^\circ$ with skewness 0.035) and a two-sample K-S test rejects the null hypothesis with a p-value $\ll 0.01$. Further testing suggests that the *Best-Fit* parameter set has a similarly shaped underlying distribution to the observed population, but that it is uniformly lower. If the *Best-Fit* distribution is tested again with varying phase shifts, the K-S test fails to reject the null hypothesis at shifts of $+11^{\rm o}$ to $+14^{\rm o}$, where all p-values are >0.10.

There is a dip in orbits with $\theta_o\sim 90^\circ$. It is supported by the Hayashi et al. (2022) results, which find initially-orthogonal orbits to be the least stable when compared with fully prograde and fully retrograde.

4.2.4.3 The Effect of Rotation

Figure 4.9 shows the specific probability distributions of mutual orbital inclinations for the systems in the T23 catalogue, and the effect of introducing different amounts of ordered rotation, $\alpha_{\rm rot}$, into the *Best-Fit Case*. There is a good fit in the shape of the distribution when $\alpha_{\rm rot}=0.5$ though this distribution is shifted from the observed values as discussed in the preceding section (Sec. 4.2.4.2).

Very low rotation ($\alpha_{\rm rot}=0$) and very high rotation ($\alpha_{\rm rot}=0.99$), on the other hand, produce distributions which are distinct from the observed and $\alpha_{\rm rot}=0.5$ distributions and flatten toward high inclinations ($\theta_o>110^\circ$). Two-sample K-S tests reject the null

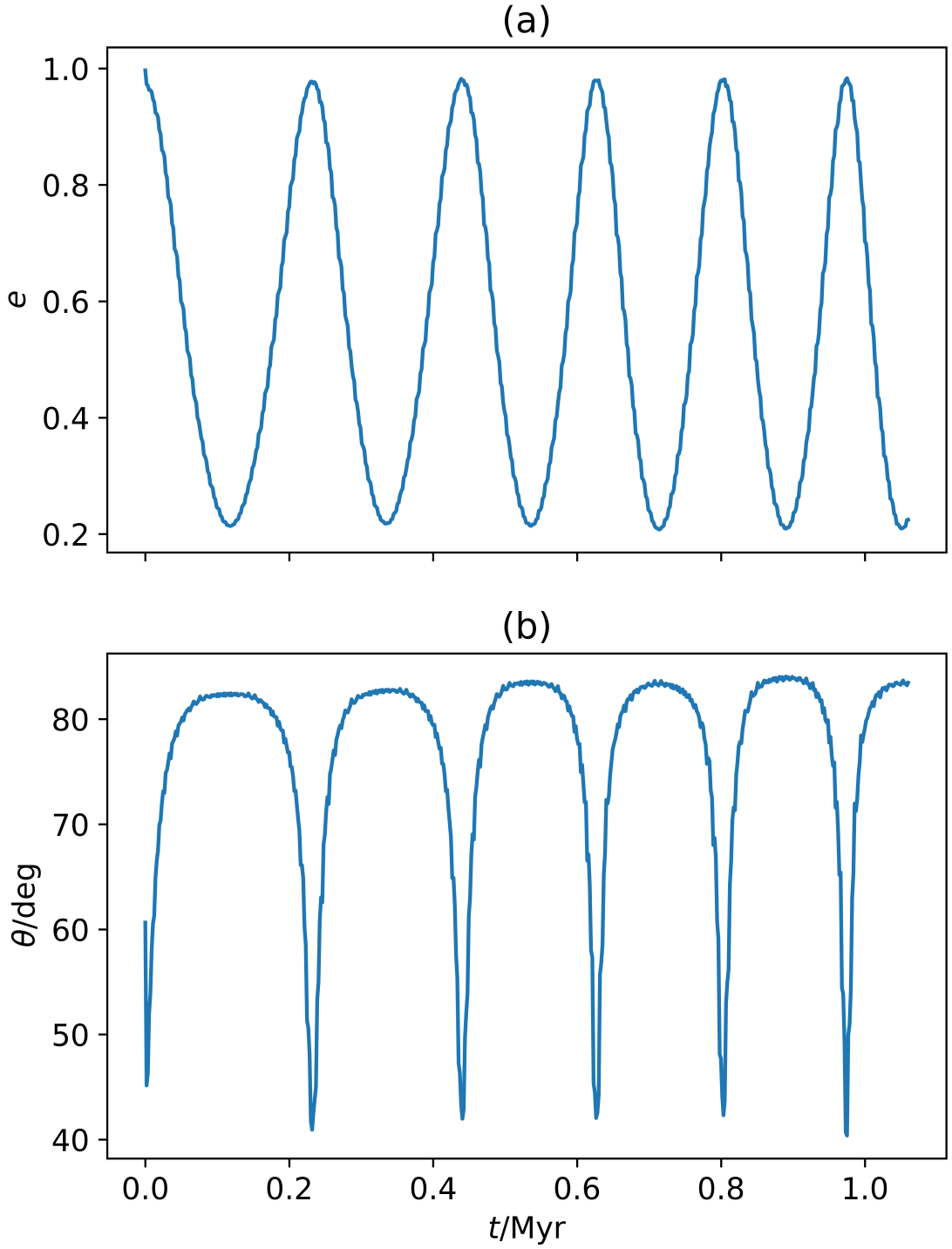

Figure 4.10. An hierarchical triple system undergoing von Zeipel-Lidov-Kozai cycles. (a) The eccentricity, e, of the inner S2 orbit, as a function of time. (b) The corresponding mutual orbital inclination, θ_o.

hypothesis with p-values < 0.2 for all pairings except $\alpha_{\rm rot} = 0$ and $\alpha_{\rm rot} = 0.99$, which produce a p-value of 0.11.

None of the distributions are consistent with a random sample – one-sample K-S tests between $\alpha_{\rm rot} = 0, 0.5, 0.99$ and a random θ distribution all reject the null hypothesis with p-values < 0.5.

4.2.4.4 von Zeipel-Lidov-Kozai Cycles

In a von Zeipel-Lidov-Kozai (ZLK) cycle, a slow periodic change in the eccentricity of the inner binary produces a correlated change in the inclination of the tertiary orbit at each peri-centre. An example from our numerical experiments is shown in Figure 4.10. In the case of hierarchical triples with high eccentricity outer orbits, octupole-order interactions can drive the eccentric Kozai-Lidov (EKL) mechanism (see Naoz 2016), potentially flipping the orbit from $\theta_o < 90^\circ$ to $\theta_o > 90^\circ$. However, of the systems which achieve $\theta_o > 90^\circ$ in the experiments reported here, only $\sim 25\%$ appear to reach these inclinations due to the EKL mechanism. The remainder are either formed with, or displaced impulsively into, orbits with $\theta_o > 90^\circ$.

4.2.5 Orbital Eccentricities

Figure 4.11a shows the specific probability distributions of eccentricity, e, for S2 orbits in the *Fiducial Case* with $N = 3$, 4, 5, 6, 7. Figure 4.11c shows the distribution of e for S2 orbits in the *Best-Fit Case*. In all cases, the distribution of eccentricities is very close to thermal, i.e. $dp/de \simeq 2e$. The only significant departure from a thermal distribution is an excess of very eccentric orbits ($e \simeq 1$), which is evident for all cases except the *Fiducial Case* with $N = 3$.

The high-e excess in S2 orbits increases with N. Some of this high-e excess may be due to stellar exchanges between nested S2 and S1 orbits, or to tertiary members exciting S2 orbits into higher eccentricities via ZLK cycles. The tertiary may then either remain bound to the excited S2 system, or be ejected. The increase in the high-e excess with increasing N supports these hypotheses, as the opportunities for orbital exchanges, and the number of systems capable of ZLK cycles, both increase with N.

Figures 4.11b and 4.11d show the specific probability distributions of e for S1 orbits for, respectively, the *Fiducial Case* with $N = 3$, 4, 5, 6, 7, and the *Best-Fit Case*. Again the distributions are approximately thermal, albeit with low counts for the low-N cases, and again there is an excess of high eccentricity orbits ($e > 0.95$). The high-e S1 population is likely to be entirely meta-stable (see Sections 3.3.4.1 and 4.3.7). It is also likely to be sensitive to external perturbations and challenging to observe; further discussion of this issue is found in Section 4.3.8.

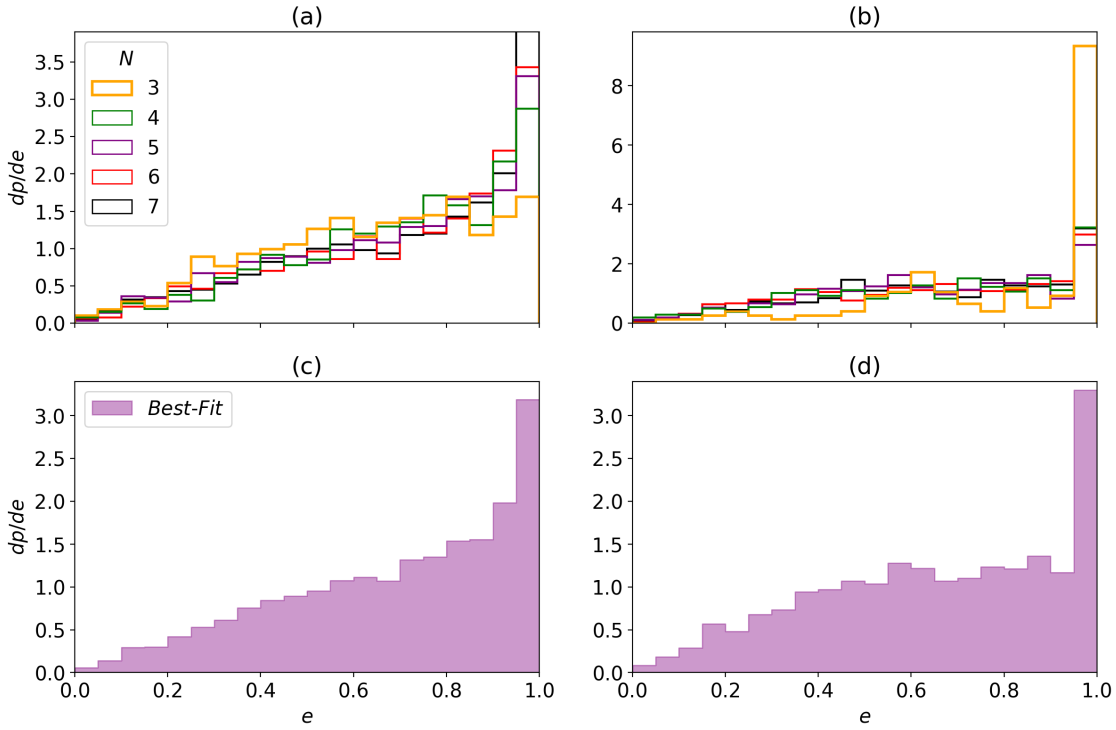

Figure 4.11. The specific probability distributions of eccentricity, e. (a) S2 orbits, (b) S1 orbits, for the *Fiducial Case* with $N = 3, 4, 5, 6, 7$. (c) S2 orbits, (d) S1 orbits, for the *Best-Fit Case*.

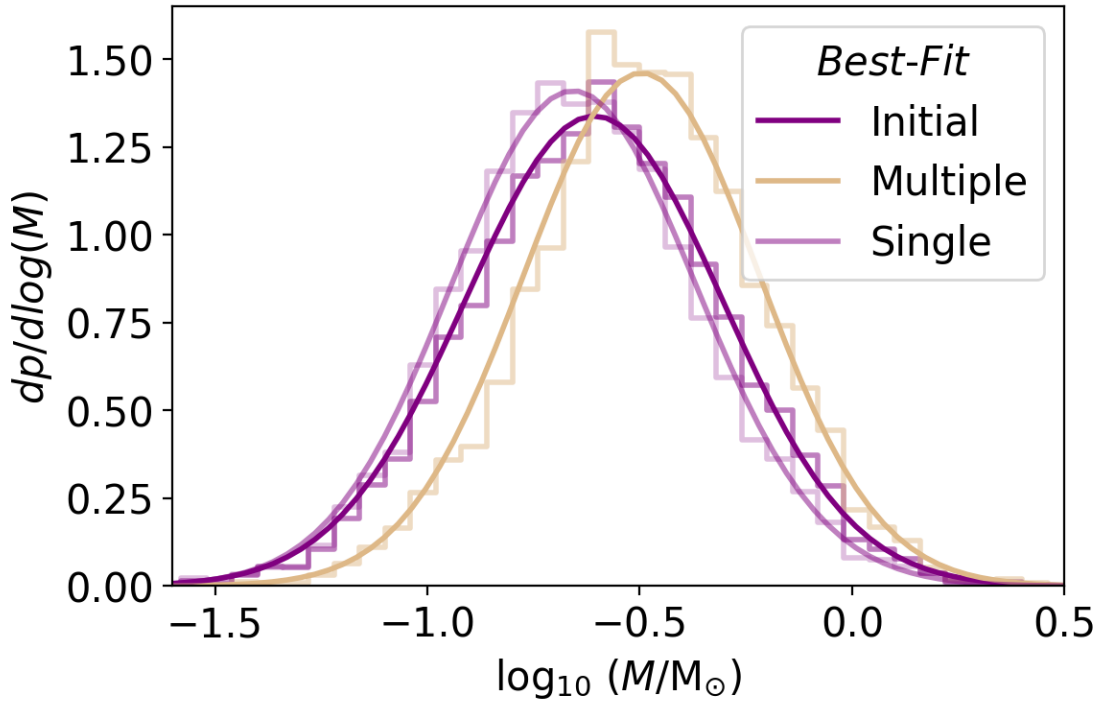

Figure 4.12. The mass distributions for all stars, for those that end up in multiples, and for those that end up single, in the *Best-Fit Case*. Means and standard deviations are given in Table 4.2.

Table 4.2. The mean and standard deviation of log-normal fits to the mass distributions for stars that end up in multiple systems and stars that end up single. Values are given for different N in the *Fiducial Case* and for the *Best-Fit* N-distribution. $\ell = \log_{10}(M/M_\odot)$.

Fiducial						*Best-Fit*
with $N =$	3	4	5	6	7	
INITIAL						
μ_ℓ	-0.60	-0.60	-0.60	-0.60	-0.60	-0.60
σ_ℓ	0.30	0.30	0.30	0.30	0.30	0.30
MULTIPLE						
μ_ℓ	-0.52	-0.50	-0.48	-0.44	-0.46	-0.49
σ_ℓ	0.28	0.28	0.27	0.28	0.28	0.27
SINGLE						
μ_ℓ	-0.71	-0.68	-0.65	-0.62	-0.59	-0.66
σ_ℓ	0.27	0.28	0.28	0.29	0.31	0.28

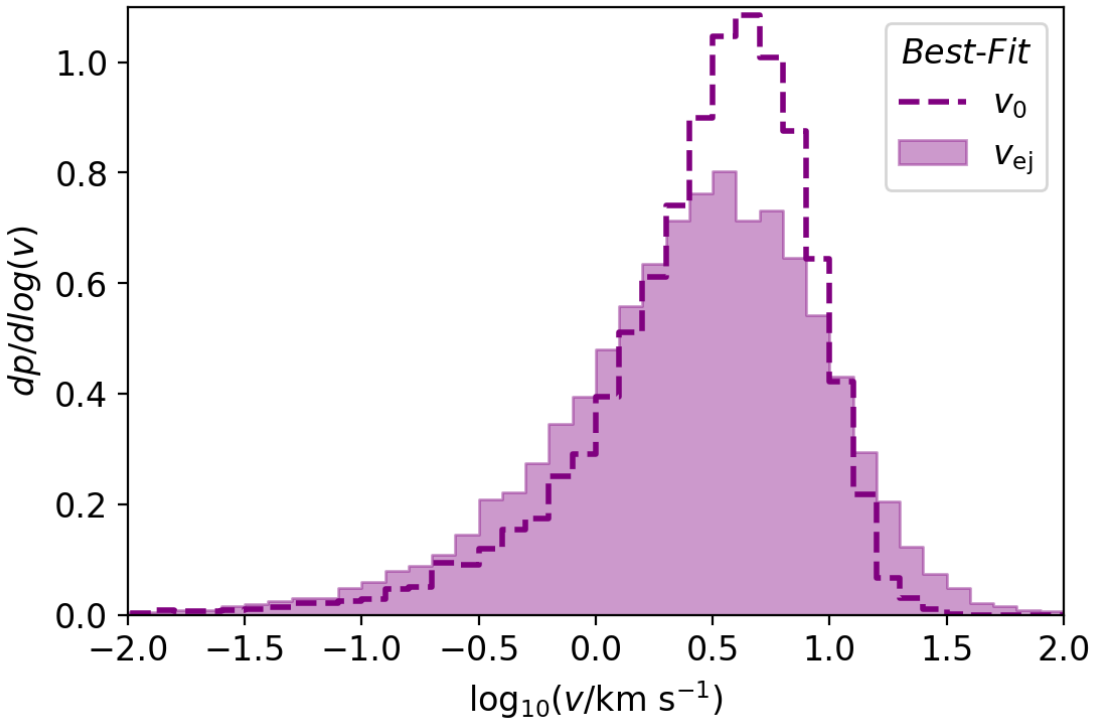

Figure 4.13. The specific probability distributions of initial velocity (v_0) and ejection velocity ($v_{\rm ej}$) for all stars in the *Best-Fit Case*.

4.2.6 Dynamical Biasing

Table 4.2 gives the means and standard deviations of log-normal fits to the mass distributions for all stars, for stars that end up in multiples, and for stars that end up single, in the *Fiducial Case* with $N = 3$, 4, 5, 6, 7, and in the *Best-Fit Case*. Due to *Dynamical Biasing* (McDonald & Clarke, 1993), the stars in multiple systems are in all cases on average more massive than the singles, typically by $\sim 50\%$. Figure 4.12 illustrates this for the *Best-Fit Case*; the distributions for the Fiducial cases look very similar.

4.2.7 Ejection Velocities

All stars start off as members of virialised subclusters. Therefore at the end any single star must have been ejected fast enough to become unbound from all the other stars in its birth subcluster.

Fig 4.13 compares the Maxwellian distribution of initial stellar velocities, v_0, with the velocities of single stars at the end, $v_{\rm ej}$, for the *Best-Fit Case*. The ejection velocity distribution is slightly broadened compared with the initial velocities. While few stars have velocity outside of the initial velocity range, the fraction of stars with velocities greater than three times the peak in the initial distribution increases significantly, by a factor of ~ 4 compared with the initial distribution. A similar result is found for the *Fiducial Case*.

4.2.8 Dissolution Timescale

Figure 4.14a shows the cumulative probability distribution of single-star ejections as a function of time, for the *Fiducial Case* with $N = 3$, 4, 5, 6, 7. Ejections occur more rapidly for larger N, as shown by Hamers (2020), but even for $N = 3$, 50% of ejections occur within the first 66 crossing times.

Figure 4.14b shows the cumulative probability distribution of single-star ejections as a function of time, for the *Best-Fit Case*. $87(\pm 5)\%$ of ejections occur in the first 2 Myr, and $98(\pm 2)\%$ occur by 10 Myr.

4.2.9 Number of Multiples per Subcluster

In most cases, a subcluster in the experiment dissolves into one multiple system of multiplicity m, and $N - m$ single stars. But in some instances the subcluster dissolves into as many as $\lfloor N/2 \rfloor$ multiple systems. For the *Best-Fit Case*, $21(\pm 1)\%$ of subclusters produce more than one multiple system. All additional multiple systems produced in this case are binaries.

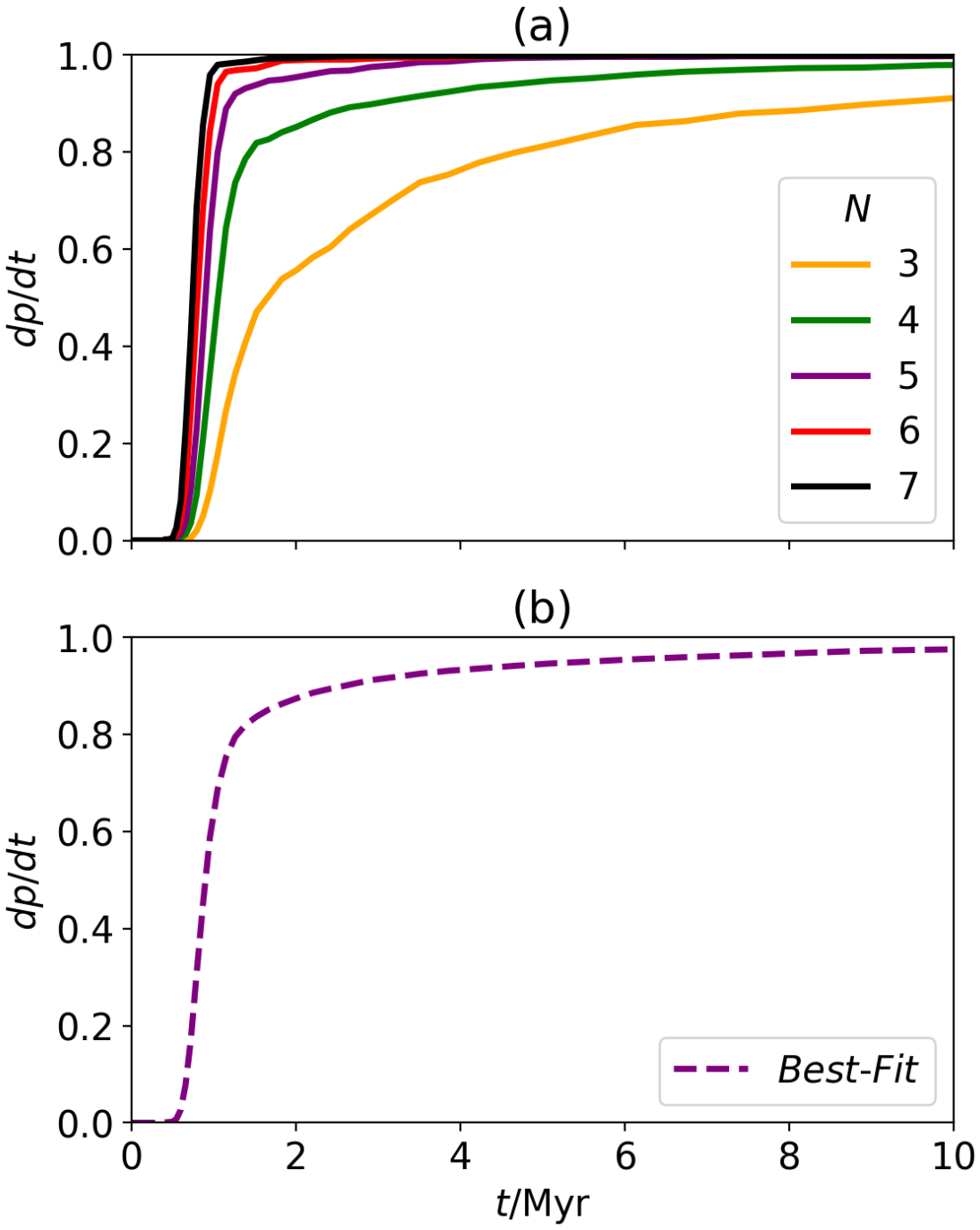

Figure 4.14. The cumulative probability distributions of the first ejection as a function of the elapsed time. (a) The *Fiducial Case* with $N = 3,\ 4,\ 5,\ 6,\ 7$. (b) The *Best-Fit Case*.

4.3 Discussion

In this section I discuss some of the caveats and limitations that pertain to the results presented above.

4.3.1 Dynamical Biasing and Ejections

If, as I find in Chapter 3, a prestellar core typically produces $N=4$ or 5 stars, and these stars have a relatively small range of masses ($\sigma_\ell \sim 0.3$), the concept of *Dynamical Biasing* is slightly more nuanced, in the sense that even if an S2 orbit does not involve the two *most* massive stars in the subcluster, it will still – more often than not – involve two of the *more* massive stars.

This in turn means that the single stars that are ejected will tend to be of lower mass, and therefore harder to detect in observations than the ones that end up in multiple systems.

4.3.2 The Core Potential and Subcluster Dispersal

It is reasonable that I have only taken account of the gravitational field of the stars in the subcluster. The gas between the stars in the subcluster will only dominate the gravitational field in the region where the stellar dynamics is modelled ($R < R_{\rm o}$) if its mean density is very high,

$$\bar{n}_{\rm H_2} \gtrsim 2 \times 10^9 \, {\rm cm}^{-3} \left(\frac{N}{5}\right) \left(\frac{\bar{M}}{0.25 \, {\rm M}_\odot}\right) \left(\frac{R_{\rm o}}{500 \, {\rm AU}}\right)^{-3}. \tag{4.8}$$

This is unlikely. However, residual gas from the prestellar core at radii larger than $R_{\rm o}$ will slow down dispersal of the stars formed, unless it has been very widely dispersed. Therefore the ejection velocities computed should strictly be seen as upper limits.

4.3.3 Binary Twins

A significant fraction of observed binary stars have mass ratio close to unity. In other words the component stars have very similar masses. This preference is too extreme to be the result of dynamical biasing, and is normally attributed to hydrodynamical effects, which are not captured in the pure N-body numerical experiments reported here. The standard explanation (Whitworth et al., 1995, their Section 5.2) is that a binary forms, possibly by disc fragmentation, but there is then ongoing accretion onto the binary. The specific angular momentum of the inflowing material increases with time, and therefore the lower-mass component, which has higher specific angular momentum (by a factor $q_{_1}^{-2}$) and is therefore on a wider orbit, is better able to accrete this material. Consequently it grows towards the same mass as the higher-mass component.

4.3.4 Disc Fragmentation and Primordial Multiples

The stars in our numerical experiments start with random positions and velocities. Therefore primordial binaries in close, tight orbits will be extremely rare at the outset. However, in nature stars forming by dynamical fragmentation of a prestellar core will be attended by circumstellar accretion discs, and these discs may become sufficiently massive and cold to fragment, producing close companions (semi-major axes $a \lesssim 50\,\mathrm{AU}$) on low-eccentricity orbits. Indeed, I believe that disc fragmentation is a critical channel for producing close systems (e.g. Whitworth & Stamatellos, 2006). Kuruwita & Haugbølle (2023) have also shown that the gas present around forming stars can trigger their inspiral and create close binaries. These close systems would be more difficult to disrupt, increasing the proportion of higher-order multiples. Therefore the experiments reported here are not expected to reproduce the statistics of the closest observed orbits.

Primordial binary systems would alter the orbital and mass ratio statistics of stellar populations. They are often very close, decreasing the average semi-major axis, and as they are more likely to be equal-mass pairs (as discussed in Section 4.3.3), they would shift the binary mass ratio. So the inclusion of these systems in the experiment would likely decrease the binary semi-major axis and shift the binary mass ratio distribution closer to unity.

For primordial binaries formed through disc fragmentation, their location within the system hierarchy would affect the outer mass ratios of the systems. If we consider the mass ratios of the binary population produced by the experiment as an example (Figure 4.6a and c) and split the more massive star into two equal mass bodies, the existing binary mass ratio becomes the new tertiary mass ratio. Therefore the shape of the q_2 distribution is significantly altered and no $q_2 > 1$ systems are present. But if we instead split the less massive star of the binary into equal masses, all binaries will now become triples with $q_2 > 1$. The ratio with which disc fragmentation acts on higher- vs lower-mass members of forming stellar subclusters will affect this $q_2 > 1$ value and the outer mass ratios as a whole. If implemented in the experiment, the effect of close primordial binaries formed through disc fragmentation on the tertiary mass ratio would depend highly upon the prescription for ordering and placing these binaries within the initial subclusters.

4.3.5 Interacting Discs and Tidal Circularisation

An attendant circumstellar accretion disc may also interact with another star and its disc. This will dissipate kinetic energy, and may thereby make the two stars bound, or more tightly bound if they are already bound (e.g. McDonald & Clarke, 1995). This mechanism is missing from our pure N-body experiments, and would help to produce closer orbits.

In addition, stars on extremely close orbits ($a \lesssim 0.1\,\mathrm{AU}$) will experience strong internal tidal interactions, and this will drive them into low-eccentricity orbits. However, such close orbits are not produced here – and tidal interactions would not be captured, even if they were, since the stars here are point masses.

Binary orbits may also be circularised when the component stars accrete from a circumbinary disc. Again this is not included in our numerical experiments.

4.3.6 Time-scales

The *Orbital Statistics* presented in this paper represent subclusters that have been evolved for 1000 crossing times. With the scalings I have adopted, one crossing time is $\sim 0.077\,\mathrm{Myr}\,N^{-1/2}$, which for the *Best-Fit Case* with $\mu_N = 4.8$ gives $\sim 0.035\,\mathrm{Myr}$. *Orbital Statistics* are only considered robust if they are reproduced in two successive MMOs (see Section 2.3). Thus the first *Orbital Statistics* are collated after 66 crossing times, i.e. at $\sim 2\,\mathrm{Myr}$.

For the *Fiducial Cases* with large $N \geq 4$, and for the *Best-Fit Case*, Figure 4.14 indicates that the *Orbital Statistics* are closing in on their asymptotic values by $t \lesssim 3\,\mathrm{Myr}$, whereas for $N = 3$, the *Orbital Statistics* only approach their asymptotic values at $t \gtrsim 15\,\mathrm{Myr}$. This may constitute a new and – at least in principle – distinctive constraint on the size of the region in which the protostellar fragments in a core become an ensemble of virialised protostars, like the ones I have modelled. If I exploit the fact that the experiments are scale-free, i.e. I can adjust the mass- and length-scales as described in Section 2.7, then the radius is given by

$$R_{\mathrm{o}} \geq \qquad 250\,\mathrm{AU}\,\left(\frac{N}{5}\right)^{2/3}\left(\frac{\bar{M}}{0.25\,\mathrm{M}_{\odot}}\right)^{1/3}\left(\frac{t_{\mathrm{disp}}}{\mathrm{Myr}}\right)^{2/3}, \qquad N > 3 \qquad (4.9)$$

$$R_{\mathrm{o}} \leq \qquad 60\,\mathrm{AU}\,\left(\frac{N}{5}\right)^{2/3}\left(\frac{\bar{M}}{0.25\,\mathrm{M}_{\odot}}\right)^{1/3}\left(\frac{t_{\mathrm{disp}}}{\mathrm{Myr}}\right)^{2/3}, \qquad N = 3 \qquad (4.10)$$

where N is the number of stars in the subcluster, $\bar{M}$ is the mean stellar mass, and t_{disp} is the timescale on which the subcluster disperses.

4.3.7 Eccentricity and meta-stable orbits

Section 4.2.5 reports a population of tertiary orbits with very high eccentricity, which is most significant in $N = 3$ subclusters. All $N = 3$ systems which have S1 orbits are triples that have not undergone an ejection. Consequently, they are either stable from the outset, or meta-stable at the end of the experiment (see subsection 3.3.4.1). Simulations by Hayashi et al. (2022) show that the disruption timescale of unstable triple systems can be as long as 10^9 times the orbital period of the inner pair and is highly

sensitive to the orbital parameters of the system. The ejection process can therefore take much longer than the standard run time of the experiment, especially in the case of high-eccentricity S1 orbits, which can have very long orbital periods.

Mardling & Aarseth (2001) established a semi-empirical and widely used metric for determining the stability of hierarchical triple systems based upon their orbital parameters. I find that of the *Fiducial* $N = 3$ systems which are triples at the end of the experiment, $15(\pm4)\%$ meet the Mardling & Aarseth (2001) stability criterion. None of these stable systems are in the high-e ($e \geq 0.95$) regime. This suggests that $\sim 10 - 20\%$ of the *Fiducial* $N = 3$ triples were likely born into and will remain in hierarchical, long-term stable triples, while the remainder are likely meta-stable and will eventually disrupt.

I expect a similar trend of meta-stability in all subclusters which have not experienced an ejection (such as $N = 4$ quadruples), especially within the high-e S1 regime. I note that because destabilization can take many Gyr, these stars may contribute to the multiplicity of their systems for a significant portion of member lifetimes.

4.3.8 External Perturbations

Even before a subcluster disperses due to internal interactions, it may be subject to external perturbations, due to other massive structures in the vicinity, i.e. other subclusters and gas clumps. These perturbations will sometimes unbind the outer members of the subcluster and will destroy some of the multiples.

Once the subcluster disperses, its stars and multiple systems will interact with other stars and multiple systems formed in nearby subclusters. These interactions will change the architectures of existing multiples, and lead to exchanges of stars between the multiples from different subclusters. In the long term these processes will tend to reduce the overall multiplicity and plurality, by unbinding wider orbits, but at the same time it will harden closer orbits.

The high-eccentricity tertiary orbits noted in Section 4.2.5 and 4.3.7 (see Figure 4.11) are real in the sense that their orbital parameters are confirmed at successive MMOs. However, successive MMOs are only $\sim 1\,\mathrm{Myr}$ apart, and these highly eccentric orbits have periods $\sim 1\,\mathrm{Gyr}$. Consequently they will be hard to detect observationally, firstly because they will spend most of their lifetime at distances $\gtrsim 1\,\mathrm{pc}$, and secondly because association with a companion will be hard to establish. Therefore they are unlikely to appear in catalogues. More importantly, they have very low binding energy and will be easily disrupted. I find that performing a cut to remove these high-period orbits ($P < 10^7$ yr, $a \lesssim 4.5 * 10^4$ AU) does not affect the distributions of tertiary mass ratio or mutual orbital inclination at a statistically significant level.

4.3.9 Collisions and Mergers

Since the stellar particles are treated as point masses, collisions and mergers between particles are not included in these experiments. Because the subclusters studied here are small ($N \leq 7$) with relatively low number density, random chance collisions are extremely unlikely. Situations which might lead to mergers are also rare. Only $\sim 0.1\%$ of multiple systems formed in the experiments reported here have semi-major axes $a < 1$ AU. While some of these systems have the potential to merge due to tidal dissipation, thereby reducing the proportion of close systems, the effect on the overall statistics is very small.

4.3.10 Initial Spatial Distribution

I invoke a uniform density profile when positioning the stellar particles. Because the number density of particles in each subcluster is so low, the choice of density profile has little effect on the initial distributions.

Our initially rotating subclusters may begin with either a spherical or oblate geometry (see Sec. 2.1.2 and 2.1.4, respectively). I find that these geometries do not produce statistically significant differences in any of the reported metrics.

4.4 Summary

The initial conditions of a subcluster play an integral role in determining the characteristics of the stellar multiple systems that it spawns. The initial number of stars in the subcluster, N, has the greatest effect, influencing periods and separations, dynamical biasing, plurality, mutual orbital inclinations, and ejection timescales. The fraction of kinetic energy in ordered rotation, $\alpha_{\rm rot}$, and the degree of mass segregation, $\alpha_{\rm seg}$ also have an effect on some of these statistics.

The distributions of semi-major axis, a, for S2 orbits shift to lower values with increasing N. This is because S2 orbits are hardened by energy exchange with other stars in the subcluster, often leading to the ejection of these other stars. With higher N there are more 'other stars' with which to exchange energy.

In contrast the distributions of a for S1 orbits are essentially independent of N.

In the *Fiducial Case* the percentage of subclusters that produce an S2 orbit involving the two most massive stars decreases from $72(\pm1.5)\%$ for $N=3$, to $62(\pm1.6)\%$ for $N=7$. However, there is still *Dynamical Biasing*, i.e. the tendency for more massive stars to be bound in multiples and lower-mass stars to be ejected, when N is large. This is because, when N is large, stars other than the two most massive ones may still be quite massive.

Consequently the single stars tend to have lower than average mass, and to acquire the highest velocities, $v_{\rm ej}$, relative to the centre of mass of the original subcluster. The distribution of $v_{\rm ej}$ for these single stars is indistinguishable from the Maxwellian distribution

of velocities in the initial subcluster, so they should be classified as 'walk-aways', rather than 'run-aways'. Walk-aways are ejected earlier in subclusters with higher N.

S2 orbits have a flat distribution of mass ratios between $q_1 = 0.2$ and $q_1 = 1.0$. S1 orbits have a flat distribution of mass ratios between $q_2 = 0.1$ and $q_2 = 0.5$ with very few higher values. These distributions do not depend strongly on the initial conditions of the subcluster.

On average, a star's Plurality (i.e. the number of companions that a star has, irrespective of whether it is a primary) increases with its mass. The maximum number of companions increases with N, and with the scaling adopted here, almost all stars with $M \gtrsim 0.5 \mathrm{M}_\odot$ end up with at least one companion when $N \geq 3$.

Moderate rotation results in triple systems with a distribution of mutual orbital inclinations peaking at $\theta_o \sim 90°$, in agreement with the observed distributions. For triple systems with $\theta_o > 90°$, the majority ($\sim 75\%$) form dynamically in high-inclination orbits without the help of vZKL cycles.

For the *Best-Fit Case*, $21(\pm 1)\%$ of subclusters produce more than one multiple system.

When considering *Multiplicity Statistics*, i.e. the relative proportions of different multiples (singles, binaries, triples, etc.) Chapter 3 found that subclusters should have a distribution of N values with median $\mu_N \simeq 4.8$; the kinetic energy of the stars should be divided between random isotropic velocities drawn from a Maxwellian distribution and ordered rotation, with comparable amounts in each; and there should be mass segregation. Here I have shown that these properties are also compatible with the observed *Orbital Statistics*, i.e. the distributions of semi-major axis, mass ratio, and eccentricity. The *Best-Fit* properties produce a similarly shaped mutual orbital inclination distribution as observations, but with a negative phase offset of $11 - 14$ degrees.

I have shown that there is a relationship (Equation 4.9) between the size of the region in which the protostars in a subcluster initially condense out (R_o), the number of stars in the subcluster (N), the mean stellar mass ($\bar{M}$), and the timescale (t_disp) on which the subcluster disperses.

Chapter 5

Equation for End States of an *N*-Star Subcluster

In this chapter, I derive multiple forms of a function for enumerating end states of an N-star subcluster. The equations provide both the number and multiplicity of systems. I detail connections to an existing function in number theory, and discuss uses for the restricted forms of the equation presented here.

5.1 Introduction

An early goal of this work was to calculate the multiplicity statistics that resulted from the evolution of 3- 4- and 5-star stellar subclusters. For this purpose, the MMO needed to be capable of identifying and tracking every type of system which could arise. This is managable for small N – an isolated and initially-bound subcluster of 2 stars will always remain as a binary; such a subcluster with 3 stars can form a triple, or decay into a binary and a single. The possible outcomes increase quickly – 4 stars may remain a quadruple, decay into a triple and a single, become two binaries, or become a binary and three single stars. As N increases, keeping track of these possible end states presents a complex combinatorics problem.

In order to better understand how the number of outcomes, $\mathcal{A}_{_N}$, increases with N, I sought to derive an equation for $\mathcal{A}_{_N}$.

Table 5.1. General Variables and Functions

number of different end-states for a subcluster of N stars	$\mathcal{A}_{_N}$
Heaviside Function	$\mathcal{H}$
dummy ID of star	n, n', n''
Partition Function	$\textsc{par}(N)$

5.2 An intuitive, limited form

An initially virialised subcluster of $N \geq 2$ stars must produce at least one bound multiple system. This component contains m_0 stars, where $2 < m_0 \leq N$. Here, we take m_0 to be the largest or equal-largest multiplicity in the end state. In the case where this component is the only multiple, all remaining $N - m_0$ stars are single. The remaining $N - m_0$ stars may also form bound systems. These systems may have any multiplicity m_1, where $2 < m_1 \leq m_0$.

In the first form of this equation, I simultaneously counted all additional component systems of multiplicity m_1 for an existing component of multiplicity m_0, by taking the number of times m_1 divides wholly into the number of remaining stars. So, end states containing a component system of multiplicity m_0 and a component system (or systems) of multiplicity m_1 are counted with the following equation:

$$\mathcal{A}_{N\leq 7} = \sum_{m_0=2}^{N} \left\{ 1 + \sum_{m_1=2}^{m_0} \left\lfloor \frac{N - m_0}{m_1} \right\rfloor \right\}. \tag{5.1}$$

This equation will account for all possible end states for initially virialised subclusters with $2 < N \leq 7$.

For $7 < N \leq 10$, it is possible to achieve end states with component systems of multiplicity m_0, m_1, and m_2, where $m_2 < m_1$, i.e. $N = 8$ may end in two separate triples and a binary, $N = 10$ may result in a quadruple, a triple, and a binary. To count these states, I added an additional level of recursion. For each set of m_0, m_1, there are $N - (m_0 + m_1)$ remaining stars. If $N - (m_0 + m_1) > 2$, the stars may form a multiple of order $2 \leq m_2 < m_1$. We disregard $m_2 = m_1$ systems, as they are counted in the previous sum. The number of components of order m_2 is then given by

$$n_{m_2} = \left\lfloor \frac{N - (m_0 + m_1)}{m_2} \right\rfloor \tag{5.2}$$

where $\lfloor\ \rfloor$ is the floor operator, and the full sum becomes

$$\mathcal{A}_{N\leq 10} = \sum_{m_0=2}^{N} \left\{ 1 + \sum_{m_1=2}^{m_0} \left\{ \left\lfloor \frac{N-m_0}{m_1} \right\rfloor + H(N-(m_0+m_1+2)) \right.\right. \left.\left. \sum_{m_2=2}^{n'-1} \left\lfloor \frac{N-(m_0+m_1)}{m_2} \right\rfloor \right\} \right\}. \tag{5.3}$$

Here $\mathcal{H}$ represents the Heaviside function, i.e.

$$\mathcal{H}(f) \;=\; \begin{cases} 1, & \text{if } f \geq 0\,; \\ 0, & \text{if } f < 0\,. \end{cases} \tag{5.4}$$

Each term of the sum represents one end state of the N-star subcluster. The combination of m_0, m_1, and m_2 which produces each term gives the multiplicities of the systems in that end state, and the value of each sum gives the number of systems with that multiplicity. The equation does not differentiate the type of system (e.g. there is no discrimination between a quadruple which is planetary versus one which is a 2+2) or on which specific stars occupy which remnant system. Further terms may be added to count the end states of $N \leq 10$.

5.3 A universal, recursive sum

Although 5.3 is useful for $N \leq 10$, it becomes unwieldy if more terms are needed. With the goal of finding a more universal expression for A_N, I explored expressing the sum in a more expanded form with simpler terms.

If we keep the outer sum of all terms whose highest multiplicity is m_0:

$$\mathcal{A}_N = \sum_{m_0=2}^{N} 1 + ... \tag{5.5}$$

For each m_0, there will again be $N - m_0$ stars remaining from which to form multiples. Since m_0 is the highest multiplicity possible for the end state, the maximum multiplicity possible in the next term cannot be greater than m_0 or $N - m_0$. Therefore $2 \leq n_1 \leq \mathrm{MIN}(m_0, N - m_1)$ and the sum becomes:

$$\mathcal{A}_N = \sum_{m_0=2}^{N} \left\{ 1 + \left\{ \sum_{m_1=2}^{\mathrm{MIN}(m_0, N-m_1)} 1 + ... \right\} \right\} \tag{5.6}$$

Each new term of the sum depends only upon three values: N, the order of the largest multiple in the previous term, m_{n-1}, and the total order of the multiples which have already been counted up to that n,

$$m_{\mathrm{tot}} = \sum_{i=0}^{n-1} m_i \tag{5.7}$$

Thus, the sum can expand to count to a multiplicity of m_n, where

$$\mathcal{A}_N = \sum_{m_0=2}^{N} \left\{ 1 + \left\{ \sum_{m_1=2}^{\mathrm{MIN}(m_0, N-m_1)} 1 + \left\{ ... \sum_{m_n=2}^{\mathrm{MIN}(m_{n-1}, N-m_{\mathrm{tot}})} 1 \right\} \right\} \right\} \tag{5.8}$$

and can be expressed as a sum of the recursive terms:

$$\mathcal{A}_N = \sum_{m_0=2}^{N} a(m_0, m_{\mathrm{tot}}); \tag{5.9}$$

where

$$a(m_{n-1}, m_{\rm tot}) = 1 + \sum_{m_n=2}^{{\rm MIN}(m_{n-1}, N-m_{\rm tot})} a(m_n, m_{\rm tot}+m_n) \qquad (5.10)$$

This fully recursive form of $\mathcal{A}_N$ gives the total number of end states for any value of N, where each m is the multiplicity of an individual system in the end state. As in 5.3, each term represents one end state of the N-star subcluster, and does not differentiate the type of system or the specific stars in a remnant system. For values $2 \leq N \leq 15$, $\mathcal{A}_N$ is listed in Table 5.2.

Table 5.2. The total number of possible end states of an initially virialized subcluster of stars with $2 \leq N \leq 15$.

N	2	3	4	5	6	7	8	9	10	11	12	13	14	15
$\mathcal{A}_N$	1	2	4	6	10	14	21	29	41	55	76	100	134	175

5.4 Links to Number Theory and the Partition Function

It turns out that the rate of growth of $\mathcal{A}_N$ is identical to an existing function in number theory – the Partition Function. This function, $\rm PAR(N)$, counts the number of ways that an integer N can be expressed as the sum of integers, disregarding order. For example, $\rm PAR(3) = (1+1+1)$, $(2+1)$, (3).

The solution for $\rm PAR(N)$ is calculated using the generating function

$$\sum_{N=0}^{\infty} {\rm PAR}(N) x^N = \prod_{k=1}^{\infty} (\frac{1}{1-x^k}), \qquad (5.11)$$

where $\rm PAR(N)$ is equal to the number of terms whose exponent is N. $\rm PAR(N)$ has no closed-form solution, and can only be calculated exactly as a recurrence relation.

$\mathcal{A}_N$ is not exactly equal to the Partition function, rather it's a restriction of it. The subclusters in this work always have $N \geq 2$. Because the subclusters are initially virialized, solutions where all stars end up single are not possible. There is one such solution for any N in the Partition Function, so $\mathcal{A}_N = \rm PAR(N \geq 2) - 1$. Figure 5.1 shows $\mathcal{A}_N$, $\rm PAR(N)$, and $\rm PAR(N \geq 2) - 1$ for values of N.

5.5 Summary

Here are presented two forms of an equation to enumerate all possible end states for an initially virialised stellar subcluster of N stars. The equations provide the multiplicities of all end components. Equation 5.3 is accurate to $N = 10$. This is sufficient for the types of systems explored in this work, as individual prestellar cores are not expected to produce more than $N = 7$. Equation 5.9, the universal form, is accurate for any value

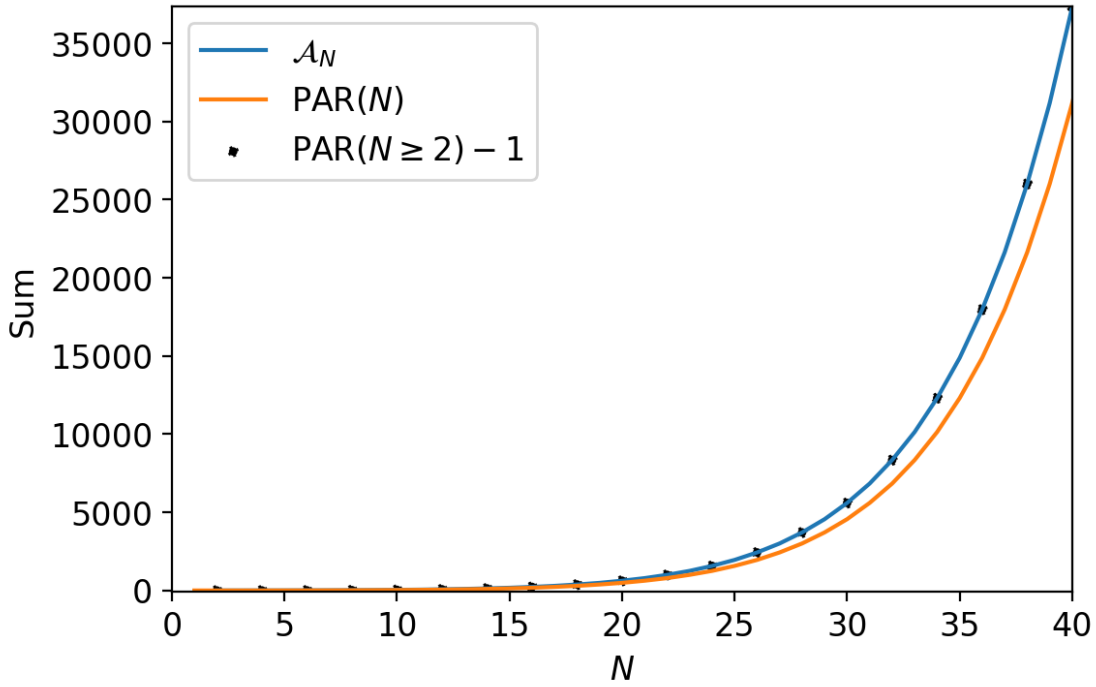

Figure 5.1. Plot of $\mathcal{A}_N$, $\textsc{par}(N)$, and $\textsc{par}(N \geq 2) - 1$ as a function of N for $2 \leq N \leq 40$. $\textsc{par}(N \geq 2) - 1$ fits $\mathcal{A}_N$ exactly.

of N. It is a restricted form of the number theory Partition Function and is simple to implement as a programming loop when exploring higher values of N. Equation 5.9 may be useful in a broader astronomical context, such as in tracking the dissolution of any clustered bodies. Or, in pure mathematics, it may be of interest as an alternate form of the Partition Function.

Chapter 6

Conclusion

"I'm ugly and I'm proud"

Patrick Star — *Spongebob Squarepants*

6.1 Thesis Overview

- **Numerical model:** I have developed and presented a scale-free prescription for initializing and evolving an ensemble of stellar particles ($N \leq 7$) as if they are the fragmentation products of a single, isolated prestellar core (Chapter 2). Initial conditions include the number of stars, mass range, amount and type of ordered rotation, presence of mass segregation, and flattening. To evolve the subclusters, I have written a numerical n-body code with 4th order Runge-Kutte integrator and an adaptive timestep. The particles are treated as point masses and evolved under gravity with no ambient gas (i.e. no stellar accretion or gravitational softening), stellar mass loss, collisions and mergers, or external forces.

- **Multiplicity-tracking algorithm:** I have developed and detailed an algorithm (MMO) which identifies the full orbital hierarchy of all systems that result from an $N \leq 7$ subcluster of objects (Section 2.3). The algorithm calculates the statistics (semi-major axis, period, mutual orbital inclination, eccentricity) of these orbits.

- **Subcluster evolution experiments:** I evolved $3 \leq N \leq 7$-star stellar subclusters with varying initial mass and spatial distributions, types and amounts of ordered rotation, and mass segregation (Section 3.1). I integrated for up to 1000 crossing times (~ 15 Myr for a cluster of M-dwarfs) with regular calls to the MMO (every 33 crossing times).

- **Multiplicity analysis:** I analysed the multiplicity statistics of the stellar systems produced from the evolution of the subclusters (Chapter 3). By mixing the multiplicity statistics from experiments of different N and comparing with the

statistics of solar mass primary systems observed by T21, I determined the mix of N and initial conditions that most closely reproduced the observed stellar multiplicity. I also determined which initial conditions most affect multiplicity outcomes.

- **Orbital parameter analysis:** I analysed the orbital statistics of the stellar systems produced from the evolution of the subclusters (Chapter 4). By comparing the statistics between different parameter sets, I isolated the effects of various initial conditions on orbits, mass ratios, and ejection velocities. Comparing initial conditions with observations, I determined the initial conditions which best reproduced observed distributions.
- **Derivation of end state equation:** I derived two versions of an equation to enumerate all possible end states (with associated multiplicities) for an initially virialised stellar subcluster of N stars (Chapter 5). The equation is a restriction on the number theory partition function and offers an intuitive form of the function for non-mathematical contexts. It is also simple to implement as a programming loop.

6.2 Key Results

This section summarizes the central findings of the thesis, grouped by their relevance to star formation modeling, initial conditions, statistical outcomes, and theoretical derivations.

1. Optimal Number of Stars for Observed Multiplicity

- On average, low-mass prestellar cores must spawn between 4 and 5 stars. This number yields multiplicity statistics that most closely match observations of solar-mass primary systems.
- Of all subcluster initial conditions explored, the initial number of stars has the strongest effect. It shapes multiplicity, orbital periods and separations, dynamical biasing, plurality, mutual orbital inclinations, and ejection timescales.
- A single subcluster of $N > 3$ may spawn more than one long-lived multiple system. For the *Best-Fit Case*, $21(\pm1)\%$ of subclusters produce more than one multiple system, significantly increasing the *Multiplicity Statistics*, especially the fraction of binary systems.

2. Role of initial kinematics and agreement across *Multiplicity* and *Orbital Statistics*

- The best agreement with multiplicity observations occurs when subclusters begin with approximately 50% of their kinetic energy in ordered rotation. Many combinations of initial conditions yield good fits, and all share this characteristic.

- These best-fit initial conditions produce a similarly shaped distribution of mutual orbital inclinations as observations, but with a phase offset.

3. Insensitive parameters

- Subcluster initial conditions such as mass segregation and spatial flattening appear to have little effect on the *Multiplicity* or *Orbital Statistics*.

4. Recursive, universal formula for enumerating end states

- All possible end states for an initially virialized subcluster of N stars are given by Equation 5.3. This is a restriction on the number theory partition function, Equation 5.4, which functions for any value of $N > 1$.

6.3 Future work

6.3.1 Discs and Gas

The experiments make a few simplifying assumptions that likely impact the results. One is that stars form exclusively through Core Fragmentation. Another is that gravity is the only force acting on the particles.

These assumptions contribute to the underproduction of high-multiplicity systems, even in the *Best-Fit case*. Two likely causes are the lack of discs and gas. The protostellar disc can fragment, creating companions with disc-scale separations, while friction with residual gas can bring distant companions into closer orbits. By the time the natal gas surrounding a stellar subcluster disperses, both mechanisms are expected to yield close companions.

Companions formed through these pathways are expected to be robust against dynamical disruption due to their tight orbits. As a result, their inclusion would likely enhance the multiplicity statistics. Future work could therefore benefit from incorporating these close companions.

Interactions between protostellar discs can also tighten orbits at close encounters, removing energy from the orbits.

I could incorporate the effects of Disc Fragmentation and in-spiral without introducing new physics, by modifying the initial conditions to include close pairings consistent with Disc Fragmentation and in-spiral predictions. Additionally, I would replace the global adaptive timestep with a local adaptive timestep scheme to efficiently handle the wide range of distance scales, from tight binaries to wide companions.

Disc interactions require additional physics, but could be added without the need for large hydrodynamical simulations, by assigning a "disc" region around each particle. Each region would have a radius, height, inclination vector, and rotational velocity. As the subcluster evolves and as disc regions intersect, the code would modify the particle velocities and disc parameters according to a prescription. I would write the prescription for interaction effects based upon the findings of Clarke & Pringle (1991).

These modifications are expected to produce more realistic *Multiplicity* and *Orbital Statistics*, bringing the experiments into better agreement with simulations.

6.3.2 Extension of Mass Regime

The analysis conducted in this thesis focuses on solar-mass primary observations. As discussed in subsection 1.2, stellar multiplicity is highly dependent on the mass of the primary, so predictions using solar mass statistics are not applicable to other spectral types. To create a more global understanding of stellar multiplicity, I would extend the analysis in Chapters 3 and 4 to different stellar mass regimes.

I would modify the initial conditions of the experiments to better reflect those predicted by simulations and observations across stellar mass regimes. By comparing the resulting multiplicity statistics with a broad set of observational surveys, it would then be possible to extend the predictions made in Chapters 3 and 4 across all mass ranges. Since multiplicity statistics are published for all spectral types (see Fig. 1.3), these data could be used to constrain the mass dependence of initial conditions such as the number of stars per system, N. Once the numerical experiments are complete for each mass range, this analysis can quickly and easily be repeated as more robust survey statistics become available.

Reproducing the high-mass primary statistics may prove difficult with the model presented here, since their multiplicity is much higher than multiplicity for solar-mass primaries (Figure 1.3). This could be remedied with the incorporation of the disc and gas effects in subsection 6.3.1, which should increase multiplicity. Additionally, the more massive prestellar cores that form massive stars could create a larger number of stars, which would harden the resulting systems through increased ejections of the lowest-mass members.

Finding a mass-dependent prediction of N would help to create a more universal, cohesive understanding of star formation.

6.3.3 Observational Confirmation of Predictions

There are three main results that I present in this thesis which could be confirmed through observations of low-mass protostars:

1. the velocities of very young and forming stars include a significant level of rotation around the center of mass of the group

2. over a short timescale, protostellar groupings undergo many slow ejections (Fig. 4.14b, Fig. 4.13), in agreement with Chen et al. (2013)

3. approximately 20% of protostellar cores produce more than one multiple system, in line with predictions of McDonald & Clarke (1995)

I would explore Prediction 1 by characterizing the rotation of the protostellar systems, and determining the strength of rotation of the protostellar multiple systems around the system center of mass.

I would explore Predictions 2 and 3 in tandem by analyzing surveys such as VANDAM Tobin et al. 2016 and PEACHES Yang et al. 2021, focusing on identifying sources that may have been ejected from their parent groupings. Potential parent systems and their ejected members could be linked through a combination of evidence: similarities in outflow morphology, age, and velocity, as well as spatial proximity and chemical signatures. Parent groupings could also be identified by probing for signs of ejection wakes in their envelopes.

After associating parent groups and ejected systems, I would calculate ejection statistics such as multiplicity, velocity, and age of the ejected protostellar systems and compare with the above predictions.

6.4 Concluding remarks

The experiments and analysis I have presented in this thesis represent a step toward understanding the earliest multiplicity history of the most common stars. They bolster the arguments that most stars must be forming in small groupings from prestellar cores. They inform predictions about the conditions of these groupings as they leave the prestellar phase, such as their bulk rotation and ejection rates. They show us that – even given gravity alone – stars can organize themselves into complex, lasting systems.

The numerical prescriptions that I have developed provide a framework around which to explore the effects of further mechanisms and physics on the creation and stabilization of stellar multiples. The analytical techniques established here create a foundation from which to extend study across stellar mass regimes, in order to understand multiplicity history for all stellar spectral types.

Our model of star formation will never be complete until we understand stellar multiplicity, and our comprehension of multiplicity will not be complete until we understand its beginnings. This thesis brings us closer to that beginning, showing us pathways through which stars come together – and stay together – in the architecture of the universe.

Appendix A

Long-lived septuple systems

Of the many $N = 7$ experimental realisations detailed in Chapter 3, three result in long-lived, 7-star systems. While these systems are too few to extract statistics, they represent interesting outcomes of seven-star dynamics, highlighting the complex and varied architectures that can emerge through gravitation alone.

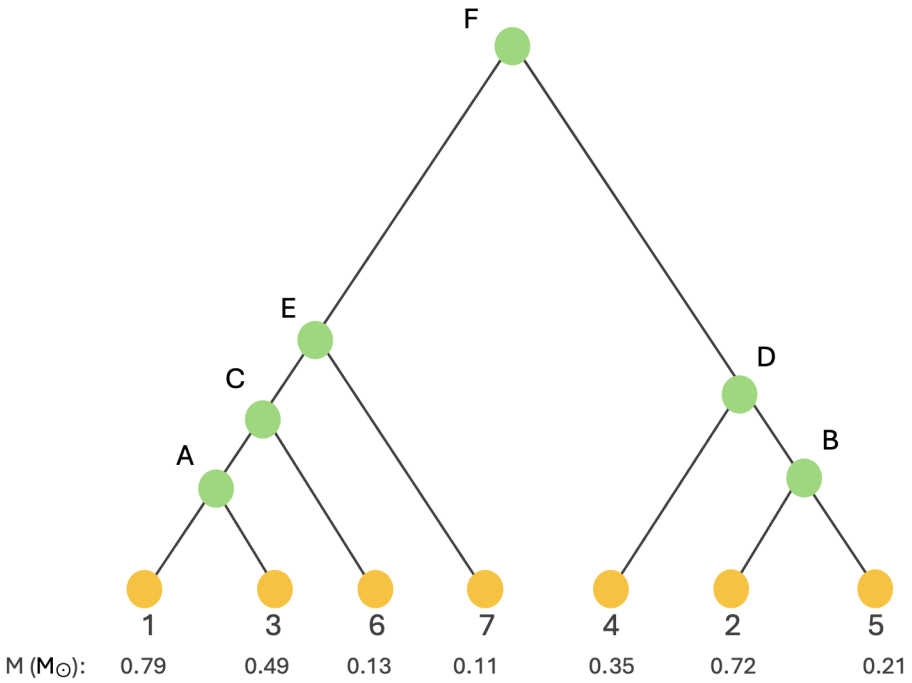

Figure A.1. Diagram of the architecture of System I in the style of Tokovinin (2021). Orange circles represent the stars, which are numbered in order of decreasing mass. The masses are listed below each star and scaled according to the convention in Chapter 3. The green circles represent each orbit, lettered from A to F according to the order which in they are identified by the MMO (see Section 2.3).

A.1 System I: a 4+3 septuple

System I is comprised of a group of 4 stars on planetary orbits, which is itself on a much larger orbit with a group of 3 stars. Figure A.1 is a diagram showing the architecture of System I in the style of Tokovinin (2021). The orbital parameters are listed in Table A.1, with the Chapter 3 scaling applied.

Orbit	θ_o	e	a/AU	P/Myr
A	-	0.42	200	0.0026
B	-	0.87	100	0.0011
C	1.86	0.80	8,600	0.67
D	1.34	0.70	2,500	0.11
E	0.67	0.69	28,000	4.0
F	1.50	0.99	110,000	20

Table A.1. Orbital parameters for System I. Letters A-F denote the orbit. θ_o is mutual orbital inclination between the given orbit and the orbit interior to it, e is eccentricity, a is orbital semimajor axis, and P is orbital period.

The system develops quickly and remains in its final configuration from $t = 66\ t_{\rm cross}$ to the end of the integration at $t = 1000\ t_{\rm cross}$.

A.2 System II: a (2+2)+3 septuple

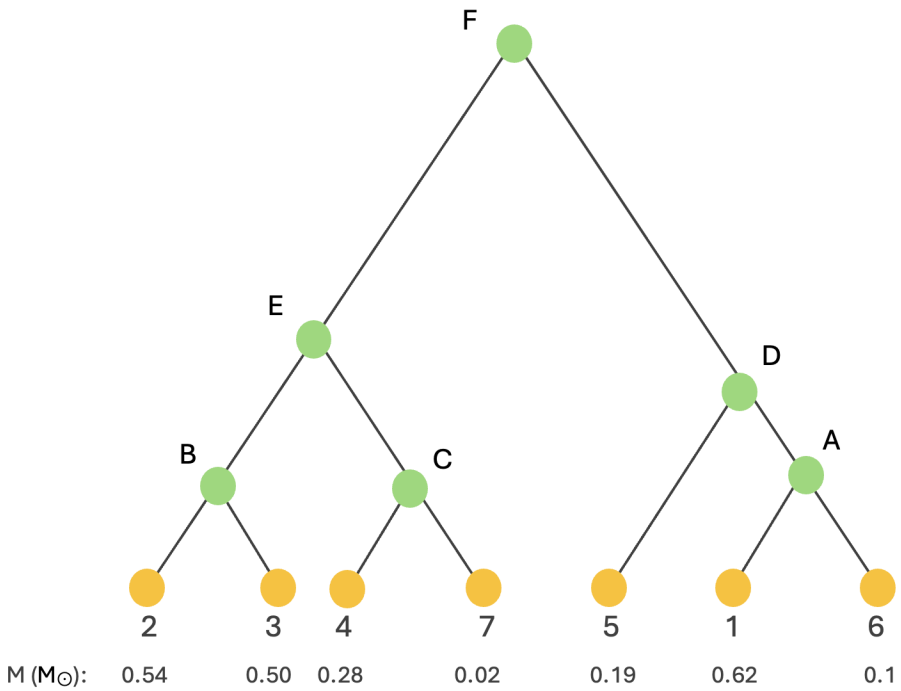

Figure A.2. As Figure A.1, for System II

System II is comprised of a group of 4 stars on 2+2 orbits, which is itself on a much larger orbit with a group of 3 stars. Figure A.2 is a diagram showing the architecture of System II. The orbital parameters are listed in Table A.2, with the same scaling as above.

Orbit	θ_o	e	a/AU	P/Myr
A	-	0.45	120	0.0015
B	-	0.74	900	0.27
C	-	0.54	15,000	3.2
D	0.81	0.37	1,400	0.056
E	2.71	0.98	260,000	110
F	1.98	0.99	1,000,000	700

Table A.2. Orbital parameters for System II. Letters A-F denote the orbit. θ_o is mutual orbital inclination between the given orbit and the orbit interior to it, e is eccentricity, a is orbital semimajor axis, and P is orbital period.

Like System I, this system also develops quickly, in this case by $t \sim 200\ t_{\rm cross}$. It remains in its final configuration until the end of the integration at $t = 1000\ t_{\rm cross}$. Due to its high eccentricity and large orbit, orbit F would likely become unbound over many orbits, or if other bodies were nearby to perturb it (see subsection 4.3.8 for further discussion). Notably, with this scaling, star 7 is in the brown dwarf mass range.

A.3 System III: a (2+3)+1+1 septuple

System III is comprised of a group of 2 stars, which is on a larger orbit with a group of 3 stars. This quintet is in turn orbited by 2 more stars on planetary orbits. Figure A.3 is a diagram showing the architecture of System III. The orbital parameters are listed in Table A.3, with the same scaling as above.

Orbit	θ_o	e	a/AU	P/Myr
A	-	0.39	89	0.00085
B	-	0.95	500	0.015
C	1.56	0.79	13,000	1.7
D	0.77	0.68	16,000	1.5
E	1.55	0.99	160,000	46
F	2.54	0.97	170,000	48

Table A.3. Orbital parameters for System III. Letters A-F denote the orbit. θ_o is mutual orbital inclination between the given orbit and the orbit interior to it, e is eccentricity, a is orbital semimajor axis, and P is orbital period.

Unlike the other two systems, System III develops more slowly, taking until $t \sim 800\ t_{\rm cross}$ to settle into its final configuration. It remains in this form until the end of the integration at $t = 1000\ t_{\rm cross}$.

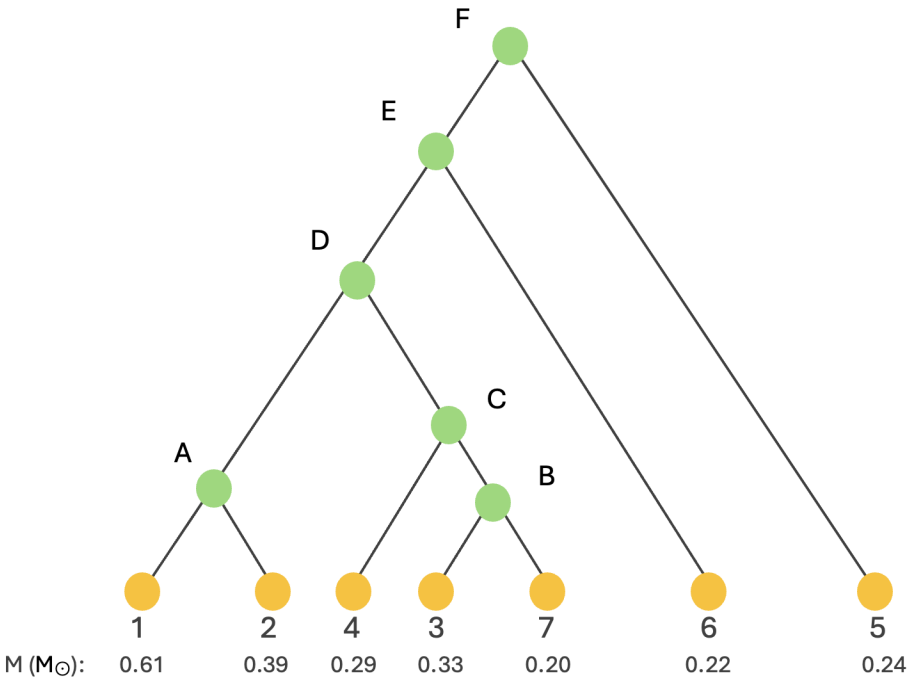

Figure A.3. As Figure A.3, for System III

Bibliography

Aarseth S. J., 1966, *MNRAS*, 132, 35

Aarseth S. J., 2003, Gravitational N-Body Simulations

Aarseth S. J., Zare K., 1974, Celestial Mechanics, 10, 185

Adams W. S., Joy A. H., 1917, *PASP*, 29, 113

Adams F. C., Ruden S. P., Shu F. H., 1989, *ApJ*, 347, 959

Ahmad A., Cohen L., 1973, Journal of Computational Physics, 12, 389

Ahmad A., Cohen L., 1974, in Numerical Solution of Ordinary Differential Equations. pp 313–336

Alves J., Lombardi M., Lada C. J., 2007, Astronomy and Astrophysics, 462, L17

Andersen M., Meyer M. R., Greissl J., Aversa A., 2008, *ApJ*, 683, L183

André P., et al., 2010, *A&A*, 518, L102

Barnes J., Hut P., 1986, *Nature*, 324, 446

Bhattal A. S., Francis N., Watkins S. J., Whitworth A. P., 1998, *MNRAS*, 297, 435

Boffin H. M. J., Watkins S. J., Bhattal A. S., Francis N., Whitworth A. P., 1998, *MNRAS*, 300, 1189

Bonnell I. A., Bate M. R., 1994, *MNRAS*, 271, 999

Boss A. P., 1986, *ApJS*, 62, 519

Broekhoven-Fiene H., et al., 2014, *ApJ*, 786, 37

Cartwright A., Whitworth A. P., 2004, *MNRAS*, 348, 589

Cha S. H., Whitworth A. P., 2003, *MNRAS*, 340, 91

Chabrier G., 2003, Publications of the Astronomical Society of the Pacific, 115, 763

Chabrier G., 2005, in Corbelli E., Palla F., Zinnecker H., eds, Astrophysics and Space Science Library Vol. 327, The Initial Mass Function 50 Years Later. p. 41 (arXiv:astro-ph/0409465), doi:10.1007/978-1-4020-3407-7_5

Chapman S., Pongracic H., Disney M., Nelson A., Turner J., Whitworth A., 1992, *Nature*, 359, 207

Chen X., et al., 2013, *ApJ*, 768, 110

Clarke C. J., Pringle J. E., 1991, *MNRAS*, 249, 588

Connelley M. S., Reipurth B., Tokunaga A. T., 2008a, *AJ*, 135, 2496

Connelley M. S., Reipurth B., Tokunaga A. T., 2008b, *AJ*, 135, 2526

Duquennoy A., Mayor M., 1991, *A&A*, 500, 337

Fernandez M. A., et al., 2017, *PASP*, 129, 084201

Gezari D. Y., Labeyrie A., Stachnik R. V., 1972, *ApJ*, 173, L1

Goodwin S. P., Whitworth A. P., Ward-Thompson D., 2004a, *A&A*, 414, 633

Goodwin S. P., Whitworth A. P., Ward-Thompson D., 2004b, *A&A*, 423, 169

Hamers A. S., 2020, *MNRAS*, 494, 5298

Hayashi T., Trani A. A., Suto Y., 2022, *ApJ*, 939, 81

Hennebelle P., Whitworth A. P., Cha S. H., Goodwin S. P., 2004, *MNRAS*, 348, 687

Herschel W., 1803, Philosophical Transactions of the Royal Society of London Series I, 93, 339

Hirsch L. A., et al., 2021, *AJ*, 161, 134

Hockney R. W., Eastwood J. W., 1988, Computer simulation using particles

Holman K., Walch S. K., Goodwin S. P., Whitworth A. P., 2013, *MNRAS*, 432, 3534

Kounkel M., et al., 2019, *AJ*, 157, 196

Kozai Y., 1962, *AJ*, 67, 591

Kramer C., Stutzki J., Rohrig R., Corneliussen U., 1998, *A&A*, 329, 249

Kratter K. M., Matzner C. D., Krumholz M. R., Klein R. I., 2010, *ApJ*, 708, 1585

Kraus A. L., Hillenbrand L. A., 2012, *ApJ*, 757, 141

Kraus A. L., Ireland M. J., Martinache F., Hillenbrand L. A., 2011, *ApJ*, 731, 8

Kroupa P., 2001, *MNRAS*, 322, 231

Kuffmeier M., Calcutt H., Kristensen L. E., 2019, *A&A*, 628, A112

Kuruwita R. L., Haugbølle T., 2023, *A&A*, 674, A196

Kutta W., 1901, Zeitschrift für Mathematik und Physik, 46, 435

Labeyrie A., 1970, *A&A*, 6, 85

Larson R. B., 1978, *MNRAS*, 184, 69

Lee A. T., Offner S. S. R., Kratter K. M., Smullen R. A., Li P. S., 2019, *ApJ*, 887, 232

Lidov M. L., 1962, *P&SS*, 9, 719

Lomax O., Whitworth A. P., Hubber D. A., Stamatellos D., Walch S., 2014, *MNRAS*, 439, 3039

Lomax O., Whitworth A. P., Hubber D. A., Stamatellos D., Walch S., 2015a, *MNRAS*, 447, 1550

Lomax O., Whitworth A. P., Hubber D. A., 2015b, *MNRAS*, 449, 662

Lomax O., Whitworth A. P., Hubber D. A., 2016, *PASA*, 33, e004

Makino J., 1991, *ApJ*, 369, 200

Mamajek E. E., Kenworthy M. A., Hinz P. M., Meyer M. R., 2010, *AJ*, 139, 919

Mardling R. A., Aarseth S. J., 2001, *MNRAS*, 321, 398

Massey 1951, Journal of the American Statistical Association, 46, 68

McDonald J. M., Clarke C. J., 1993, *MNRAS*, 262, 800

McDonald J. M., Clarke C. J., 1995, *MNRAS*, 275, 671

McMillan S. L. W., Aarseth S. J., 1993, *ApJ*, 414, 200

Miller R. H., 1964, *ApJ*, 140, 250

Moeckel N., Bally J., 2007, *ApJ*, 661, L183

Motte F., André P., Neri R., 1998, Astronomy and Astrophysics, 336, 150

Muñoz D. J., Kratter K., Vogelsberger M., Hernquist L., Springel V., 2015, *MNRAS*, 446, 2010

Mugrauer M., Rück J., Michel K.-U., 2023, Astronomische Nachrichten, 344, e20230055

Naoz S., 2016, *ARAA*, 54, 441

Newton I., 1687, Philosophiae Naturalis Principia Mathematica., doi:10.3931/e-rara-440.

Offner S. S. R., Kratter K. M., Matzner C. D., Krumholz M. R., Klein R. I., 2010, *ApJ*, 725, 1485

Offner S. S. R., Moe M., Kratter K. M., Sadavoy S. I., Jensen E. L. N., Tobin J. J., 2023, in Inutsuka S., Aikawa Y., Muto T., Tomida K., Tamura M., eds, Astronomical Society of the Pacific Conference Series Vol. 534, Protostars and Planets VII. p. 275 (arXiv:2203.10066), doi:10.48550/arXiv.2203.10066

Ostriker E. C., 1994, *ApJ*, 424, 292

Pickering E. C., Bailey S. I., 1896, *ApJ*, 4, 235

Portegies Zwart S., 2011, AMUSE: Astrophysical Multipurpose Software Environment, Astrophysics Source Code Library, record ascl:1107.007 (ascl:1107.007)

Pringle J. E., 1989, *MNRAS*, 239, 361

Raghavan D., et al., 2010, *ApJS*, 190, 1

Reipurth B., Mikkola S., 2015, *AJ*, 149, 145

Reipurth B., Zinnecker H., 1993, *A&A*, 278, 81

Rohde P. F., Walch S., Clarke S. D., Seifried D., Whitworth A. P., Klepitko A., 2021, *MNRAS*, 500, 3594

Runge C., 1895, Mathematische Annalen, 46, 167

Salpeter E. E., 1955, The Astrophysical Journal, 121, 161

Schmeja S., Kumar M. S. N., Ferreira B., 2008, *MNRAS*, 389, 1209

Shariat C., El-Badry K., Naoz S., 2025, *PASP*, 137, 094201

Sigalotti L., Cruz F., Hareter M., Gabbasov R., Klapp J., Fierro-Santillán C. R., Ramírez-Velásquez J. M., Zsargó J., 2023, *MNRAS*, 519, 2578

Stamatellos D., Whitworth A. P., 2008, *A&A*, 480, 879

Stamatellos D., Whitworth A. P., 2009, *MNRAS*, 400, 1563

Stamatellos D., Hubber D. A., Whitworth A. P., 2007, *MNRAS*, 382, L30

Stamatellos D., Whitworth A. P., Hubber D. A., 2011, *ApJ*, 730, 32

Stamatellos D., Whitworth A. P., Hubber D. A., 2012, *MNRAS*, 427, 1182

Stebbins J., 1910, *ApJ*, 32, 185

Sterzik M. F., Durisen R. H., 1998, *A&A*, 339, 95

Stromgren E., 1900, Meddelanden fran Lunds Astronomiska Observatorium Serie I, 13, 3

Strömgren E., 1909, Astronomische Nachrichten, 182, 181

Thies I., Kroupa P., Goodwin S. P., Stamatellos D., Whitworth A. P., 2010, *ApJ*, 717, 577

Thomas S. J., Rodgers B., van der Bliek N. S., Doppmann G., Bouvier J., Salvo C. A., Beuzit J.-L., Rigaut F., 2023, *AJ*, 165, 135

Tobin J. J., et al., 2016, *ApJ*, 818, 73

Tobin J. J., et al., 2022, *ApJ*, 925, 39

Tokovinin A., 2014, *AJ*, 147, 87

Tokovinin A., 2021, Universe, 7, 352

Tokovinin 2023, Updated Multiple Star Catalog (MSC): Dec 2023, doi:https://doi.org/10.26093/cds/vizier.22350006

Turner J. A., Chapman S. J., Bhattal A. S., Disney M. J., Pongracic H., Whitworth A. P., 1995, *MNRAS*, 277, 705

Vogel H. C., 1890, Astronomische Nachrichten, 123, 289

Walch S., Burkert A., Whitworth A., Naab T., Gritschneder M., 2009, *MNRAS*, 400, 13

Walch S., Whitworth A. P., Girichidis P., 2012, *MNRAS*, 419, 760

Watkins S. J., Bhattal A. S., Boffin H. M. J., Francis N., Whitworth A. P., 1998a, *MNRAS*, 300, 1205

Watkins S. J., Bhattal A. S., Boffin H. M. J., Francis N., Whitworth A. P., 1998b, *MNRAS*, 300, 1214

Whitworth A. P., Stamatellos D., 2006, *A&A*, 458, 817

Whitworth A. P., Chapman S. J., Bhattal A. S., Disney M. J., Pongracic H., Turner J. A., 1995, *MNRAS*, 277, 727

Wielen R., 1967, Veroeffentlichungen des Astronomischen Rechen-Instituts Heidelberg, 19, 1

Wielen R., 1974, in Mavridis L. N., ed., Stars and the Milky Way System. p. 169

Yang Y.-L., et al., 2021, *ApJ*, 910, 20

Zimmerman N., et al., 2010, The Astrophysical Journal, 709, 733–740

van Biesbroeck G., 1944, *AJ*, 51, 61

von Hoerner S., 1960, Zeitschrift für Astrophysik, 50, 184

von Zeipel H., 1910, Astronomische Nachrichten, 183, 345